

Chapter 5

Fe K-Edge X-ray Absorption Edge Spectra of Iron Models Relevant to Dinuclear Non-Heme Iron Enzyme Systems

5.1. Introduction

The appearance of transition metal edge spectra are characteristic of the coordination environment and oxidation state of the metal ion and have been both explained by, and used to demonstrate the utility of, crystal field¹ and molecular orbital theory.² Transition metal edges have been the subject of investigation for a number of years, however few definitive assignments of the observed transitions have been made.³ Systematic investigations of structurally characterized inorganic models by X-ray absorption near edge spectroscopy (XANES) have resulted in correlations of the appearance of the edge spectra with symmetry, oxidation state and ligand environment. These studies have been used to provide insight into the structural environment of the active sites of metalloprotein systems, including the multi-copper oxidase laccase⁴, the manganese-containing oxygen evolving complex from photosystem II,⁵ and the nickel enzymes carbon monoxide dehydrogenase⁶ and hydrogenase.⁷ We propose to utilize X-ray absorption spectroscopy to similarly characterize Fe XANES spectra of dinuclear non-heme iron model compounds of relevance to hemerythrin, ribonucleotide reductase, purple acid phosphatase and methane monooxygenase.⁸

Fe K-edge X-ray absorption spectra have been collected on a number of dinuclear non-heme iron models. All of the compounds studied have high-spin octahedrally coordinated iron atoms with N and/or O ligation. The model compounds investigated contained tri-, di-, and mono-bridged iron centers with various combinations of oxo, hydroxo, alkoxo and carboxylato bridging groups. Correlations of the appearance of the edge spectra with the numbers and types of bridges, changes in the ligation sphere, and changes in the oxidation state of the diiron center will be discussed. Comparisons will be made with the edge spectra of the hydroxylase component of soluble methane monooxygenase from *Methylococcus capsulatus* (Bath).⁹

5.1.1. Interpretation of Transition Metal XANES Spectra

The dipole-allowed transition for an X-ray absorption K-edge is from an initial $1s$ state to a final np state ($\Delta l = 1$) and will correspond to the most intense region in the edge spectrum. Transitions are commonly seen below the $4p$ threshold for transition metal spectra. The weak pre-edge feature has been attributed to a formally dipole-forbidden $1s \rightarrow 3d$ transition made allowed by $4p$ mixing into the $3d$ states as a result of non-centrosymmetric symmetry of the metal site and vibronic coupling.^{10,11} This assignment has been confirmed by the absence of this feature in K-edge spectra of d^{10} transition

metals,¹² and by single-crystal polarized studies for other metals.¹³ The intensity of this feature increases as the metal site is distorted from octahedral to tetrahedral symmetry (greater 4p mixing due to symmetry reduction), and can therefore be used as a probe of the coordination number and/or the site symmetry of the absorbing atom.¹⁴

Shoulders have been observed on the rising edge of some transition metal spectra which have been explained as the forbidden $1s \rightarrow 4s$ transition or as the allowed $1s \rightarrow 4p$ transition. Single-crystal oriented edge studies have been instrumental in determining the assignment of this feature. Transitions to the spherically symmetric 4s orbital would not exhibit any polarization dependence unlike transitions to the directional 4p orbitals. A single-crystal polarized study of a Cu(I) compound whose edge spectrum exhibited a shoulder on the rising edge showed the feature to exhibit polarization-dependent intensity,¹⁵ and permitted assignment of the transition as occurring to a $4p_z$ final state orbital. The same conclusion was reached for a similar feature in the edge spectrum of a distorted O_h Fe(III) compound using oriented single-crystal measurements.¹⁶ The sharpness and intensity of this feature has been noted to be quite strong and well-resolved in square planar complexes of Fe,¹⁴ Cu¹⁵ and Ni,^{6,7} which reflects the splitting of the 4p levels as expected for D_{4h} symmetry metal sites.¹

The generally accepted explanation of the shoulder is that it is a shake-down feature associated with the $1s \rightarrow 4p$ transition resulting from the transfer of an electron from a ligand valence orbital into the metal 3d manifold made allowed by final state relaxation.^{17,18} This ligand-to-metal-charge transfer (LMCT) shakedown feature would occur to lower energy than the metal $1s \rightarrow 4p$ transition by an amount equal to the difference in energy between the ligand 2p and metal 3d levels. The energy of the valence level of a more covalent ligand is higher than that of a less covalent ligand, resulting in a greater energy difference between the ligand orbital and the relaxed metal 3d state. The position of the LMCT shake-down feature would therefore be expected to move to lower energy as the covalency of the ligands increased.

5.2. Experimental

The model compounds investigated for this study are summarized in Table 5.1.¹⁹ The compounds were synthesized according to the references listed in the table with the following exceptions. All of the tribridged samples were provided by Prof. Stephen Lippard of the Massachusetts Institute of Technology. The SALMP dibridged compounds in all three oxidation states were provided by Prof. Richard Holm of Harvard University.

Table 5.1. Summary of Samples.

Sample Name	Sample	Ref. 19	Description	Experiment Beamline
FE2CO2	$[\text{Fe}_2\text{O}(\text{OAc})_2\{[\text{OP}(\text{OEt})_2]_3\text{Co}(\text{C}_5\text{H}_5)\}_2]$	a	tribridge, diferric	NSLS X
FE3BIPHME	$[\text{Fe}_2\text{O}(\text{O}_2\text{CH})_4(\text{BIPhMe})(\text{CH}_3\text{OH})]$	b	tribridge, diferric	SSRL 4-
FEHBPZO	$[\text{Fe}_2\text{O}(\text{OAc})_2(\text{HB}(\text{pz})_3)_2]$	c	tribridge, diferric	SSRL 7-
FEHBPZOH	$[\text{Fe}_2\text{O}(\text{OAc})_2(\text{HB}(\text{pz})_3)_2](\text{ClO}_4)$	d	tribridge, diferric	SSRL 7-
FE2BIPHME	$[\text{Fe}_2(\text{O}_2\text{CH})_4(\text{BIPhMe})]$	b	tribridge, diferrous	SSRL 7-
FECHL	$[\text{FeOH}(\text{H}_2\text{O})\text{Chel}]_2(\text{H}_2\text{O})_4$	e	dibridge, diferric	SSRL 7-
FEDIPIC	$[\text{FeOH}(\text{H}_2\text{O})\text{Dipic}]_2$	e	dibridge, diferric	SSRL 4-
FESALMP0	$[\text{Fe}_2(\text{salmp})_2] \cdot 2\text{DMF}$	f	dibridge, diferric	SSRL 7-
FESALMP1	$(\text{Et}_4\text{N})[\text{Fe}_2(\text{salmp})_2] \cdot 2\text{DMF}$	f	dibridge, semimet	SSRL 7-
FESALMP2	$(\text{Et}_4\text{N})_2[\text{Fe}_2(\text{salmp})_2] \cdot 4\text{MeCN}$	f	dibridge, diferrous	SSRL 7-
FETPAOAC	$[\text{Fe}_2(\text{TPA})_2\text{O}(\text{OAc})](\text{ClO}_4)_2$	g	dibridge, diferric	SSRL 7-
FETPAO3	$[\text{Fe}_2(\text{TPA})_2\text{O}(\text{CO}_3)](\text{ClO}_4)_2$	h	dibridge, diferric	SSRL 7-
FETPAPHT	$[\text{Fe}_2(\text{TPA})_2\text{O}(\text{phthalate})](\text{ClO}_4)_2$	h	dibridge, diferric	SSRL 7-
FE2OPHEN	$[\text{Fe}_2\text{O}(\text{Phen})_4(\text{H}_2\text{O})_2](\text{ClO}_4)_4$	i	monobridge, diferric	SSRL 4-
FE2OHBPZ	$[\text{Fe}_2\text{O}(\text{HB}(\text{pz})_3)_4]$	j	monobridge, diferric	NSLS X

Details of the preparation and data collection for the hydroxylase samples (EXAFS5, EXAFS7, and EXAFS6) have been presented in reference 9 and in Chapters 2 and 3.

Samples for XAS experiments were diluted with BN powder, finely ground with a mortar and pestle, and pressed into a 1mm thick Al sample spacer windowed with Mylar tape (total sample weight, ~ 55 mg). The samples were run in transmission mode at the Stanford Synchrotron Radiation Laboratory (SSRL) on unfocused 8-pole wiggler beamlines 4-3 or 7-3 (18 kG), or on unfocused bending magnet beamline X19A at the National Synchrotron Light Source (NSLS) at Brookhaven National Laboratory (see Table 5.1). Ring operating conditions were 3.0 GeV and 40-90 mA at SSRL, and 2.5 GeV and 90-200 mA at NSLS. The height of the beam was defined to be 1 mm using slits in front of the monochromator, and a Si(220) monochromator was used to maximize energy resolution for the edge spectra (~2 eV under these conditions for Fe). The edge spectra of the samples run at NSLS have worse resolution due to software limitations on the step size in the edge region. The monochromator was detuned 50% at 7475 eV (the end of the Fe edge scan) to reject higher harmonics in the incident beam. The incident and transmitted beam intensity was monitored by using N₂-filled ionization chambers of the standard design. The diferrous and semimet model compounds were run at 10 K by using a continuous flow LHe cryostat (Oxford Instruments model CF1208). The diferric models were either run at ambient temperature, or at 10 K if the cryostat was already in use.

Energy calibration for each scan was performed by using an internal foil calibration method²⁰, setting the energy of the first inflection point of the iron foil as 7111.2 eV. Although the signal-to-noise ratio for the model compounds is high enough to obtain satisfactory data with one scan, more than one scan was measured to insure reproducibility of the data. In general, 2 or 3 scans were averaged together for each sample. The data were background-subtracted by fitting a polynomial to the pre-edge region which was extracted through the post-edge region and subtracted. The edge jump was normalized to unity using a polynomial through the post-edge region. Care was taken to insure that the data for each sample were normalized to each other for direct comparison. This process involved adjusting the background subtraction to insure that the slope of the data from sample to sample was the same, and adjusting the normalization to insure that the edge jump from sample to sample was the same.

5.3. Results and Discussion

Positions of the features in the edge spectra were determined by measuring the position of the half-width at half-height of the second derivative of the spectra, and are

presented in Table 5.2. In many cases, features were suggested by the second derivative that were not clearly resolved in the edge spectrum themselves. The positions of these features are enclosed in parentheses.

5.3.1. Description of the Edge Spectra

5.3.1.1. Models Containing a μ -oxo Bridge. In Figure 5.1 are the edge spectra of representative tri-, di-, and mono-bridged models which incorporate a μ -oxo bridge. The spectra represent different ligation of the iron site, from 6 O (**FE2CO2**) to 5 N and 1 O (**FE2OHBPZ**). The most intense pre-edge transition (region A in the spectra), occurs between 7114.1 - 7114.8 eV (Figure 5.2, top curve). A lower energy transition can be seen in the spectra of the di- and mono-bridged compounds (see **FE2OPHEN**) and occurs between 7112.2 - 7112.6 eV. The energy splitting between the two features is on the order of 2 eV. The resolution of the low-energy shoulder correlates with the increase in the number of N atoms in the first coordination sphere. It is best resolved in the complexes which have 2 O and 4 N (**FETPAOAC** and **FE2OPHEN**, Figure 5.2; **FETPAO3** and **FETPAPHT**, data not shown). In **FEHBPZO** (3 O/3 N, Figure 5.2), **FE3BIPHME** (4 O/2 N, see Figure 5.5) or **FE2CO2** (6 O, Figure 5.2), the lower energy transition is not as clearly resolved and leads to the asymmetric appearance of the pre-edge feature. This trend also coincidentally correlates with the decrease in the number of bridges from three to two. It cannot be determined if the ligation or the number of bridges is a more important factor in determining the appearance of the pre-edge feature based on the data available.

A shoulder on the rising edge of the spectra (Feature B) is clearly resolved in the models containing more than 3 N atoms in the first coordination sphere (Figure 5.1, bottom curve), however the second derivatives suggest the presence of this feature in the other models as well. In the tribridged models, the shoulder occurs between 7125.3 and 7125.9 eV and in the di- and mono-bridged models, the feature appears between 7123.5 and 7125.6 eV. The intensity of this feature is lowest in the 5 N/1 O model **FE2OHBPZ** and highest in the 4 N/2 O model **FE2OPHEN**. As seen with the resolution of the shoulder in the pre-edge feature, the appearance of the shoulder correlates both with increasing N ligation and decreasing number of bridges.

The most intense transition in the edge spectra occurs between 7128.1 and 7130.0 eV (Feature C). This feature is more narrow in the di- and mono-bridged compounds than in the tri-bridged compounds. The position of the feature does not seem to correlate with either the number of bridges or the first shell ligation. The energy difference between the position of the rising edge shoulder and the primary transition ranges from 3.7 eV for

Table 5.2. Energies of Features^a in the Edge Spectra of Diiron Models.

Sample	Coordination Environment	Bridge System	Feature A1 eV	Feature A2 eV	Feature B eV	Feature C eV
OXO-BRIDGED MODELS						
diferric						
FE2CO2	6 O	O, (OAc) ₂ ^b		7114.1	(7125.3)	712
FE3BIPHME	4 O, 2 N	O, (O ₂ CH) ₂ ^b		7114.8	(7125.9)	see
FEHBPZO	3 O, 3 N	O, (OAc) ₂ ^b		7114.3	(7125.6)	712
FETPAOAC	4 N, 2 O	O, OAc ^b	(7112.2)	7114.3	7124.6	712
FETPACO3	4 N, 2 O	O, CO ₃ ^b	(7112.6)	7114.2	7124.3	712
FETPAPHT	4 N, 2 O	O, (OPht) ^{b,c}	(7112.4)	7114.3	7124.5	713
FE2OPHEN	4 N, 2 O	O	7112.4	7114.6	7125.6	712
FE2OHBPZ	5 N, 1 O	O		7114.3	7123.5	712
NON-OXO-BRIDGED MODELS						
diferric						
FEHEL	5 O, 1 N	(OH) ₂	7112.9	7114.5	(7127.9)	713
FEDIPIC	5 O, 1 N	(OH) ₂	7112.7	7114.3	(7125.9)	713

Table 5.2. continued

Sample	Coordination Environment	Bridge System	Feature A1 eV	Feature A2 eV	Feature B eV	Feature C eV
FESALMP0	4 O, 2 N	(OPh) ₂ ^c	7112.4	7114.3		(7128.0)
FEHBPZOH	3 O, 3 N	OH, (OAc) ₂ ^b	7112.7	7114.4	(7127.1)	7130.0
semimet						
FESALMP1	4 O, 2 N	(OPh) ₂ ^c	7112.4	7114.1	(7124.9)	7126.3
diferrous						
FESALMP2	4 O, 2 N	(OPh) ₂ ^c	7111.6	7113.8	(7123.3)	7125.7
FE2BIPHME	4 O, 2 N	(O ₂ CH) ₃ ^d	7111.6	7113.7		7125.4

^aThe energies were determined by measuring the position of the half-maximum at half-height of features in the second derivative of the edge spectra. Energies in parenthesis represent features seen in the second derivative that are not clearly resolved in the edge spectra, and included for comparison. ^bThe carboxylate bridge coordinates to the iron center in a bidentate mode. ^cThe phenol bridge derives from the ligand coordinating the iron atoms. Two additional extended bridges involving the N atoms are present. ^dOne formate group bridges the iron center in a monodentate mode via one oxygen atom, and two formates bridge in a bidentate mode through each oxygen atom.

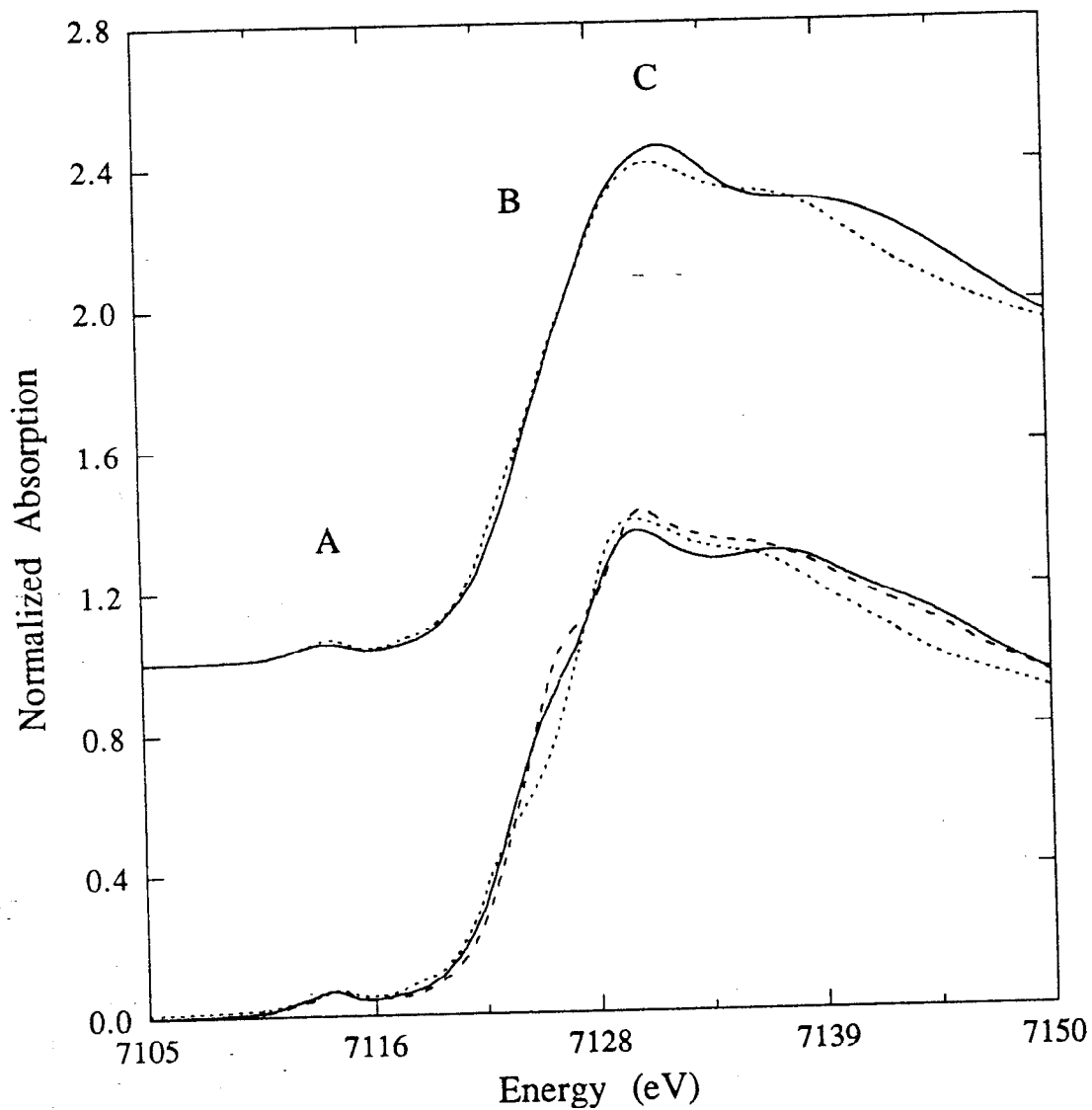


Figure 5.1. The Fe K-edge XANES spectra of oxo-bridged model compounds. Tribridged models **FE₂CO₂** (solid) and **FEHBPZO** (dot) are presented in the top curve. Dibridged models **FETPAOAC** (solid), **FE₂OPHEN** (dash) and **FE₂OHBPZ** (dot) are presented in the bottom curve.

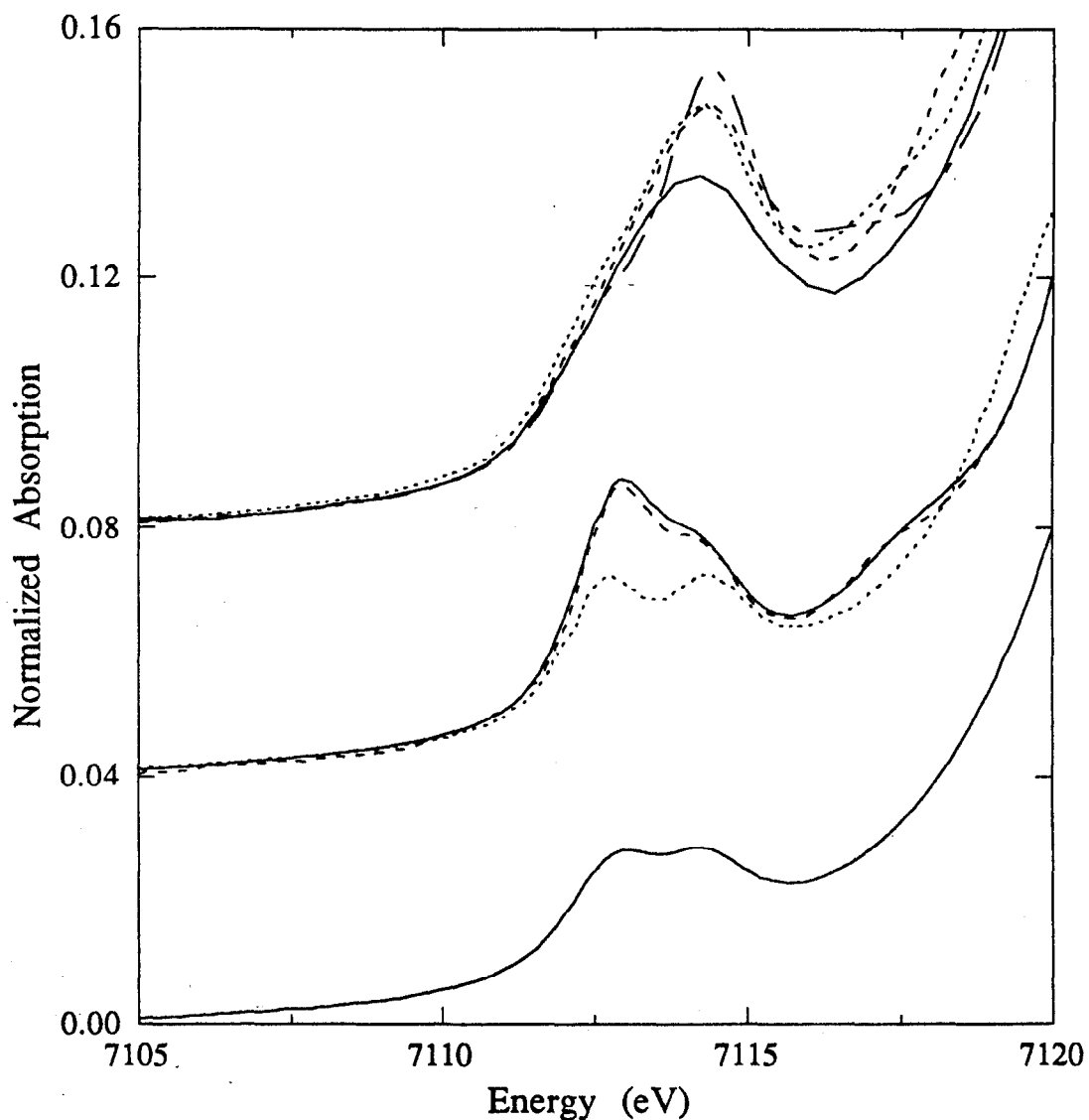


Figure 5.2. The pre-edge features of iron model compounds. The top curve shows the pre-edge transitions of oxo-bridged models **FE₂CO₂** (solid), **FEHBPZO** (dash), **FETPAOAC** (dot) and **FE₂OPHEN** (dash-dot). The middle curve shows the pre-edge transitions of non-oxo-bridged models **FECH₂EL** (solid), **FEDIPIC** (dash) and **FEHBPZOH** (dot). The bottom curve shows the pre-edge feature from monomeric **Fe(acac)₃** (solid). Note the difference in the appearance of the pre-edge feature of the oxo-bridged models compared to the non-oxo-bridged models.

FETPACO3 to 5.5 eV for **FETPAPHT** with the splittings for all of the rest of the compounds falling within this range (Table 5.2). There is also a broad feature above 7135 eV in all of the compounds whose appearance and position also varies in a non-systematic way from compound to compound.

5.3.1.2. Non-oxo Bridged Models. The edge spectra for representative di- and tribridged models which do not contain an oxo bridge are presented in Figure 5.3. These models represent ligation of 5 O and 1 N (**FECHL** and **FEDIPIIC**) and 3 O and 3 N (**FEHBPZOH**). The edge spectrum of **FESALMP0** (4 O/2 N) is presented in Figure 5.4. The shape of the pre-edge feature (region A) in these models is also independent of the number of bridges in the diiron center (Figure 5.2, middle curve) and quite different from the pre-edge feature of the oxo-bridged models. In all of the non-oxo-bridged models, the pre-edge feature is clearly a doublet, with the more intense transition occurring between 7112.4 and 7112.9 eV and the weaker transition occurring between 7114.3 and 7114.6. The difference in relative intensities of these transitions is greater for the 5 O/1 N compounds than for the 4 O/2 N (see Figure 5.5) or 3 O/3 N compound and the energy splitting between the transitions is in the range of 1.6 to 1.9 eV. In addition, a shoulder is seen between the pre-edge transition and the rising edge in the spectra of **FECHL** and **FEDIPIIC** at ~ 7118 eV (Figure 5.2). A feature is seen in this region of the second derivatives of the edge spectra for all of the models, however it is not clearly seen in the edge spectra themselves. This feature may be the forbidden $1s \rightarrow 4s$ transition, which would also be made allowed by vibronic coupling.

There is a suggestion of a shoulder on the rising edge of **FECHL** (5 O/1N), which occurs at 7127.9 eV according to the second derivative of the edge spectrum. Unlike the oxo-bridged models, however, the appearance of a rising edge shoulder does not occur with increasing numbers of N atoms in the first coordination sphere as a shoulder is not seen in **FEHBPZOH** which has 3 N and 3 O atoms. In the non-oxo-bridged models, then, the appearance of the shoulder may be due to the reduction in the number of bridges in the diiron center. This is also consistent with the appearance of the rising edge shoulder in the oxo-bridged models, however in the case of the non-oxo-bridged models, the effect is not as dramatic.²¹

The main transition in the non-oxo-bridged models (Feature C) occurs at 7130 eV in the spectrum of **FEHBPZOH** and **FEDIPIIC**, and at 7131.6 in the spectrum of **FECHL**. The edge spectrum of **FESALMP0** is not very well defined (Figure 5.4). The position of Feature C in the non-oxo-bridged models occurs at slightly higher energies than the position of the corresponding feature in the oxo-bridged models (7128.1 - 7130

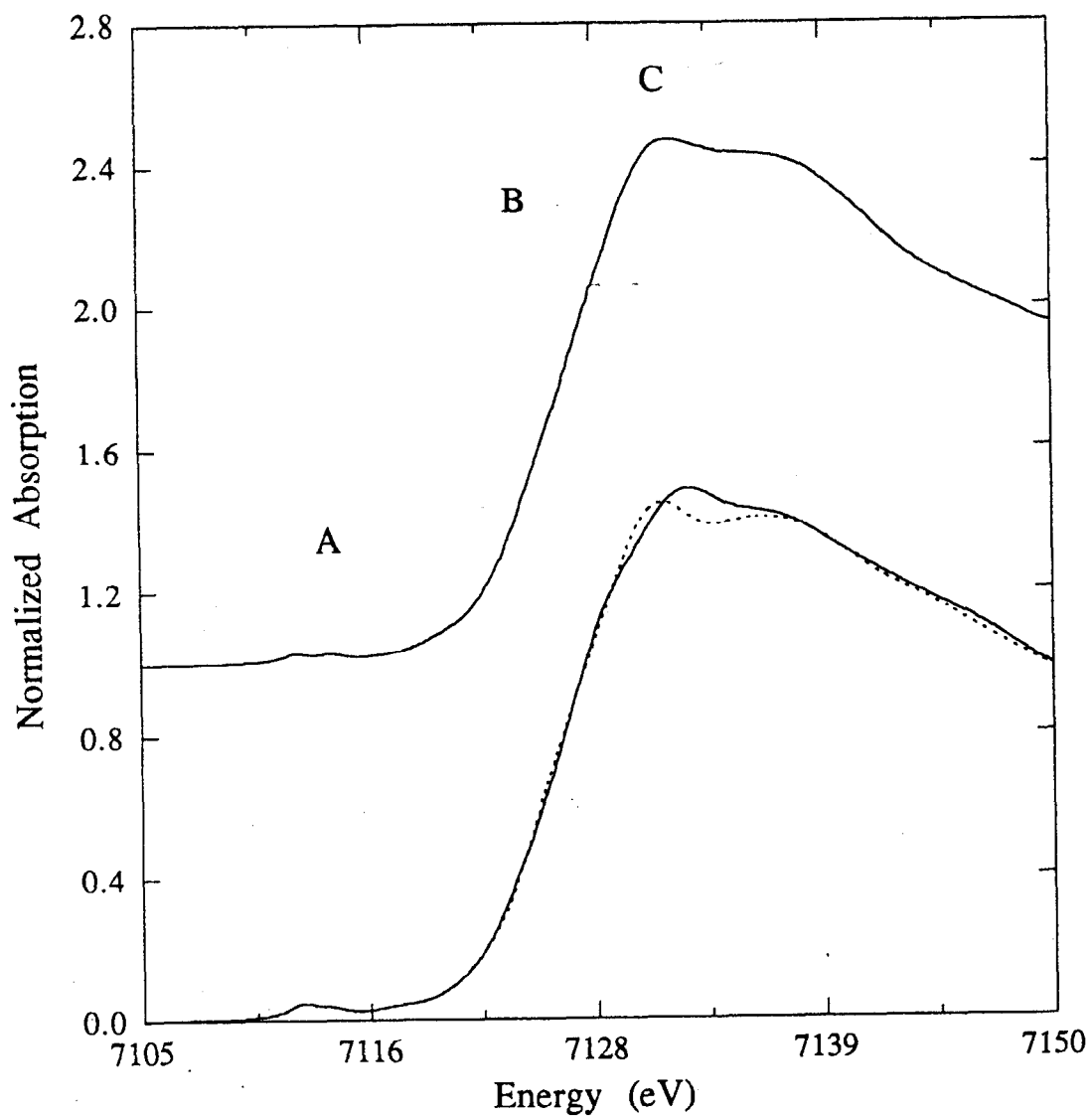


Figure 5.3. The Fe K-edge XANES spectra of non-oxo-bridged model compounds. Tribridged model **FEHBPZOH** (solid) is presented in the top curve. Dibridged models **FECHL** (solid), and **FEDIPIC** (dot) are presented in the bottom curve.

eV). As in the edge spectra of the oxo-bridged models, there is a broad feature which occurs above 7135 eV in the spectra of **FECHL**, **FEDIPIC**, and **FEHBPZOH**.

5.3.1.3. Changes in Spectra with Oxidation State. The spectra of the **FESALMP** dimer series in all three oxidation states are presented in Figure 5.4 (top curve). Upon reduction from the diferric Fe(III)Fe(III) state to the semimet Fe(III)Fe(II) state, the position of the edge (measured at an absorption value of 1) moves to lower energy by 2.3 eV, the edge broadens, and the intensity of the main transition region (Feature C) decreases somewhat. In the diferrous Fe(II)Fe(II) state, the position of the edge moves 4.3 eV to lower energy relative to the diferric edge and the shape of the edge changes, increasing in intensity and becoming more narrow. For the **BIPHME** models (Figure 5.4, bottom curve), the edge moves 3.3 eV to lower energy from the diferric (**FE3BIPHME**) to the diferrous (**FE2BIPHME**) state, and the intensity and appearance of the main transitions change in a manner similar to that described for the **FESALMP** series.

The pre-edge feature in the reduced forms of these models is also a doublet (Figure 5.5, top curve), and like the non-oxo-bridged diferric models, the first transition is more intense than the second transition. The first transition occurs at 7111.6 eV in the diferrous models and the second transition occurs at 7113.7 eV for **FE2BIPHME** and at 7118.3 eV for **FESALMP2**, corresponding to a splitting of 2.1 and 2.2 eV, respectively. The pre-edge of the semimet model **FESALMP1** is broader and less well-resolved than the pre-edge of **FESALMP0**. There is very little change in the intensity of the pre-edge feature in going from the diferric to diferrous forms in the **FESALMP** models, but in the **FE2BIPHME** models, there is a loss in intensity. This reduction in intensity is counterintuitive to expectation, based on the change in the coordination of the iron atom which occurs in the diferrous form of **FE2BIPHME**. One of the hexacoordinate iron atoms becomes pentacoordinate in **FE2BIPHME**, and the decrease in the symmetry should result in an increase in the pre-edge intensity. The loss of the oxo-bridge which occurs upon reduction of **FE3BIPHME**, which would result in a decrease in the distortion of the iron site, may offset any gain in intensity due to the decrease in the coordination number. The intensities of the diferrous model pre-edge features are similar to each other, therefore it is unlikely that this information can be used to distinguish between symmetric and unsymmetric ferrous diiron sites.

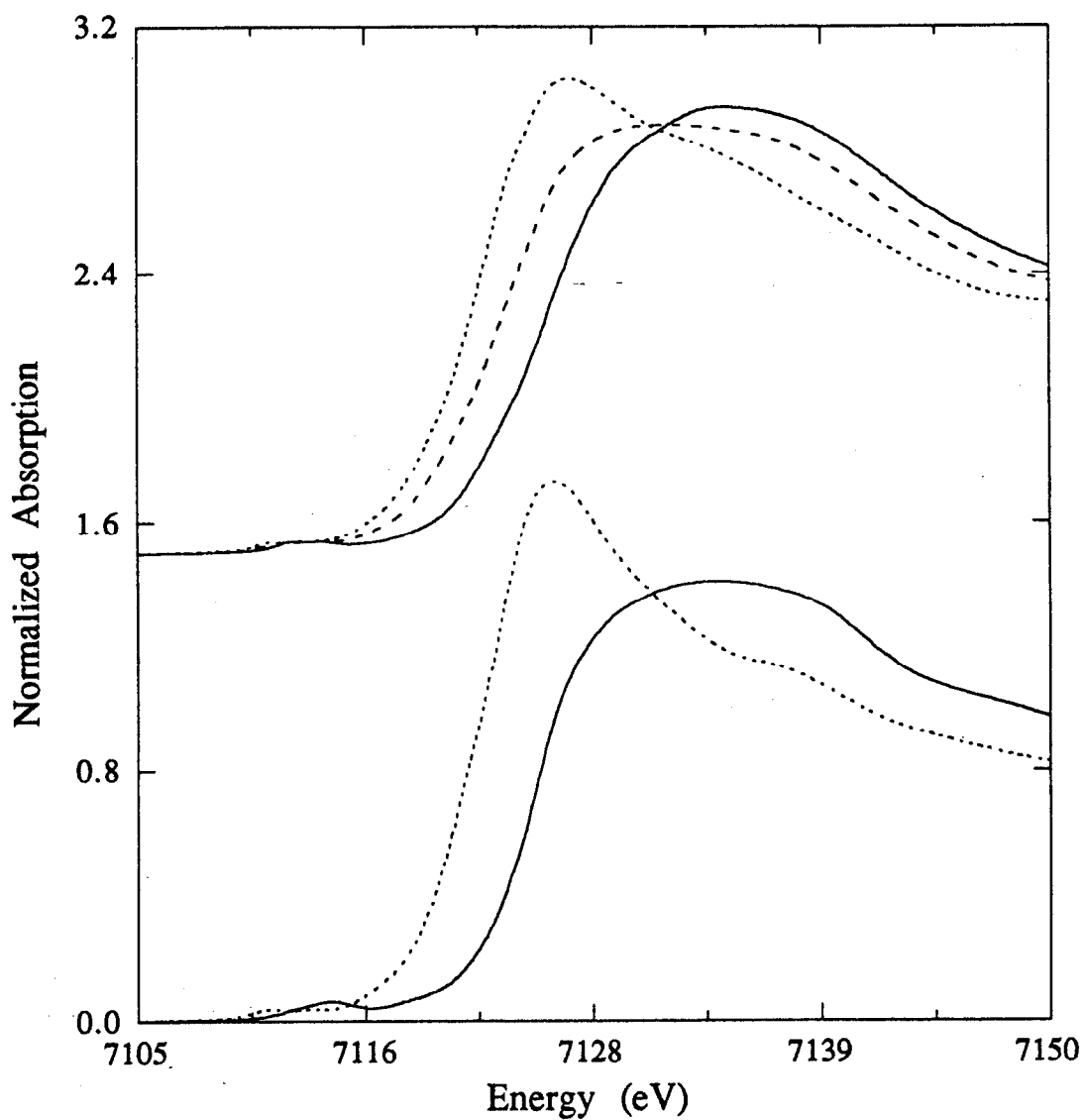


Figure 5.4. Changes in the edge spectra with change in oxidation state. The top curve shows the spectra of diferric Fe(III)Fe(III) **FESALMP0** (solid), semimet Fe(III)Fe(II) **FESALMP1** (dash), and diferrous Fe(II)Fe(II) **FESALMP2** (dot). The bottom curve shows the spectra of diferric **FE3BIPHME** (solid) and diferrous **FE2BIPHME** (dot).

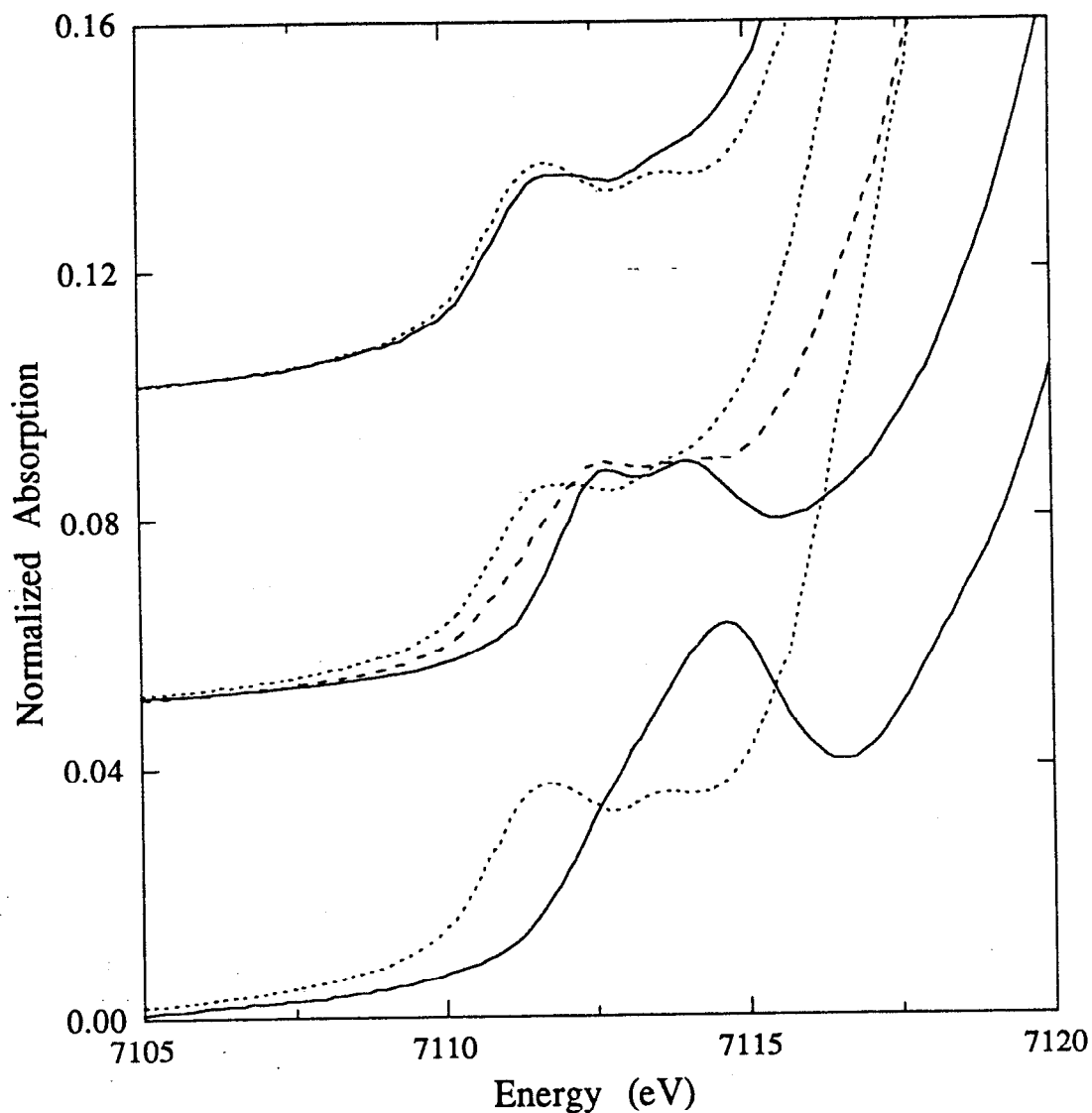


Figure 5.5. Changes in the pre-edge feature with change in oxidation state. The pre-edge of the diferric models **FESALMP2** (solid) and **FE2BIPHME** (dot) are compared in the top curve. The middle curve shows the pre-edge features of **FESALMP0** (solid), **FESALMP1** (dash) and **FESALMP2** (dot). The pre-edge features of **FE3BIPHME** (solid) and **FE2BIPHME** (dot) are compared in the bottom curve.

5.3.2. Interpretation of Edge Spectra

All of the compounds investigated had octahedral, or nearly octahedral coordination around the iron atoms and the edge spectra are relatively similar for all of the compounds studied here. The most dramatic change occurs in the pre-edge region, which will be discussed separately. The differences observed in the appearance of the edge structure can be correlated to the nature of the bridging groups in the diiron center and to changes in the relative numbers of N and O atoms ligated to the iron atoms.

5.3.2.1. Changes in the Edge Spectra with Bridging Geometry. The position of the edge (measured at an absorption value of 1/3) is correlated to the average first shell bond length for the models studied (Table 5.3 and Figure 5.6) with the exceptions of **FE2CO2** and **FESALMP0**. In general, the oxo-bridged models have longer average bond lengths than the non-oxo-bridged models due to the distortion of the site caused by the presence of the short Fe-O bond (see Table 4.1 in Chapter 4). **FE2CO2** is an exception to this observation due to the all O ligation which decreases the distortion effect of the oxo-bridge. The bond length of **FE2CO2** is similar to the bond lengths of the non-oxo-bridged models, but the edge position is similar to the oxo-bridged models. The average distance of **FESALMP0** is consistent with the lack of an oxo-bridge, but the position of the edge of is similar to the positions of the oxo-bridged model edges. Otherwise, however, the position of the edge moves to lower energy as the average first shell bond length increases. The increase in the average bond length is itself loosely correlated to the number of N and O atoms ligating the iron center.

The data available for a direct comparison of the effect of an oxo-bridge on the edge spectra of otherwise identical models is limited, however the number of bridges seems to have an effect on the appearance of the edges. In general, the appearance of the features in the edge spectra of the tribridged models are not as well-defined as in the edge spectra of the di- and mono-bridged models, although **FESALMP0** is an exception to this observation. For example, the edges of oxo-bridged **FEHBPZO** and hydroxo-bridged **FEHBPZOH** (both tribridged models) are more similar to each other (Figure 5.7, top curve) than **FEHBPZO** is to oxo-bridged **FETPAOAC** or **FEHBPZOH** is to hydroxo-bridged **FECHEL** (Figure 5.7, compare dotted lines and solid lines, respectively). In addition, the edges of **FETPAOAC** and **FECHEL** (both dibridged models) are relatively similar to each other (Figure 5.7, middle curve), although the edge of the oxo-bridged model is less intense and broader than the hydroxo-bridged model. Comparing the spectra of **FEHBPZO** and **FEHBPZOH**, a similar effect is seen, with the edge of the oxo-bridged model appearing wider than that of the analagous hydroxo-bridged model (Figure

Table 5.3. Comparison of Average First Shell Distance with Edge Position.

Sample	Coordination Environment	Avg. First Shell Distance ^a (Å)	Position of Edge ^b (eV)
OXO-BRIDGED MODELS			
FE ₂ CO ₂	6 O	2.02	7122.2
FE ₃ BIPHME	4 O, 2 N	2.05	7122.6
FEHBPZO	3 O, 3 N	2.06	7122.0
FETPAOAC	4 N, 2 O	2.07	7121.9
FETPACO ₃	4 N, 2 O	2.07	7121.7
FETPAPHT	4 N, 2 O	2.08	7121.5
NON-OXO-BRIDGED MODELS			
FEHEL	5 O, 1 N	2.02	7123.4
FEDIPIC	5 O, 1 N	2.03	7123.1
FESALMP0	4 O, 2 N	2.03	7122.2
FEHBPZOH	3 O, 3 N	2.04	7123.1
HYDROXYLASE SAMPLE			
EXAFS5	6 N/O	2.04	7122.6

^aThe average distance includes all first shell distances from the crystal structures of the models. ^bThe edge position was measured at an intensity value of 1/3. ^cThe data for the hydroxylase sample was determined by EXAFS (see Chapter 2).

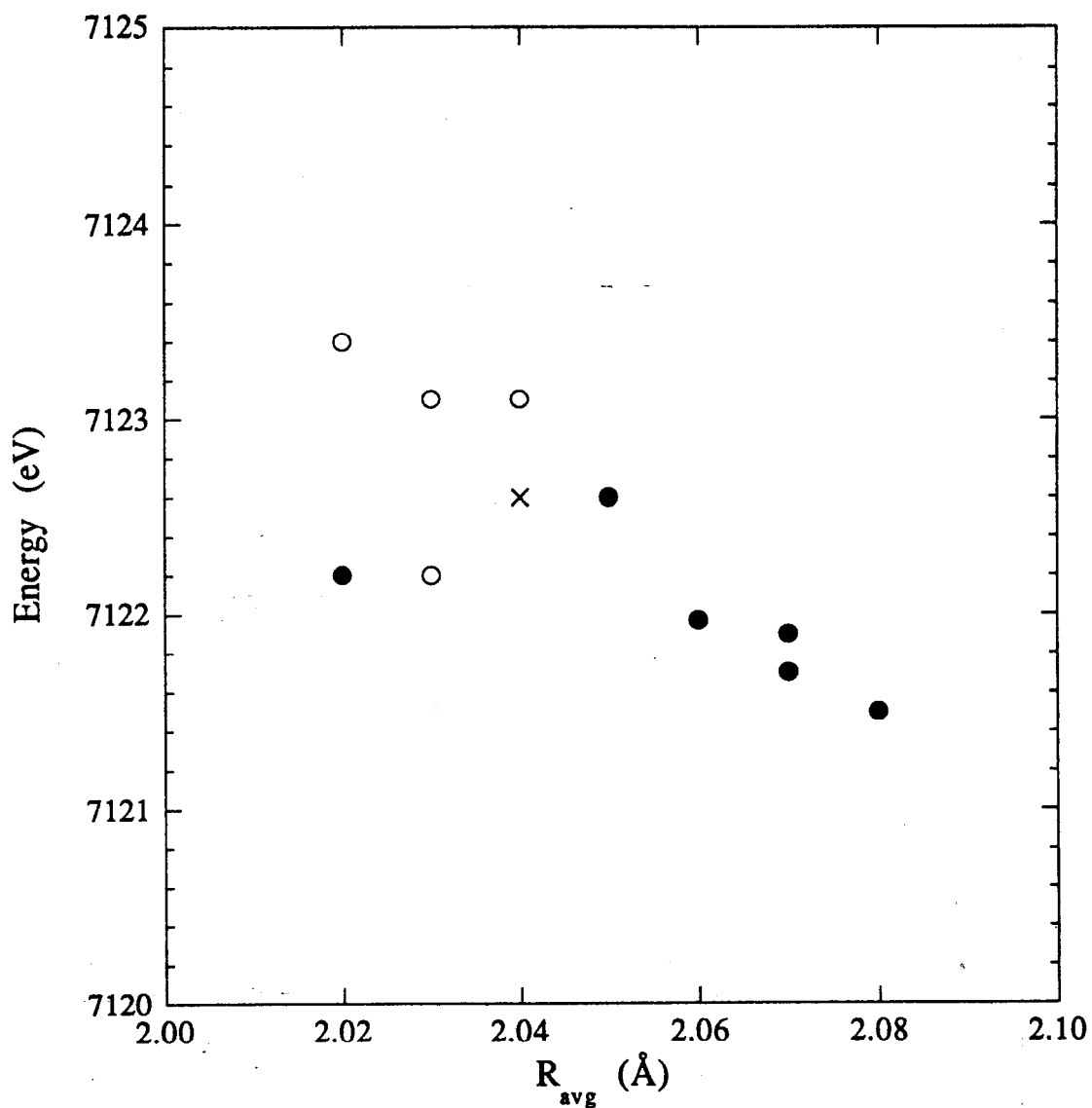


Figure 5.6. A comparison of the average first shell distance with edge position. The solid circles are data for oxo-bridged models. The open circles are data for non-oxo-bridged models. The x is the oxidized hydroxyase data.

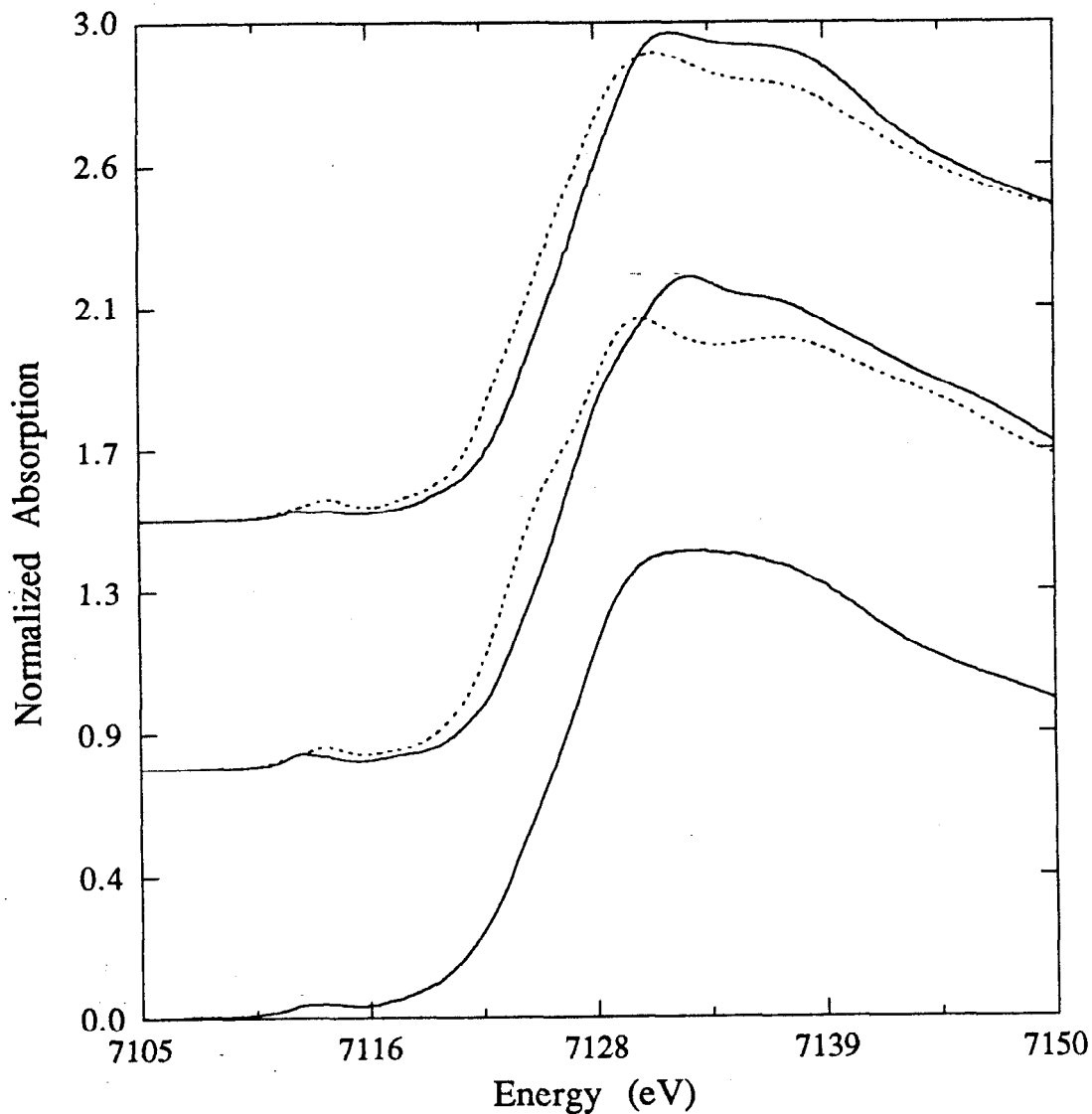


Figure 5.7. Comparisons of model and MMO hydroxylase edges. The solid lines are spectra of non-oxo-bridged models, while the dotted lines are oxo-bridged model spectra. The top curve compares the edge spectra of tribridged models **FEHBPZOH** (solid) and **FEHBPZO** (dot). The middle curve compares the edge spectra of dibridged models **FEHEL** (solid) and **FETPAOAC** (dot). The edge spectrum of the oxidized hydroxylase sample **EXAFS5** is presented in the lower curve, and more resembles the spectra of the tribridged models presented in the top curve.

5.7, top curve). It should be noted that the ligation of the iron center also changes for FETPAOAC (4 N/2 O) and FECHL (5 O/1 N) in addition to the types of bridges changing, which introduces another variable into the comparison.

5.3.2.2. Changes in the Edge Spectra with Changes in Ligation. The appearance of the shoulder on the rising edge in the oxo-bridged models (Figure 5.1) corresponded to the increase in the number of N atoms relative to O atoms in the first coordination sphere, suggesting that this feature may be related to changes in the covalency of the active site due to differences in the ligation sphere. Similar effects in the edge spectra of Ni,⁷ Cu,⁴ and Fe⁹ models and proteins have been seen with changes in the ligation of the metal center which have been attributed to an increase in the covalency of the metal site. In the Ni and Cu compounds studied, this shoulder has been interpreted as a ligand-to-metal charge transfer shake down feature associated with the $1s \rightarrow 4p$ transition. A similar interpretation of the feature for the oxo-bridged dinuclear iron centers could apply here as well. No such change in the edge spectra was seen in the non-oxo-bridged compounds as a result of changing ligation sphere, however, the spectrum of dibridged FECHL has a weak shoulder, whereas the spectrum of tribridged FEHBPZO does not. This suggests that the decrease in the number of bridges may also impact the presence of the shoulder, perhaps reflecting greater distortion in the diiron center imposed by the bridging geometry. This interpretation is consistent with the greater intensity of the $1s \rightarrow 3d$ pre-edge feature of FECHL relative to FEHBPZO (Figure 5.2, middle curve).

5.3.2.3. Pre-edge Feature. The intensity of the pre-edge feature is gained by the non-centrosymmetric character of the Fe site in the iron dimers which allows 4p and 3d mixing to occur. The intensity of the pre-edge feature is related to the amount of 4p mixing into the 3d orbitals and is inversely proportional to the coordination number of the metal site.^{3,5} For the models studied here, the coordination number is 6 in every case so any variation in the intensity of the pre-edge feature reflects the amount of distortion around the iron site. The edge spectrum of oxo-bridged model FEHBPZO and hydroxo-bridged model FEHBPZO are compared in Figure 5.5a. Both of these compounds are coordinated by 3 N and 3 O atoms. The intensity of the pre-edge feature in the oxo-bridged model is greater than the intensity in the non-oxo-bridged model, reflecting the increased distortion of the iron site due to the presence of the short oxo-bridge (see Table 4.1 in Chapter 4). In the oxo-bridged model, the average first shell distances range from 1.79 to 2.19 Å (0.4 Å difference), while in the hydroxo-bridged model, the average first shell distances range from 1.96 to 2.11 Å (0.15 Å difference). In addition, the pre-edge features of the non-oxo-bridged models are very similar to the pre-edge feature of Fe(acac)₃²² (Figure 5.2, bottom curve), a monomeric octahedral compound coordinated by 6 O atoms

whose bond lengths range from 1.986 to 2.004 Å. The presence of the pre-edge feature in the $\text{Fe}(\text{acac})_3$ compound reflects the sensitivity of the transition to slight symmetry distortions.

The pre-edge feature is clearly split in all non-oxo-bridged models, and asymmetric in all oxo-bridged models (Figure 5.2). The appearance of this feature is therefore characteristic of the nature of the bridge in the iron center, but not of the number of bridges. There are two possible explanations for the splitting seen in the pre-edge feature. One is that each transition corresponds to the $1s \rightarrow 3d$ transition for each iron atom in the dimer. This doesn't seem very likely as the edge spectra seen will be the average for both iron atoms and the individual iron sites within each dimer are very nearly identical to each other. In addition, the presence of a split pre-edge feature in monomeric $\text{Fe}(\text{acac})_3$ argues against this explanation. The alternative explanation is that the transitions seen are to different molecular states in the final d-state configuration.

The transition which occurs in the pre-edge region is from an initial $[1s^2...3d^5]$ state to a final $[1s^1...3d^6]$ state and will occur to states of maximum spin multiplicity. In the free ion limit, only the 5D state is available, however at somewhat stronger fields (but still in the weak field limit), transitions can occur to the $^5T_{2g}$ and 5E_g molecular states. The splitting seen in the pre-edge region of the edge spectra is therefore consistent with transitions to the $^5T_{2g}$ and 5E_g states ($^5T_{2g} < ^5E_g$). The energy splittings seen in the pre-edge region of the diferric dimers were between 1.6 and 2.2 eV ($\sim 13,000 - 17,700 \text{ cm}^{-1}$), which correspond to D_q/B values in the range from 1.3 to 1.75. These values are consistent with the high-spin character of these model compounds. The electronic configuration which gives rise to the $^5T_{2g}$ and 5E_g molecular states are $(t_2^4e^2)$ and $(t_2^3e^3)$, respectively, so the energy splittings observed in the pre-edge correspond to $10Dq$ for the various model compounds.

The overall increase in intensity of the pre-edge feature for the oxo-bridged model spectra over the non-oxo-bridged models can be explained by the increased distortion of the Fe site due to the presence of the short Fe-O_{oxo} bridging distance. In the spectra of the non-oxo-bridged models, the transition to the $^5T_{2g}$ state is the most intense, while the transition to the 5E_g state is the most intense in the spectra of the oxo-bridged models. The intensity differences may reflect a greater amount of 4p mixing into the 5E_g final state over the $^5T_{2g}$ state for the oxo-bridged models due to the lowering of the symmetry of the iron atoms caused by the presence of the oxo-bridge.

In the diferrous systems, splitting in the pre-edge region has commonly been attributed to transitions to the free ion 4F and 4P states of the d^7 excited state configuration.¹⁰ The relative intensities of the two transitions has been calculated to be 7:3

for F:P ($4F < 4P$), so the higher energy transition should be less intense. This is the case for the ferrous models (Figure 5.5, top curve). The magnitude of the splitting seen (2.1 and 2.2 eV) is consistent with the energy difference expected for the $4F$ and $4P$ levels. Alternatively, the transitions seen could be to the $4T_{1g}$ and $4T_{2g}$ molecular states which correspond to D_q/B values of 1.8 and 1.9. These values of D_q/B are consistent with the high-spin character of the model compounds but correspond to $10D_q$ values of $\sim 16,500$ cm^{-1} for **FE2BIPHME** and $\sim 17,400$ cm^{-1} for **FESALMP2**, somewhat greater than the corresponding ferric models ($10D_q$ for **FE3BIPHME** and **FESALMP0** was calculated to be $\sim 15,000$ cm^{-1}). This is not consistent with the relative positions of Fe^{+2} and Fe^{+3} in the spectrochemical series and supports the assignment of the transitions as corresponding to the free ion $4F$ and $4P$ states.

5.3.2.4. Comparisons with Hydroxylase Edge Spectra. The edge spectrum of the oxidized hydroxylase is included in Figure 5.7 for comparison the the dimer edges. The appearance of the hydroxylase spectrum is most similar to tribridged **FEHBPZOH** and **FEHBPZO** and to dibridged **FESALMP0** (shown in Figure 5.4, top curve). It is not clear why the spectrum of **FESALMP0** is less distinct than the other models, but may reflect the extended bridges in the structure (see Table 5.2). The pre-edge features of these four samples are compared in Figure 5.8 (bottom curve). The pre-edge feature of the hydroxylase is asymmetric and the higher energy region is more intense than the lower energy region, similar to oxo-bridged model pre-edge features. The overall intensity of the hydroxylase pre-edge feature is more like the non-oxo-bridged model pre-edge features. The hydroxylase data are certainly more consistent with the lack of an oxo-bridge in the iron center, however the exact nature of the bridging geometry is not revealed by this analysis. Inclusion of the diferric hydroxylase on the plot in Figure 5.6 (represented as an x) using the average first shell distance of 2.04 Å determined by EXAFS analysis (see Chapter 2) is also consistent with the lack of an oxo bridge in the diiron site. The EXAFS analysis clearly shows that there is no oxo bridge in the iron center (Chapter 2).

The main transition in the diferrous hydroxylase edge is sharper than in the edge spectrum of either **FESALMP2** or **FE2BIPHME**, and lacks the high energy shoulder seen at around 7135 eV (see Figure 5.4 in Chapter 2). The edge of the semimet hydroxylase appears to be a little broader on the rising edge than the edge of the oxidized hydroxylase. The change in the edge of the hydroxylase with reduction to the semimet and diferrous state is similar to the change seen for the **FESALMP** and **FEBIPHME** models (compare Figure 5.4 with Figure 5.4 in Chapter 2). The intensity of the pre-edge features in both the semimet and reduced hydroxylase spectra is greater than the intensity of the

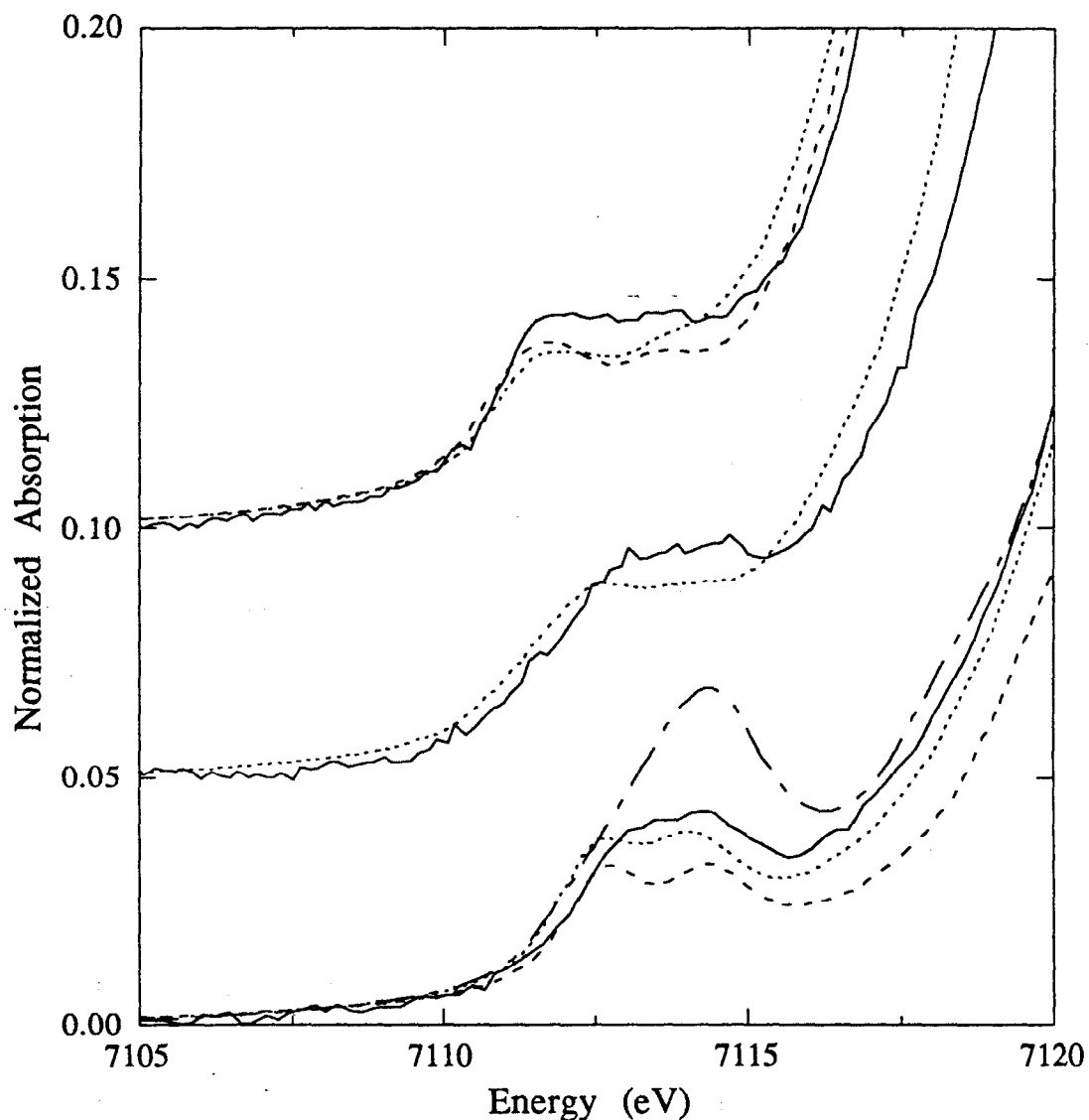


Figure 5.8. A comparison of the pre-edge features of the models and the MMO hydroxylase samples. The solid lines are the protein spectra. The top curve compares the reduced hydroxylase sample EXAFS6 (solid) with FESALMP2 (dot) and FE2BIPHME (dash) and the middle curve compares the semimet hydroxylase sample EXAFS7 (solid) with FESALMP1 (dot). The bottom curve compares the feature of oxo-bridged FEHBPZO (dash-dot) with the oxidized hydroxylase sample EXAFS5 (solid) and the non-oxo-bridged models FEHBPZOH (dash) and FESALMP0 (dot).

corresponding model compounds (Figure 5.8, top curve for reduced samples, middle curve for semimet samples), suggesting that the coordination or symmetry of the hydroxylase diiron center may be different than in the model compounds, however the difference may be due to subtraction of the different background contributions for transmission (model) data and fluorescent (protein) data are different.

5.4. Conclusions

The appearance of the Fe K-edge XANES spectra of the model compounds is related to the nature of the bridges in the diiron center and with the ligation of the iron atoms. In general, the features in the spectra are more well-defined for the dibridged models than the tribridged models (compare upper and lower curves in Figures 5.1 and 5.3). The presence of an oxo bridge tends to broaden the edge somewhat over the edges of the non-oxo-bridged models (Figure 5.7). The appearance of a shoulder on the rising edge of the spectra reflects a decrease in the number of bridges in the non-oxo-bridged models. In the oxo-bridged models, the appearance of the shoulder was correlated with the increase in the N ligation of the iron center. A reasonable interpretation of this feature is that it is a shake down feature associated with the $1s \rightarrow 4p$ transition, and reflects an increase in the covalency of the iron site due to the change in the ligation. The final assignment of this feature as a shake down transition awaits confirmation by XPS/PES experiments. The position of the edge decreases in energy as the average first shell distance in the models decreases, and is related to the presence or absence of a μ -oxo bridge in the center.

The appearance of the pre-edge feature is characteristic only of the presence or absence of a μ -oxo bridge in the diferric center and not of the number of bridges in the diiron site. In oxo-bridged compounds, the pre-edge feature is asymmetric with the most intense transition occurring at ~ 7114 eV. In the non-oxo-bridged compounds, the pre-edge feature is clearly resolved into a doublet with the lower energy transition (~ 7113 eV) having more intensity than the 7114 eV transition. The splitting of the transitions is consistent with the assignment of the transition to the ${}^5T_{2g}$ and 5E_g molecular states for the excited state d^6 configuration. The greater overall intensity of the oxo-bridged models is consistent with the increased distortion of the iron site over the non-oxo-bridged models due to the presence of the short Fe-O bridge. Additionally, the differences in the relative intensities of the two pre-edge transitions for the oxo- and non-oxo-bridged models probably arises from differences in the site symmetry of the iron atoms which impacts the amount of 4p mixing into the different molecular states. For the diferrous model, a reasonable interpretation of the split transition is that it occurs to the free ion 4F and 4P

molecular states. The intensity of this feature is similar for both symmetrically substituted **FESALMP2** and asymmetrically substituted **FE2BIPHME**, making conclusions about the coordination of the iron atoms in the reduced state difficult based on the pre-edge information.

The diferric hydroxylase edge is most consistent with the lack of an oxo-bridge in the diiron center, supporting the results from the EXAFS analysis (Chapter 2). The shape of the pre-edge feature is reminiscent of an oxo-bridged compound, but the intensity is more like **FESALMP0** and **FEHBPZOH**, suggesting the octahedral symmetry of the iron site in the hydroxylase is more like that in the latter models. The changes in the edge seen with reduction of the diferric state to the diferrous state are similar for the protein and model compounds. The greater intensity of the pre-edge features of the semimet and reduced hydroxylase samples compared to the semimet and reduced models may reflect lower coordination or symmetry at the Fe center in the protein samples. A systematic study of the edge structure of reduced and semimet model compounds would greatly aid in the interpretation of the edge structure of these forms of the protein samples.

5.5. Acknowledgements

The data were collected at the Stanford Synchrotron Radiation Laboratory and the National Synchrotron Light Source, Brookhaven National Laboratory, which are supported by the Department of Energy, Office of Basic Energy Sciences, Division of Chemical Sciences and Division of Materials Sciences. SSRL is also supported by the National Institutes of Health, Biomedical Resource Technology Program, Division of Research Resources (RR-01209) and by the Department of Energy, Office of Health and Environmental Research. Grant support was provided by the National Science Foundation (CHE 91-21576 to KOH). The author wishes to thank Profs. Stephen J. Lippard and Richard Holm for the gifts of model compounds, and Susan E. Shadle for helpful discussions.

5.6. References and Notes

1. Cotton, F. A.; Ballhausen, C. J. *J. Chem. Phys.* **1956**, *25*, 617-623.
2. Seka, W.; Hanson, H. P. *J. Chem. Phys.* **1969**, *50*, 344-350.
3. Srivastava, U. C.; Nigam, H. L. *Chem. Coord. Rev.* **1972**, *9*, 275-310 and references therein.
4. Kau, L.-S.; Spira-Solomon, D. J.; Penner-Hahn, J. E.; Hodgson, K. O.; Solomon, E. I. *J. Am. Chem. Soc.* **1987**, *109*, 6433-6442.
5. Penner-Hahn, J. E.; Fronko, R. M.; Pecoraro, V. L.; Yocum, C. L.; Betts, S. D.; Bowlby, N. R. *J. Am. Chem. Soc.* **1990**, *112*, 2549-2557.
6. Tan, G. O.; Ensign, S. A.; Ciurli, S.; Scott, M. J.; Hedman, B.; Holm, R. H.; Ludden, P. W.; Korszun, Z. R.; Stephens, P. J.; Hodgson, K. O. *Proc. Natl. Acad. Sci. USA* **1992**, *89*, 4427-4431.
7. Colpas, G. H.; Maroney, M. J.; Bagyinka, C.; Kumar, M.; Willis, W. S.; Suib, S. L.; Baidya, N.; Mascharak, P. K. *Inorg. Chem.* **1991**, *30*, 920-928.
8. (a) Lippard, S. J. *Angew. Chem. Int. Ed. Engl.* **1988**, *27*, 344-361. (b) Sanders-Loehr, J. *Iron Carriers and Iron Proteins*; VCH Publishers Inc.: New York, 1989; pp. 373-466. (c) Que, L., Jr.; True, A. E. *Prog. Inorg. Chem.* **1990**, *38*, 97-200.
9. DeWitt, J. G.; Bentsen, J. G.; Rosenzweig, A. C.; Hedman, B.; Green, J.; Pilkington, S.; Papaefthymiou, G. C.; Dalton, H.; Hodgson, K. O.; Lippard, S. J. *J. Am. Chem. Soc.* **1991**, *113*, 9219-9235.
10. Shulman, R. G.; Yafet, Y.; Eisenberger, P.; Blumberg, W. E. *Proc. Natl. Acad. Sci. USA* **1976**, *73*, 1384-1388.
11. This feature could also be due to a quadropole transition, in which case the selection rule is $\Delta l = 2$ and the $1s \rightarrow 3d$ transition is allowed. The authors of reference 10 have estimated that the quadropole transitions would be three orders of magnitude weaker than the intensity of the Fe preedge feature, and concluded that the feature is due to an Fe $1s \rightarrow 3d$ transition made allowed by vibronic coupling of the 4p and 3d states.
12. Cotton, F. A.; Hanson, H. P. *J. Chem. Phys.* **1958**, *28*, 83-87.
13. Hahn, J. E.; Scott, R. A.; Hodgson, K. O.; Doniach, S.; Desjardins, S. E.; Solomon, E. I. *Chem. Phys. Lett.* **1982**, *88*, 595-598.
14. Roe, A. L.; Schneider, D. J.; Mayer, R. J.; Pyrz, J. W.; Que, L. Jr. *J. Am. Chem. Soc.* **1984**, *106*, 1676-1681.

15. Smith, T. A.; Penner-Hahn, J. E.; Hodgson, K. O.; Berding, M. A.; Doniach, S. *Springer Proc. Phys.* **1984**, *2*, 58-60.
16. Waychunas, G. A.; Brown, G. E. Jr. *Phys. Chem. Minerals* **1990**, *17*, 420-430.
17. Blair, R. A.; Goddard, W. A. *Phys. Rev. B* **1980**, *22*, 2767-2776.
18. Shadle, S. E.; Penner-Hahn, J. E.; Schugar, H. J.; Hedman, B.; Hodgson, K. O.; Solomon, E. I. *J. Am. Chem. Soc.* accepted for publication, 1992.
19. (a) Feng, X.; Bott, S. G.; Lippard, S. J. *J. Am. Chem. Soc.* **1989**, *111*, 8046-8047. (b) Armstrong, W. H.; Spool, A.; Papaefthymiou, G. C.; Frankel, R. B.; Lippard, S. J. *J. Am. Chem. Soc.* **1984**, *106*, 3653-3667. (c) Tolman, W. B.; Bino, A.; Lippard, S. J. *J. Am. Chem. Soc.* **1989**, *111*, 8522-8523. (d) Armstrong, W. H.; Lippard, S. J. *J. Am. Chem. Soc.* **1984**, *106*, 4632-4633. (e) Thich, J. A.; Ou, C. C.; Powers, D.; Vasilou, B.; Mastropaolo, D.; Potenza, J. A.; Schugar, H. J. *J. Am. Chem. Soc.* **1976**, *98*, 1425-1433. (f) Snyder, B. S.; Patterson, G. S.; Abrahamson, A. J.; Holm, R. H. *J. Am. Chem. Soc.* **1989**, *111*, 5214-5223. (f) Bertrand, J. A.; Breece, J. L.; Eller, P. G. *Inorg. Chem.* **1974**, *13*, 125-131. (g) Norman, R. E.; Yan, S.; Que, L. Jr.; Backes, G.; Ling, J.; Sanders-Loehr, J.; Zhang, J. H.; O'Connor, C. J. *J. Am. Chem. Soc.* **1990**, *112*, 1554-1562. (h) Norman, R. E.; Holz, R. C.; M'enage, S.; O'Connor, C. J.; Zhang, J. H.; Que, L. Jr. *Inorg. Chem.* **1990**, *29*, 4629-4637. (i) Gaines, A.; Hammett, L. P.; Walden, G. H. *J. Am. Chem. Soc.* **1936**, *58*, 1668-1674. (j) Armstrong, W. A.; Lippard, S. J. unpublished results
20. Scott, R. A.; Hahn, J. E.; Doniach, S.; Freeman, H. C.; Hodgson, K. O. *J. Am. Chem. Soc.* **1982**, *104*, 5364-5369.
21. The second derivative of the edge spectra of all of the models does indicate the presence of a feature in the 7122.7 to 7124.8 eV range which is not seen in the edge spectra themselves.
22. (a) Iball, J.; Morgan, C. H. *Acta Cryst.* **1976**, *23*, 239-244. (b) Roof, Jr., R. B. *Acta Cryst.* **1956**, *9*, 781-786.

Chapter 6

Sulfur and Chlorine K-Edge X-ray Absorption Spectroscopic Studies of Photographic Materials

6.1. Introduction

Sulfur is present in several important components of the photographic system including spectral sensitizing dyes and chemical sensitizing centers. These components exist at the surface of the photoactive silver halide crystals and are involved in electron and energy transfer processes. It is therefore likely that the surface structure and electronic environment of these sensitizing dyes and centers will have an effect on photographic performance. X-ray absorption spectroscopy (XAS) studies can directly probe the local geometric and electronic structure of these important surface-active species on the photoactive substrate.

Previous sulfur XAS studies have shown that the S K-edge has sharp absorption features in the edge and near-edge region arising from bound-state transitions from the sulfur 1s orbital to low-lying unoccupied or partially occupied atomic or molecular orbitals. These features have been shown to be very dependent on the local geometry and oxidation state of the absorbing atom.^{1,2,3} With a spectrometer energy resolution of 0.5 eV at these energies (2-3 keV), shifts of as much as 13 eV have been seen with a change in the oxidation state of sulfur from -2 to +6.

Studies of the sulfur K-edge of numerous organic and inorganic compounds have revealed characteristic absorption spectra dependent on the nature of sulfur in the compound, making XAS a useful tool in determining the forms and relative amounts of sulfur present in petroleum asphaltenes and coal.⁴ Polarized K-edge measurements together with theoretical calculations using a multiple-scattered wave X- α formalism have resulted in assignments of some of these S K-edge features.⁵ A number of soft X-ray studies have been done on gaseous⁶ and surface-adsorbed^{6a,7} organic and inorganic sulfur-containing molecules, such as thiols, thioethers, and sulfur halides. These studies provide further insight into the origin and nature of the S K-edge features, including information about the symmetry of the final state orbitals to which the transition occurs, and the orientation dependence of the edge features of adsorbed species.^{6a,6b,8}

Spectral sensitizing dyes are used in many applications such as non-linear optics, solar energy conversion, electrophotography and silver halide photography. Merocyanine and cyanine dyes extend the response of photographic materials beyond the intrinsic blue/ultraviolet absorption of the silver halide photoconductor into the visible and infrared regions. The spectral sensitivity imparted to the silver halide substrate depends on the visible absorption properties of the dye molecules. Spectral shifts of the visible absorption features to longer wave-lengths result from the aggregation of the dye molecules on the surface, and depend on both the concentration and the orientation of the dye molecules.

The degree and extent of aggregation, and consequently of the spectral shift, is in part determined by silver halide morphology, the presence of other adsorbates, and structural features of the dye molecules themselves.⁹ Structural properties of dye molecules which are important for aggregation formation include extended delocalization of π electrons, planarity of the molecule, and reduction of positional isomers.

The sensitization process involves the transfer of electrons or energy as an exciton from the photoexcited state of the dye molecule aggregate into the conduction band of the silver halide substrate. For well-ordered, strongly interacting molecular systems, excitons are transferred via coupled oscillations of the molecules in a time period shorter than the period of the molecular vibrations. The transfer of the exciton from the dye aggregate to the substrate conduction band requires that the dye molecules exist in an adsorbed state on the surface of the silver halide grains. The nature of the interaction between the dye aggregates and the silver halide substrate has been the subject of many studies. For dyes containing benzthiazole groups (belonging to the cyanine dye class), it has been postulated that the adsorbed dye molecules are oriented with their sulfur atoms directed toward the silver halide surface.^{10,11} XPS experiments of dyed AgCl crystals¹² and electrophoretic mobilities of dyed silver halide grains¹³ have suggested that direct interaction between the sulfur atoms and the silver ions on the crystal surface is a driving force in the adsorption process and a determining factor in the orientation of dye molecules on silver halide crystal faces.

Another important process in photography is latent image formation. Latent image formation involves the reduction of Ag^+ to Ag^0 which appear as dark areas on negatives and are invisible until the film is exposed to developer. The aggregates of Ag metal are referred to as latent image centers. The efficiency of formation of latent image centers is related to the size of the Ag metal aggregates and the competition between combination of the photoelectron with Ag^+ and electron-hole recombination. The efficiency of latent image formation, which means that less exposure time is required to form an image, can be improved by the formation of chemical sensitization centers on the silver halide surface.

Chemical sensitization centers are formed by the treatment of silver halide crystals with aqueous solutions of labile sulfur-containing compounds such as thiosulfate and thioureas. The sensitization centers are believed to be silver sulfide specks on the silver halide surface which act as electron traps for photoelectrons.¹⁴ The electron-trapping capabilities of these centers result in a reduction in the electron-hole recombination rate which improves the efficiency of latent image formation, and they may also promote or stabilize latent image center formation. The highest degree of chemical sensitization is

achieved with a combination of sulfur compounds and gold-containing salts, however the nature of these chemical sensitization centers is not well understood.

We have used S and Cl K-edge XAS to characterize the electronic and geometric structure of a wide variety of compounds important to the photographic system, including cyanine and merocyanine dyes and dye intermediates, and thiol- and thione-containing molecules. The nature of the interaction between the metal ions and the forms of sulfur of importance in the photographic system have been studied by S K-edge XAS measurements on silver and gold complexes of sulfides, thiazoles, and thiol- and thione-containing ligands. Oriented single-crystal polarized studies of representative dye nuclei and a metal-sulfur compound have been used to determine the angular dependence of the features seen in powder spectra. These studies permit assignments of the features and provide a basis for interpreting polarized measurements of dye molecules and chemical sensitization centers on silver bromide sheet crystals.

6.2. Experimental

The samples discussed in this paper are presented in Tables 6.1-6.4. The dye samples (Tables 6.1 and 6.2) were measured to be 90% pure by HPLC. All of the samples with the exception of 9,10-dichloroanthracene were supplied by Eastman Kodak Co. Single crystals of 2-thiohydantoin¹⁵ (IM4) were obtained from ethanol as orange rhombic plates with sides 1-2 mm long and 0.3 - 0.5 mm thick. Yellow needles of 3,3'-diethylthiacyanine bromide¹⁶ (DC5) were obtained from propanol (1-2 mm x ~ 0.25 mm x ~ 0.25 mm). Single crystals of 9,10-dichloroanthracene¹⁷ (DCA) were obtained from saturated petroleum ether solutions of the compound placed in a desiccator containing scraps of paraffin. The crystals were yellow plates of dimensions 1 - 2 mm x 0.3 mm x < 0.3 mm. White single crystals of bis(ethylenethiourea) gold (I) chloride hydrate¹⁸ were obtained from water. The crystals were parallelograms, 2 mm x 1 mm x 0.5 mm. The integrity of the crystals after exposure to synchrotron radiation was verified by checking that degradation of the diffraction quality of the crystal had not occurred, and by confirming the unit cell dimensions using a diffractometer after the conclusion of the experiments. AgBr sheet crystals (50 μ thick) were grown on quartz plates using a growth gradient technique. The dyed surface samples were prepared by submerging the sheet crystal in 10^{-5} M aqueous solutions of the dyes (20 minutes at 40° C). The chemically sensitized samples were prepared by submerging the sheet crystals in 10^{-5} M aqueous solutions of sodium thiosulfate or aurous dithiosulfate (20 minutes at 50° C).

Table 6.1. Energies of Transitions in S K-Edge Spectra of Cyanine Dyes and Dye Intermediates.

Compound	Structure	Sample name	Feature A (*) (eV)	Feature B (eV)
2-(2-anilinoethyl)-3-methylthiazolium iodide		IC1	2473.3	2475.2
2-acetylthiazole-3-ethylbenzotriazoline		IC2	2474.0	2476.1
2-acetylthiazole-1-ethylnaphtho[1,2-d]thiazoline		IC3	2474.0	2476.2
5-chloro-1,3,3'-triethylbenzimidazolothiacarbocyanine iodide		DC1	2473.8	2475.8

Table 6.1. continued

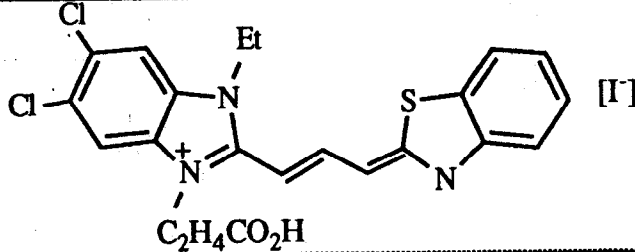
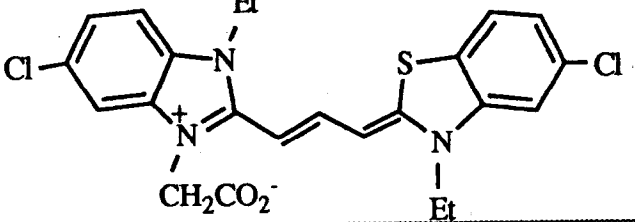
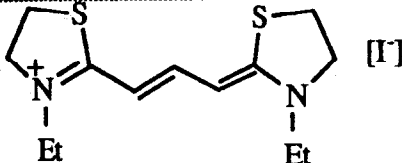
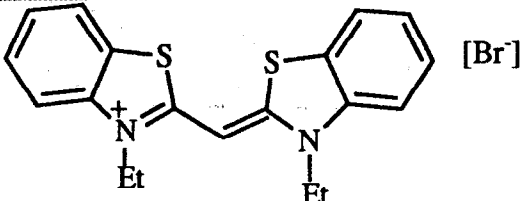
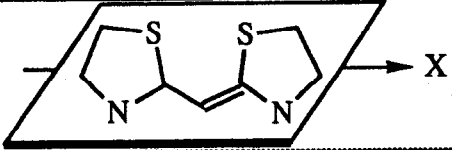
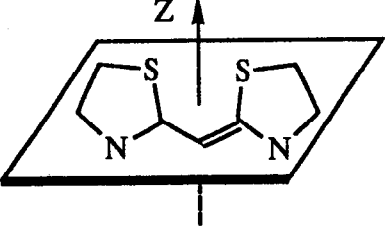
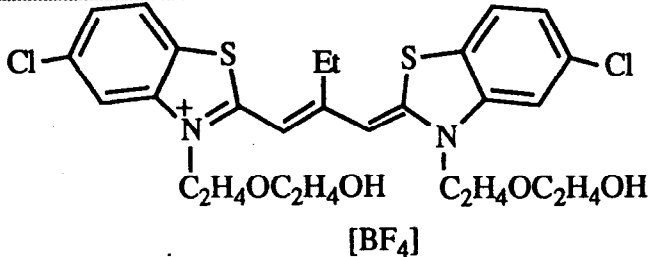
Compound	Structure	Sample name	Feature A (*) (eV)	Feature B (eV)
1-(2-carboxyethyl)-5,6-dichloro-3,3'-diethylbenzimidazolo-thiacarbocyanine iodide		DC2	2473.9	2476.0
Anhydro-3-carboxymethyl-5,5'-dichloro-3'-ethylthiacyanine hydroxide		DC3	2473.8	2475.8
1,1'-diethyl-2,2'-thiazoline carbocyanine iodide		DC4	2473.5	2475.3
3,3'-diethylthiacyanine bromide		DC5	2473.8	2475.6 2476.4

Table 6.1. continued

Compound	Structure	Sample name	Feature A (*) (eV)	Feature B (eV)
3,3'-diethylthiacyanine bromide in-plane orientation		DC5X	2473.5	2475.1
3,3'-diethylthiacyanine bromide out-of-plane orientation		DC5Z	2473.9	2475.6 (sh) 2476.5
5,5'-dichloro-3,3'-2(2-hydroxyethoxy)ethyl-9-ethylthiacarbocyanine tetrafluoroborate		DC6	2474.1 2473.2 (sh)	2476.1

*most intense feature

Table 6.2. Energies of Transitions in S K-Edge Spectra of Compounds Containing Exocyclic S.

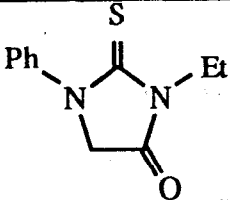
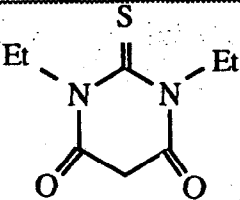
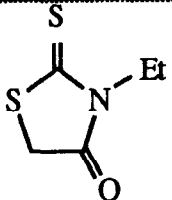
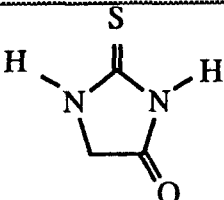
Compound	Structure	Sample name	Feature A' (eV)	Feature A (eV)	Feature B (eV)
Merocyanine Dyes and Dye Intermediates:					
3-ethyl-1-phenyl-2-thiohydantoin		IM1	2471.3*	2473.6	2475.6 (sh) 2477.3
1,3-diethyl-2-thiobarbituric acid		IM2	2471.1*	2473.9	2476.2 (sh) 2478.1
3-ethylrhodanine		IM3	2470.7	2473.4*	2475.4 (sh) 2478.0
2-thiohydantoin		IM4	2471.4	2473.8*	2477.5

Table 6.2. continued

Compound	Structure	Sample name	Feature A' (eV)	Feature A (eV)	Feature B (eV)
2-thiohydantoin, X orientation in-plane, along C=S		IM4X	2471.3 (sh)	2473.8*	2475.9(sh) 2477.8
2-thiohydantoin, Y orientation in-plane, perp. to C=S		IM4Y	2471.2 (sh)	2473.7*	2476.5
2-thiohydantoin, Z orientation out-of-plane		IM4Z	2471.3*	2473.4 (sh)	2477.4
5-[(5,7-dichloro-3-ethyl-2-benzoxazolinylidene)-ethylidene]-1,3-diethyl-2-thiobarbituric acid		DM1	2470.5 2471.9 (sh)	2473.6*	2478.2

Table 6.2. continued

Compound	Structure	Sample name	Feature A' (eV)	Feature A (eV)	Feature B (eV)
5-(5,6-dichloro-1,3-diethyl-2-benzimidazolinylidene)-3-ethyl-2-thio-2,4-oxazolindione		DM2	2471.4	2473.7*	2477.3
5-(5,6-dichloro-1,3-diethyl-2-benzimidazolinylidene)-3-ethyl-1-phenyl-2-thiohydantoin		DM3	2471.2	2473.4*	2477.0
4-[(5-chloro-3-ethyl-2-benzoxazolinylidene)-ethylidene]-3-methyl-1-phenyl-2-thiohydantoin		DM4	2470.9 2472.4 (sh)	2474.0*	2476.6
Thioureas and other thione-containing compounds:					
thiourea		THIOUR	2472.0	2473.2	2475.7 (sh) 2477.5*

Table 6.2. continued

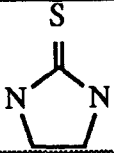

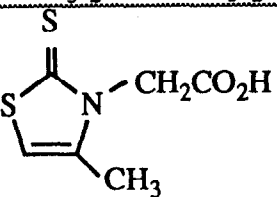
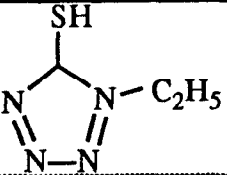
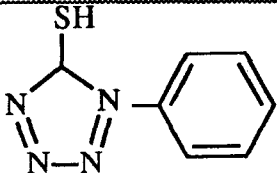
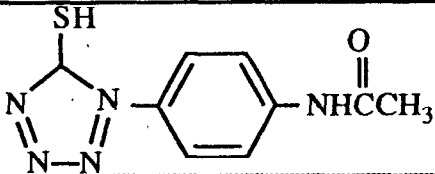
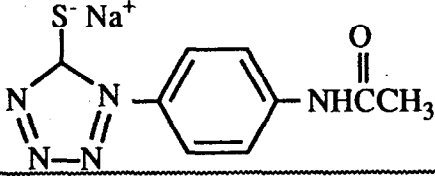
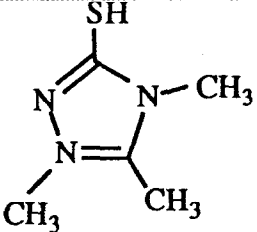
Compound	Structure	Sample name	Feature A' (eV)	Feature A (eV)	Feature B (eV)
ethylenethiourea		ETU	2472.0	2473.4	2475.1(sh) 2476.7
tetramethylthiourea		TMTU	2471.4	2473.2	2474.7(sh) 2476.0*
3-carboxymethyl-4-methyl-4-thiazoline-2-thione		CMMT	2471.3	2474.3*	2476.2
Mercaptotetrazoles and triazoles:					
2-ethylmercaptotetrazole		EMT	2472.5 (wk. sh)	2473.2*	2476.2
2-phenylmercaptotetrazole		PMT	2471.8	2473.6*	2476.3 (sh) 2478.2

Table 6.2. continued

Compound	Structure	Sample name	Feature A' (eV)	Feature A (eV)	Feature B (eV)
2-acetamidophenylmercapto-tetrazole		APMT	2471.8	2473.5*	2475.9 (sh) 2477.7
2-acetamidophenylmercapto-tetrazole sodium salt		APMTNA	2472.2 (wk. sh)	2473.2*	2476.7
2,3,4-trimethyl-2,4,5-tetrazole thiolate		TRZ	2472.4 (sh)	2473.2*	2474.9

*most intense feature.

Table 6.3. Energies of Transitions in Cl K-Edge Spectra of Dyes and Dye Intermediates.

Compound	Structure	Sample name	Feature A (*) (eV)	Feature B (eV)
5-chloro-1,3,3'-triethylbenzimidazothiacarbocyanine iodide		DC1	2825.0	2830.5
Anhydro-3-carboxymethyl-5,5'-dichloro-3'-ethylthiacyanine hydroxide		DC3	2825.0	2830.6
5,5'-dichloro-3,3'-2(2-hydroxyethoxy)ethyl-9-ethylthiacarbocyanine tetrafluoroborate		DC6	2825.1	2831.5

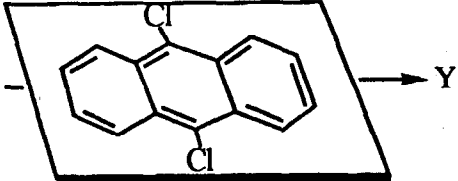
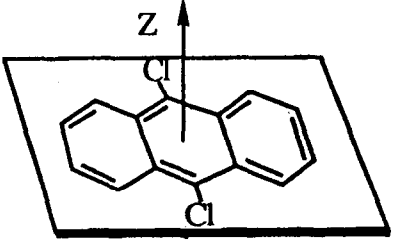
Table 6.3. continued

Compound	Structure	Sample name	Feature A (*) (eV)	Feature B (eV)
5-[(5,7-dichloro-3-ethyl-2-benzoxazol-2-ylidene)-ethylidene]-1,3-diethyl-2-thioarbituric acid		DM1	2825.0	2831.0
5-(5,6-dichloro-1,3-diethyl-2-benzimidazol-2-ylidene)-3-ethyl-1-phenyl-2-thiohydantoin		DM3	2824.8	2828.2 2831.4
4-[(5-chloro-3-ethyl-2-benzoxazol-2-ylidene)-ethylidene]-3-methyl-1-phenyl-2-thiohydantoin		DM4	2825.1	
2-[2,4-bis(1,1-dimethylpropyl)-phenoxy-N-(3,5-dichloro-2-hydroxy-(4-methyl)phenyl)-butanamide		ICL1	2825.2	2830.0 2831.9

Table 6.3. continued

Compound	Structure	Sample name	Feature A (*) (eV)	Feature B (eV)
2-[2,4-bis(1,1-dimethylpropyl)-phenoxy-N-(3,5-dichloro-2-hydroxy-(4-ethyl)phenyl)-butanamide		ICL2	2825.1	2829.3 2832.1
9,10-dichloroanthracene		DCA	2825.0	2830.5
9,10-dichloroanthracene in-plane, along Cl-Cl		DCAX1X	2825.0	2827.9 2831.3

Table 6.3. continued

Compound	Structure	Sample name	Feature A (*) (eV)	Feature B (eV)
9,10-dichloroanthracene in-plane, perp. to Cl-Cl		DC4X1Y	2825.0	2827.9 2829.4 2831.7*
9,10-dichloroanthracene out-of-plane		DC4X2Z	2824.6	2827.2 2830.4*

*most intense feature.

Table 6.4. Energies of Transitions in Silver- and Gold-Sulfur Complexes.

Compound	Sample name	Feature A (eV)	Feature B (eV)
silver (I) benzthiazole tetrafluoroborate	AGBENZ	2473.3*	2474.5
silver (I) 3-carboxymethyl-4-methyl-4-thiazoline-2-thione hydrate tetrafluoroborate	AGCMMT	2473.7 2471.8 (sh)	2476.1
silver (I) phenylmercaptotetrazole tetrafluoroborate	AGPMT	2473.3*	
silver (I) bis(trimethyltriazolium-thiolate) tetrafluoroborate, monomer	AGTRZ	2473.6* 2473.0 (sh)	2474.8
silver (I) bis(trimethyltriazolium-thiolate) tetrafluoroborate, polymer	AGTRZ2	2473.3*	
silver (I) tetris(trimethyltriazolium-thiolate) tetrafluoroborate, monomer	AGTRZ4	2473.2*	(sh at 2472.7 pk at 2473.6)
gold (I) bis(ethylenethiourea) chloride hydrate	AUETU2	2473.3*	2475.3
gold (I) bis(ethylenethiourea) chloride hydrate in-plane, along C-S	AUETU2X	2473.5	2475.3*
gold (I) bis(ethylenethiourea) chloride hydrate in-plane, along Au-S	AUETU2Y	2473.4*	2475.4
gold (I) bis(ethylenethiourea) chloride hydrate out-of-plane	AUETU2Z	2473.2*	2474.5 2475.6
gold (I) thiourea tetrafluoroborate	AUTHIOUR	2473.3*	2475.0
gold (I) tetramethylthiourea tetrafluoroborate	AUTMTU	2473.3* 2472.6 (sh)	2474.9
gold (I) bis(trimethyltriazolium thiolate) tetrafluoroborate	AUTRZ2	2473.5*	2475.1
silver (I) gold (I) bis(trimethyltriazolium thiolate) tetrafluoroborate	AGAUTRZ2	2473.6*	2475.4

Table 6.4. continued

Compound	Sample name	Feature A (eV)	Feature B (eV)
Metal Sulfides			
silver (I) sulfide	AG2S	2471.8	2474.1*
gold (I) sulfide	AU2S	2472.6*	
gold (III) sulfide	AU2S3	2472.3*	
(Ph4P)4[Au12S8]	AU12S8	2473.4*	2476.0

* most intense feature

Experiments were conducted under dedicated conditions on the unfocused 8-pole wiggler beamline 4-1 and the focused 54-pole wiggler beamline 6-2 (in low magnetic field mode) at Stanford Synchrotron Radiation Laboratory (3.0 GeV, 40 - 80 mA), and on unfocused bending magnet beamlines X19A and X10C at the National Synchrotron Light Source (2.5 GeV, 90 - 200 mA) by using Si (111) double crystal monochromators. Higher harmonics were rejected by detuning the monochromator 80% at 2740 eV for the sulfur edge and 60% at 3250 eV for the chlorine edge on beamline 4-1. On beamline 6-2, higher harmonics were rejected by placing 3-4 layers of Al foil between the sample holder and the detector and detuning the monochromator at 2740 eV for S and 3150 eV for Cl until the fluorescent signal approached dark current level, resulting in ~ 20% detuning. Incident radiation was detuned 20% - 30% at 2740 eV on beamlines X19A and X10C. Beam size for the powder samples was defined to be 2 mm x ~ 15 mm except on beamline 6-2 which was defined by the focusing mirror to be ~ 1.5 mm x 4.0 mm. For the single crystal samples, the incident beam size was defined to be slightly larger than the size of the crystal in the appropriate orientation. For the polarized surface measurements (performed on beamline 6-2 at SSRL), the width of the beam was determined by the size of the focusing optics. Slits were set to allow the maximum amount of sample to be illuminated by a narrow band of beam (7 x 1 mm for $\chi = 0^\circ$, 5 x 2 mm for $\chi = 90^\circ$).

Data were collected at room temperature in fluorescence mode using a N₂-filled gas ionization detector of the Stern/Heald/Lytle design.^{2,19} Powder samples were finely ground in a mortar and dusted onto Mylar tape to avoid self-absorption effects. At the low energies at which these experiments were conducted (~ 2460 eV to ~ 3200 eV), reduction in incident radiation intensity by air absorption is of major concern. To alleviate this problem, the experiment was conducted under a helium beam path for the incident radiation and sample fluorescence. Polypropylene windows of thickness 6.3 μm were used where necessary. Scans of Na₂S₂O₃·2H₂O collected between sample measurements were used to calibrate the energy of the sample spectra by assigning the position of the first peak in the thiosulfate scan at 2472.02 eV. For each sample, 2-5 calibrated scans were averaged and the inherent background in the data was removed by fitting a polynomial to the pre-edge region which was extrapolated through the entire spectrum and subtracted. The data were normalized to an edge jump of unity for direct comparisons of intensities of features. The positions of the edge features were determined by locating the position of the half-width at half-maximum of the second derivative in the region of the feature of interest, and are listed in Tables 6.1-6.4.

6.2.1. Single-Crystal Polarized Studies

For dipole-allowed transitions, the features seen in the K-edge spectra are governed by the following relation:

$$\sigma = |\langle \Psi_f | \mathbf{e} \cdot \mathbf{r} | \Psi_i \rangle|^2 \quad (1)$$

which can be approximated by:

$$\sigma = \cos^2 \theta |\langle \Psi_f | \mathbf{r} | \Psi_i \rangle|^2 \quad (2)$$

where σ is the photoabsorption cross section, Ψ_f is the final state wave function, Ψ_i is the initial state wave function (S or Cl 1s orbital), \mathbf{e} is the polarization vector of the incident radiation (perpendicular to the direction of the incident radiation and in the plane of the synchrotron ring), \mathbf{r} is the transition dipole operator (x , y , or z) and θ is the angle between \mathbf{e} and \mathbf{r} . The dipole-allowed transition from an initial 1s state is to a final p state ($\Delta l = \pm 1$), and the maximum in the photoabsorption cross section is obtained when $\theta = 0^\circ$, when the polarization vector and the dipole operator are parallel. By aligning a molecular orientation in the sample (for example, a C-S bond) with the direction of the incident radiation polarization vector, one can selectively excite transitions into the orbitals along that molecular orientation. The symmetry of the transitions ($p\sigma$ or $p\pi$) seen in the anisotropic powder spectrum can be therefore be determined by observing the polarization properties of the various transitions as a function of molecular alignment.

Single crystal samples were mounted on a glass fiber using polymethylmethacrylate in methylene chloride as the adhesive for the S-containing crystals, and a standard 5 minute epoxy (which contains S) for the Cl-containing crystals, and attached on a standard goniometer head. On the beamline, a lid to the sample chamber containing a goniometer mount was used allowing full rotation in phi with chi fixed at 180° . The samples were preoriented on a Syntex P2₁ 4-circle diffractometer in such a way that the molecular orientation of interest could be isolated solely by rotations in phi. This geometric restriction meant that more than one crystal was required to isolate all of the orientations of interest. For 2-thiohydantoin and 9,10-dichloroanthracene, two crystals were used to isolate three orientations. For bis(ethylenethiourea) Au (I) and 3,3'-diethylthiacyanine bromide, one crystal per orientation was required, for a total of three crystals for AUETU2, and two crystals for DC5. The largest source of error in these polarized measurements is due to

misalignment of the samples in the beam, however we estimate that the maximum misalignment of the goniometer mount on the beamline is 2°, resulting in less than a 5% loss of polarization. After the data at the proper phi setting were measured, the crystal was misaligned 2-5° to insure that the features noted were not due to Bragg diffraction peaks from the crystal lattice planes.

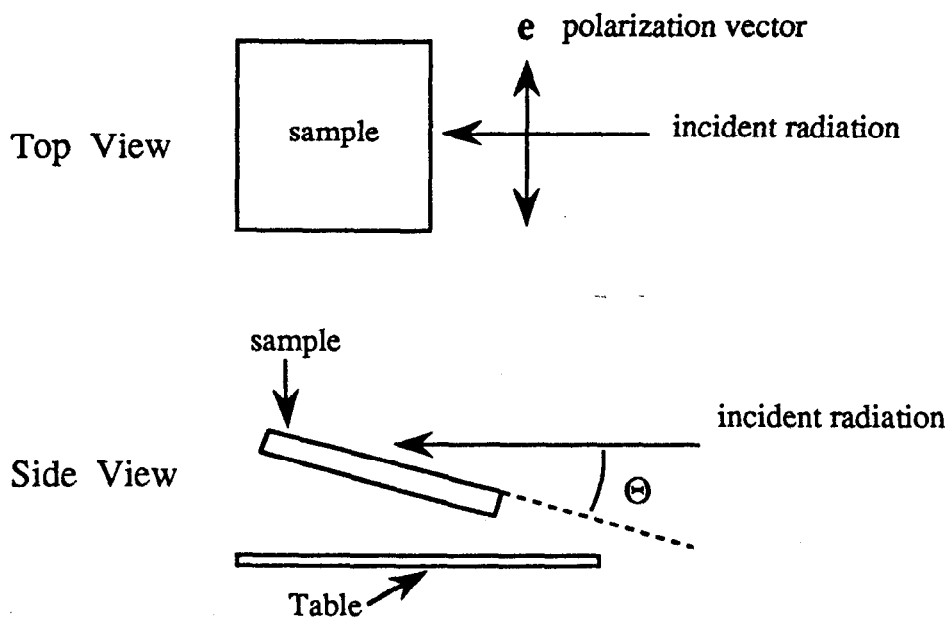
6.2.2. Polarized Surface Measurements

Surface X-ray measurements at glancing angle configurations take advantage of the fact that X-rays undergo total external reflection below the critical angle, Θ_c , and therefore penetrate only 20 - 30 Å into the surface.²⁰ At angles less than the critical angle, the signal of an adsorbed species on the surface of a substrate is enhanced relative to that of the substrate due to the decreasing penetration depth of the incident radiation. The critical angle is dependent on the type of substrate the X-rays reflect from and is governed by the following equation for Θ_c in radians:²¹

$$\Theta_c = \lambda \left(5.4 \times 10^{10} \frac{Z\rho}{A} \right)^{1/2} \quad (3)$$

where λ is the wavelength of radiation (cm), and Z is the atomic number, ρ the density and A the atomic weight of the substrate. For a AgBr substrate, the critical angle (in degrees) ranges from 1.13 at the S K-edge (2470 eV), to 1.02 at the end of a typical sulfur scan (2740 eV), and from 0.987 at the Cl K-edge (2820 eV) to 0.883 at the end of a chlorine scan (3150 eV). The measurements reported for this work were done at angles of 1°, which was sufficient at all energies to obtain an acceptable signal-to-noise level. There has been a study of low-Z adsorbates on high-Z substrates using fluorescence detection in which the authors found that a glancing angle configuration was not required for the characterization of the surface species.²² This will be tested on this system as well. The surface samples were mounted on a sample plate attached to a rotation stage, thereby allowing full phi rotations to be made (in the azimuthal plane). The sample plate and rotation stage were placed on a 90° chi circle mounted perpendicular to the beam to allow both in-plane and out-of-plane orientations to be collected at grazing incidence angles (Figure 6.1).

a



b

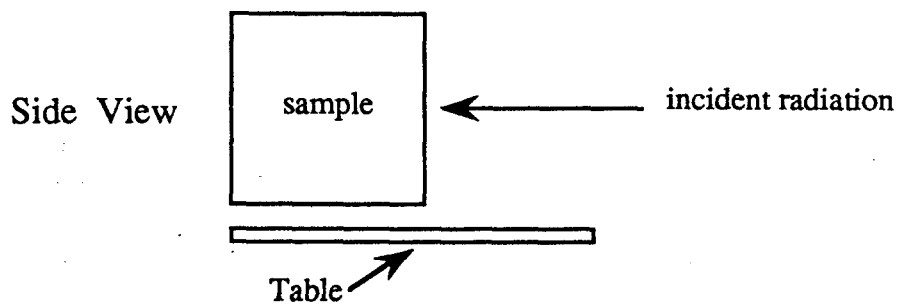


Figure 6.1. Schematic of the geometry utilized for the surface measurements. χ refers to the orientation of the surface relative to the table and Θ refers to the angle of the surface relative to the incident radiation. (a) $\chi = 0^\circ$ orientation. (b) $\chi = 90^\circ$ orientation.

6.3. Results

6.3.1. S K-Edge Spectra of Dye Molecules

6.3.1.1. Cyanine Dye Molecules. Cyanine spectral sensitizing dyes contain cyclic sulfur in 5-membered rings such as thiazole, benzthiazole and naphththiazole with various ring substituents and bridges between the dye nuclei (Table 6.1). The sulfur spectra of cyanine molecules consists of two features (Figure 6.2), a high-intensity feature at 2473.3 - 2474.1 eV (Feature A) and a lower-intensity transition at 2475.2 - 2476.4 eV (Feature B). The relative intensities of these features and the shape of the multiple scattering regime (above ~ 2478 eV) reflects changes in the local environment of the S atom. The energy of Features A and B are relatively invariant, however the features appear at a slightly higher energy for cyanine-type molecules which contain aromatic groups, such as the benzthiazole (IC2, DC1, DC2, DC3, DC5, DC6) and naphththiazole (IC3) derivatives (Feature A at 2473.8 - 2474.0 eV; Feature B at 2475.8 - 2476.4 eV) relative to the non-aromatic thiazole compounds (IC1, DC4: Feature A at 2473.3 - 2473.5 eV; Feature B at 2475.2 - 2475.3 eV). This suggests that the presence of the electron-withdrawing aromatic groups results in an effective positive charge on the sulfur atom relative to the non-aromatic group-containing dyes and dye intermediates.

Single-crystal polarized spectra of the benzthiazole-containing dye molecule 3,3'-diethylthiacyanine bromide are presented in Figure 6.3. Spectra were obtained for two polarizations, one corresponding to polarization in the plane defined by the benzthiazole group (DC5X), and the other corresponding to polarization along the average normal to that plane (DC5Z). The molecule is not completely planar, with a dihedral angle of $\sim 13^\circ$ between the thiazoline rings, therefore the polarizations of this molecule could not be completely isolated. In the powder spectrum, the most intense feature occurs at 2473.8 eV, and Feature B appears at 2475.6 with a shoulder at 2476.4 eV. In the in-plane polarized spectrum, the white-line feature occurs at 2473.5 eV, and in the out-of-plane polarized spectrum at 2473.9 eV. The shoulder at around 2475.6 eV is also present in both polarized spectra, however it occurs as a single feature in the in-plane polarized spectrum at 2475.1 eV, and as a doublet in the out-of-plane spectrum at 2475.6 and 2476.5 eV. The white-line feature is somewhat more intense in the in-plane polarized spectrum than in the out-of-plane spectrum, suggesting that the contribution to the S K-edge absorption features of 3,3'-diethylthiacyanine bromide, and by extension to the other molecules with S heterocyclic groups, involves transitions to final states with $p\sigma$ type symmetry. The presence of the 2473.9 eV feature in the out-of-plane spectrum might be due to the inability to completely

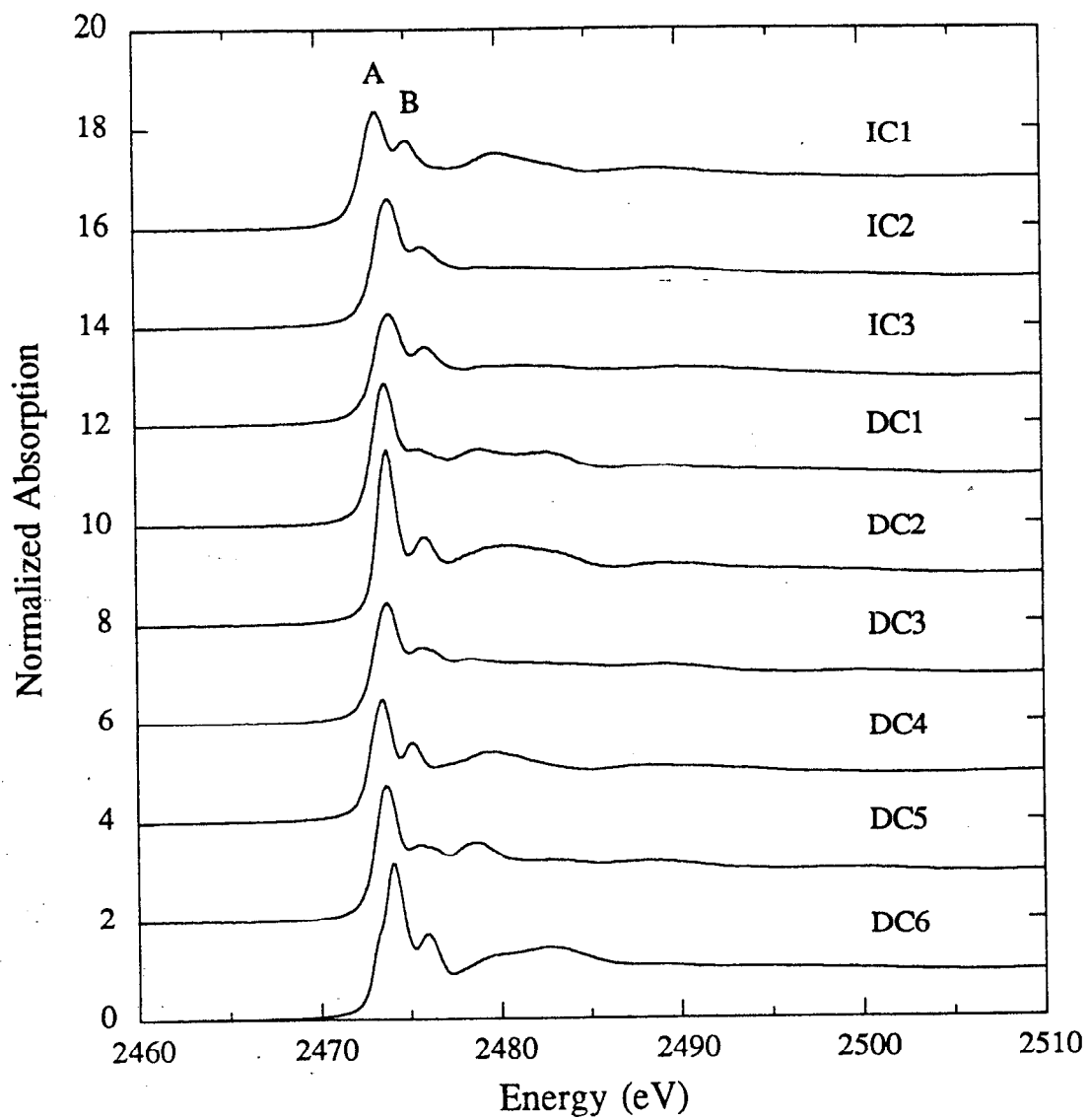


Figure 6.2. The S K-edge spectra of cyanine dyes and dye intermediates (Table 6.1).

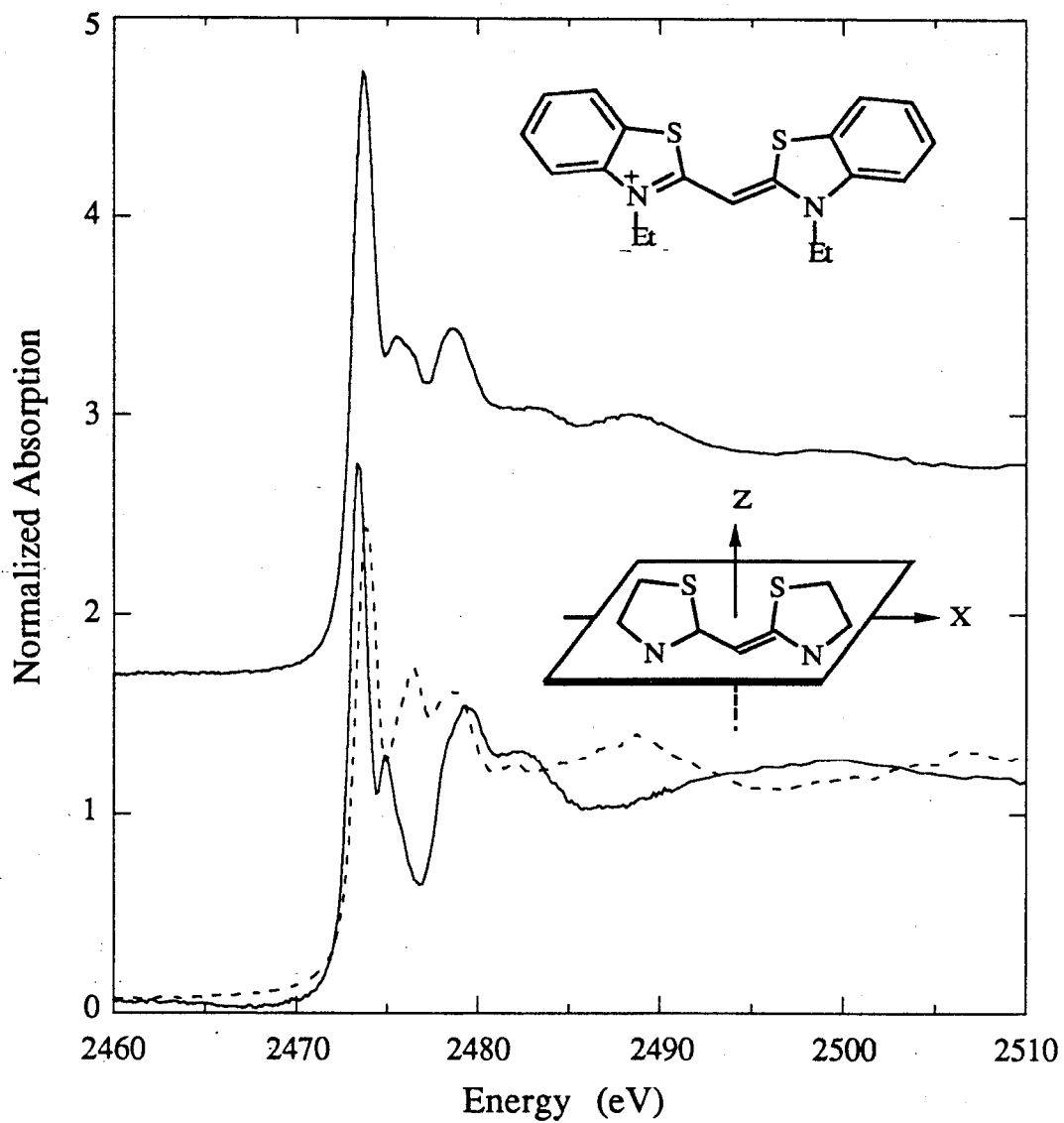


Figure 6.3. The powder spectrum (top) of DC5, a cyanine dye molecule, compared with the single-crystal spectra (bottom) corresponding to polarization along the average X (solid) and Z (dash) molecular axes.

isolate the out-of-plane orientation from the in-plane orientation due to the packing of the molecules in the crystal structure of this compound, or it could reflect a transition to an orbital oriented along the normal to the benzthiazole plane (discussed below).

These studies on the cyanine dye molecules are consistent with the results of the soft X-ray studies and calculations done for a variety of S heterocycles, thiols and thioethers.^{6,7} In these studies, the dominant feature in the S K-edge spectra occurs between 2472.3 and 2473.4 eV (relative to the t_{1u} resonance of SF₆ at 2486 eV), similar to the location of the strongest feature in the cyanine dyes and dye intermediaries. This feature has been assigned to a transition to a S-C final state with σ^* symmetry,^{2,6,7} which supports the qualitative determination of the symmetry of this feature based on our polarized single-crystal study. One explanation for the 2473.9 eV feature in the Z, or out-of-plane orientation of 3,3'-diethylthiacyanine bromide is that there is a final state orbital with π character that accounts for some of the intensity of the primary feature in the powder spectrum. In a study of the aromatic molecule thiophene,^{6a} MS-X α calculations show that the lowest unoccupied valence orbital has π^* symmetry and occurs at approximately the same energy as the S-C σ^* orbital. The aromatic character of thiophene allows appreciable delocalization of the π^* level onto the sulfur atom, accounting for approximately 25% of the intensity of the 2473 eV feature, with the balance being accounted for by the transition to the S-C σ^* orbital. It is therefore likely that there is a contribution to the white-line feature from a transition to a final state with $p\pi$ symmetry due to the extended conjugated system of 3,3'-diethylthiacyanine bromide, and that the presence of the 2473.9 eV feature in the out-of-plane polarized spectrum is not due solely to the crystallographic limitations on isolating the out-of-plane orientation from the in-plane orientation.

6.3.1.2. Merocyanine Dye Molecules. Merocyanine spectral sensitizing dyes contain sulfur as a terminal thione group on 5- or 6-membered heterocyclic rings such as thiohydantoin, benzoxazole, benzimidazole, or thiobarbituric acid (Table 6.2). Like cyanine dyes, the merocyanine dye spectra have a feature between 2473.4 and 2474.0 eV (Feature A), which has been attributed to a transition to a final state with $p\sigma$ symmetry (Figure 6.4). However, this feature is less intense relative to the edge jump in the merocyanine dye spectra than in the cyanine dye spectra (see Figure 6.6a). The shoulder on the high energy side of Feature A in the cyanine dye spectra is absent in the merocyanine dye spectra, however a broad feature which in some cases has a low energy shoulder, is seen in all of the merocyanine dye spectra (2475.4 - 2478.2 eV, Feature B). The most striking difference between the merocyanine and cyanine dye spectra occurs to the low energy side of Feature A. The merocyanine dye spectra are characterized by a sharp feature

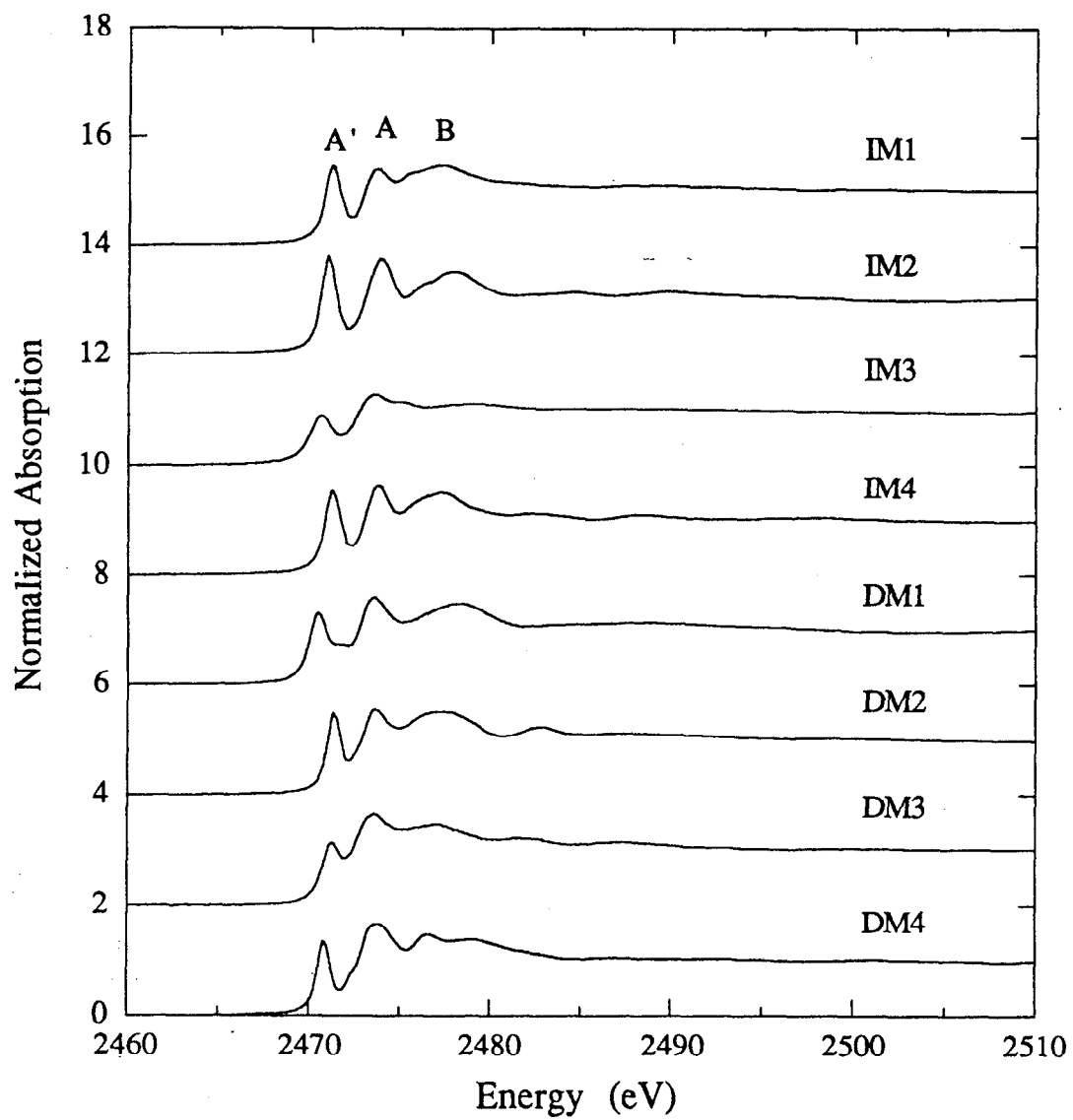


Figure 6.4. The S K-edge spectra of merocyanine dyes and dye intermediates (Table 6.2).

(Feature A') at 2470.5 - 2472.5 eV, which is unique to the presence of the terminal thione group.

The single-crystal polarized spectra for 2-thiohydantoin, a merocyanine dye intermediate, are presented in Figure 6.5. Three orientations were isolated, corresponding to polarization in the plane of the ring and along the C=S bond (X polarization), in the plane and perpendicular to the C=S bond (Y polarization), and perpendicular to the plane and the C=S bond (Z polarization). The Z orientation is 100% polarized normal to the plane of the 2-thiohydantoin molecule, while the X and Y orientations are each 70% polarized. The spectra reveal that the features in the powder spectrum have different polarization properties. The sharp pre-edge feature at 2471.2 eV, characteristic of the thione sulfur, is polarized almost entirely along the normal to the plane of the 2-thiohydantoin molecule, while the white-line feature at 2473.7 eV is polarized in the plane of the molecule, predominantly along the C=S bond. This is consistent with the results of the single-crystal polarized study of the cyanine dye molecule, in which the ~ 2474 eV white-line feature corresponds to a transition to a final state with $p\sigma$ symmetry. The sharp pre-edge feature, on the other hand, can be accounted for by a transition to a state with $p\pi$ symmetry due to the presence of unfilled $p\pi^*$ orbitals for molecules of this type.

The compounds 3-ethylrhodanine and 3-carboxymethyl-1,4-methyl-4-thiazoline-2-thione contain sulfur in both a heterocyclic and exocyclic form (IM3 and CMMT, respectively, Table 6.2). The spectra are a superposition of the features characteristic of both the thione and thiazole S, with a pre-edge feature characteristic of the thione S and a white-line intensity similar to that of the cyclic sulfur cyanine dyes (Figure 6.6).

In addition to the merocyanine dye and dye intermediates discussed above, spectra were collected on a variety of thioureas, mercaptotetrazoles and mercaptotriazoles (Figure 6.7). In the thioureas, the sulfur is present as a thione, similar to the merocyanine dyes, while the mercaptotetrazoles and triazoles contain sulfur as a thiol (Table 6.2). Although Feature A' is present in all of the spectra, its position and resolution from Feature A is sample dependent. In the thione-containing compounds, the feature occurs between 2470.5 and 2472.0 eV. Upon protonation of the thione sulfur to a thiol group, the position of the feature shifts to higher energy and occurs at 2471.8 eV for the phenyl-substituted mercaptotetrazoles (PMT and APMT) and at 2472.5 eV for ethylmercaptotetrazole and trimethyltriazolium thiolate (EMT and TRZ). Upon deprotonation of the thiolate in the sodium salt of 2-acetamidophenylmercaptotetrazole (APMTNA), the pre-edge feature appears as a poorly resolved shoulder on the rising edge at 2472.4 eV (Figure 6.8).

There have been a few S K-edge studies of compounds containing a terminal sulfur group.^{6b-c,7} Both CS₂ and SCO have features below 2473 eV (at 2470.8 for CS₂ and

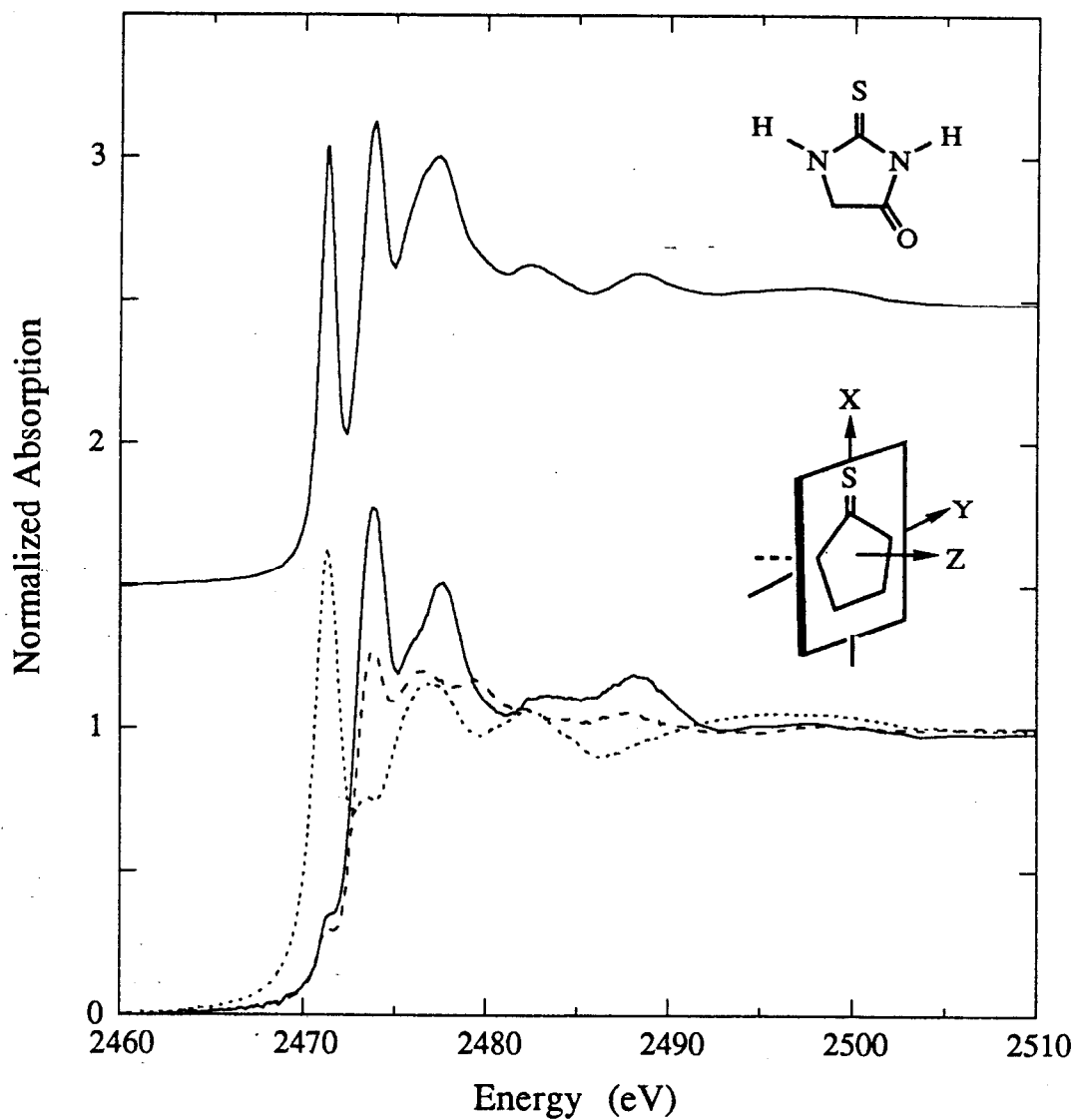


Figure 6.5. The powder spectrum (top) of IM4, a merocyanine dye intermediate, compared with the single-crystal spectra (bottom) corresponding to polarization along the average X (solid), Y (dash), and Z (dot) molecular axes.

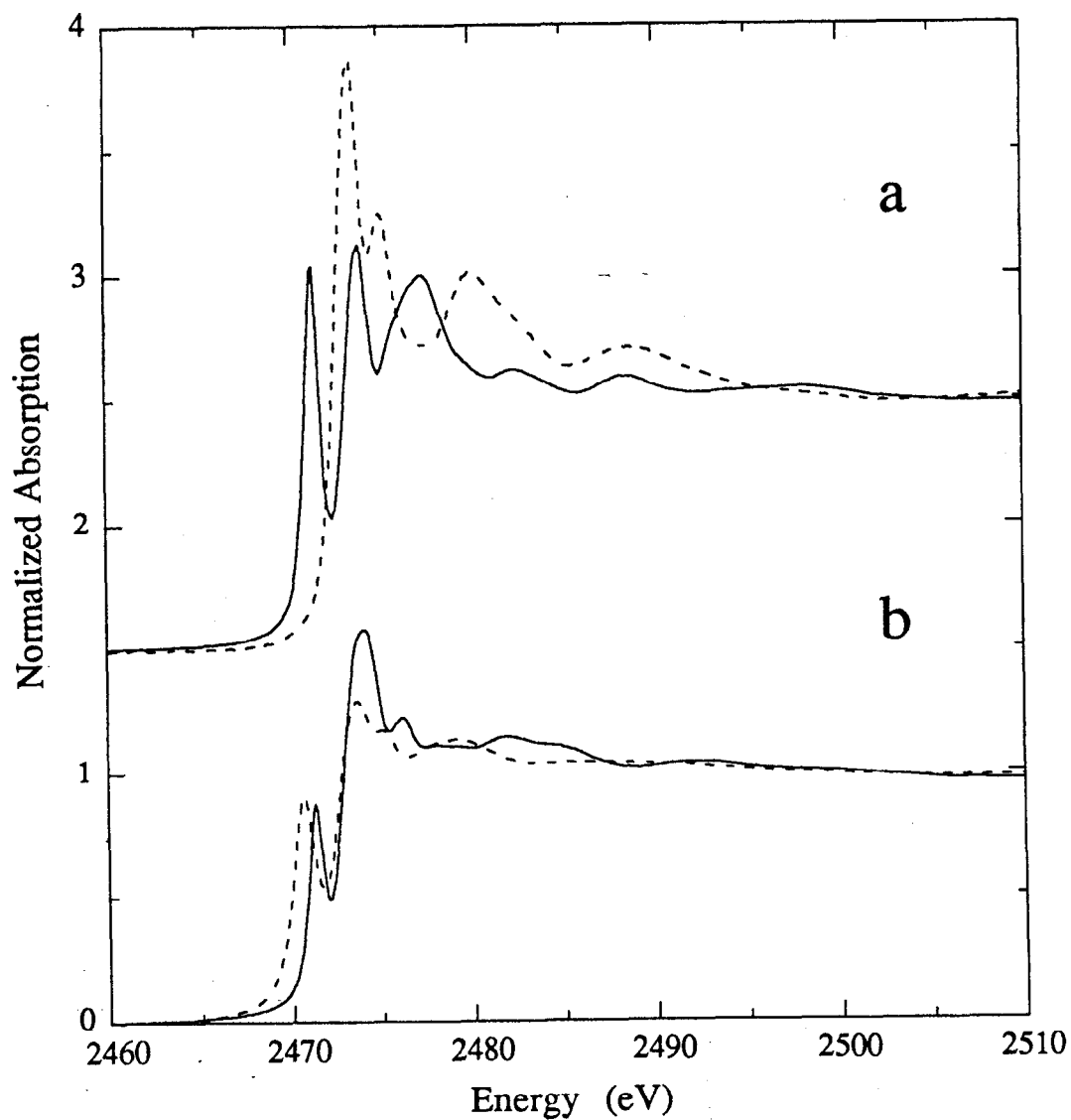


Figure 6.6. The spectra (a) of IM4 (solid), a merocyanine dye intermediate, and IC1 (dash), a cyanine dye intermediate compared to the spectra (b) of CMMT (solid) and IM3 (dash) which contain S both in a cyclic and exocyclic form.

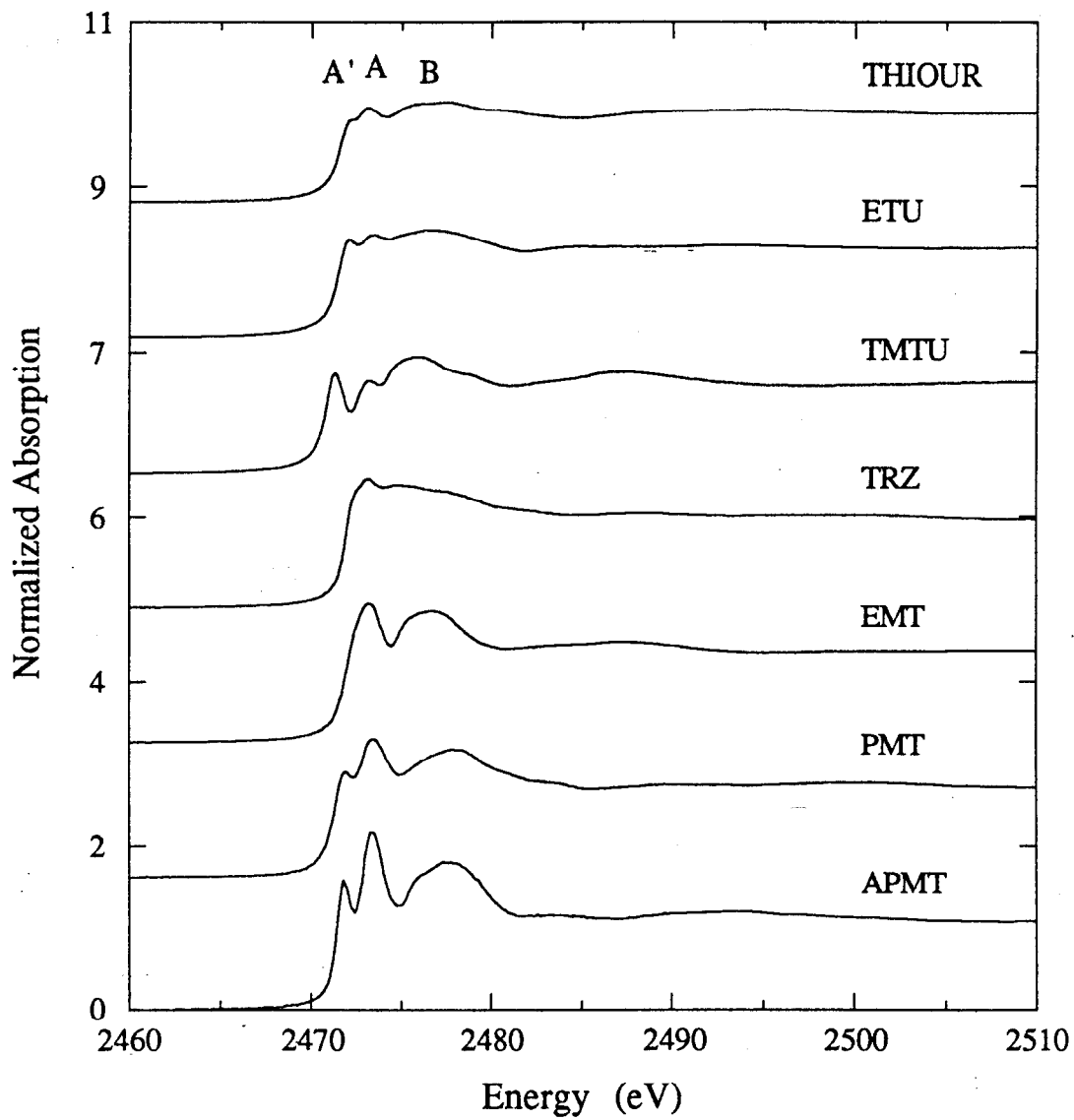


Figure 6.7. The S K-edge spectra of thioureas, mercaptotetrazoles and mercaptotriazoles (Table 6.2).

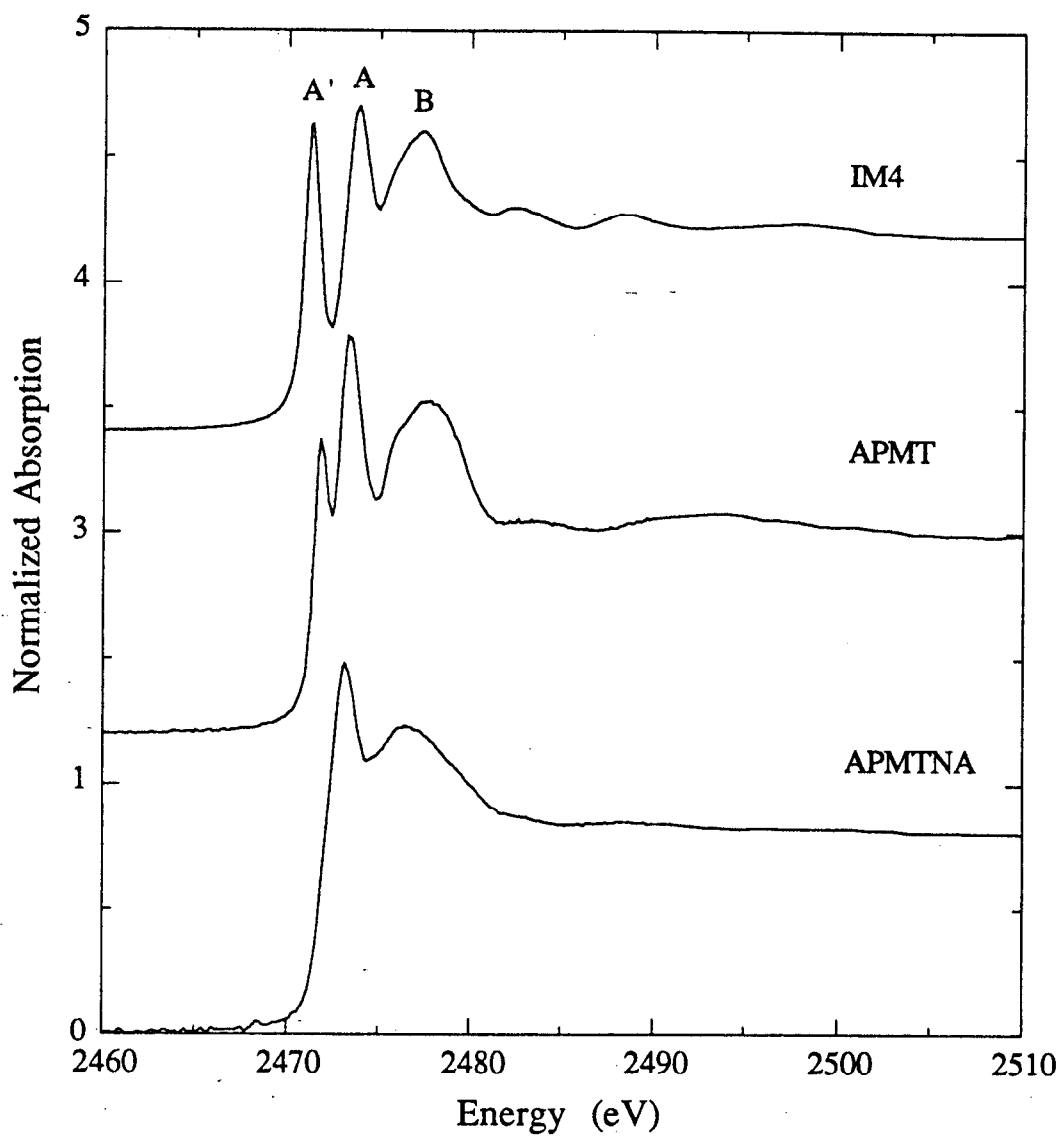


Figure 6.8. The position of the thione-feature is compared for S present as a thione (top, IM4), a thiol (middle, APMT), and a thiolate (bottom, APMTNA). See Table 6.2 for the structures.

2472.0 for SCO), which have been assigned to transitions with final states of π symmetry, consistent with the qualitative results of the polarized single-crystal measurements on 2-thiohydantoin reported herein. In contrast to the thiols studied here, there is no low energy pre-edge feature seen in the S K-edge spectra of the alkyl thiols studied by Dezarnaud et. al.^{6b} The primary difference between the alkyl thiols and the thiols studied in this work is the presence of the conjugated system in the mercaptotetrazoles and -triazoles. The low energy feature may thus reflect the involvement of the terminal S group in some sort of a π system, whether it be a double bond to C as in the merocyanine dye molecules and the thioureas, or the presence of a conjugated π system such as in the mercaptotetrazoles and -triazoles. The factors involved in determining the relative intensities and the energies of the terminal sulfur low energy feature studied in this work have not yet been established. Qualitatively, the position of this feature moves to higher energy from thione to thiol to thiolate (Figure 6.8), suggesting that the position of the low energy feature is related at least in part to the accumulation of negative charge on the terminal sulfur.

6.3.2. Cl K-Edge Spectra of Dye Molecules

Chlorine is present as a substituent on both merocyanine and cyanine dye molecules (Table 6.3) and enhances the aggregation of the dye molecules resulting in the desired spectral shift to longer wavelengths. The Cl spectra are similar in all cases (Figure 6.9), with a white line transition between 2824.8 and 2825.1 eV, and a broad feature occurring between 2829.1 and 2830.6 eV.

To understand the polarization properties of Cl as a substituent on dye molecules, single-crystal polarized studies on 9,10-dichloroanthracene (DCA) were performed. The powder spectrum of DCA has the same spectral features as the Cl K-edge spectra of the dye and dye intermediate samples, making it an appropriate choice for the single crystal studies. The polarized spectra are presented along with the powder spectrum in Figure 6.10. The three spectra correspond to having the polarization vector in the plane of the molecule and along the Cl-Cl vector (X orientation), in the plane of the molecule and perpendicular to the Cl-Cl vector (Y orientation), and perpendicular to the plane of the molecule (Z orientation). The features in the powder spectra are present in all three of the polarized spectra, however the X orientation shows the highest intensity of the three spectra. In the Z polarized spectrum, the white-line feature is shifted to slightly lower energy, to 2824.6 eV and is a much narrower transition than for the in-plane oriented spectra, indicating that there may be multiple transitions occurring in the in-plane orientation. These results suggest that the white-line feature of compounds containing Cl in this kind of an environment is primarily

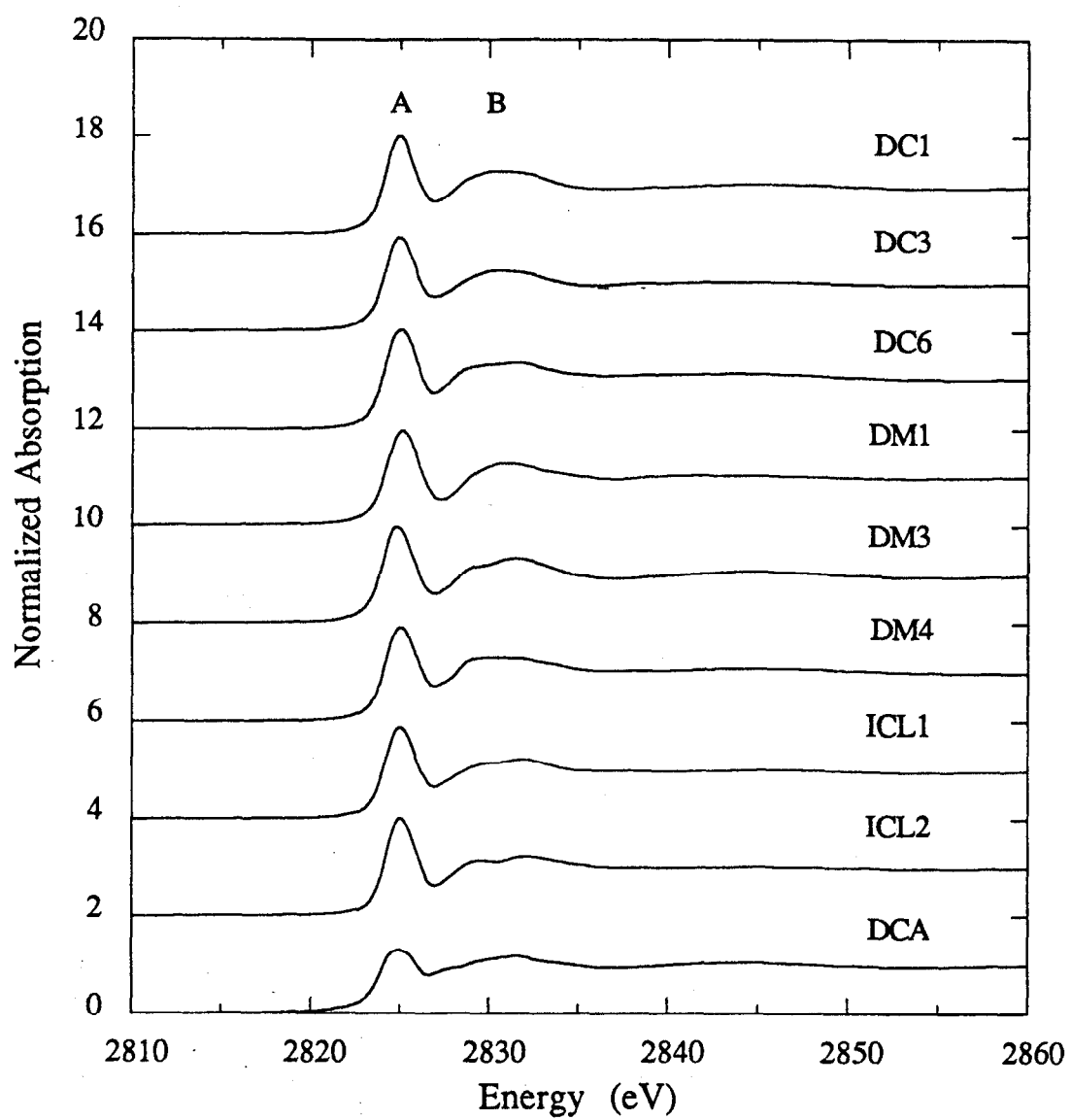


Figure 6.9. The Cl K-edge spectra of dyes and dye-intermediates (Table 6.3).

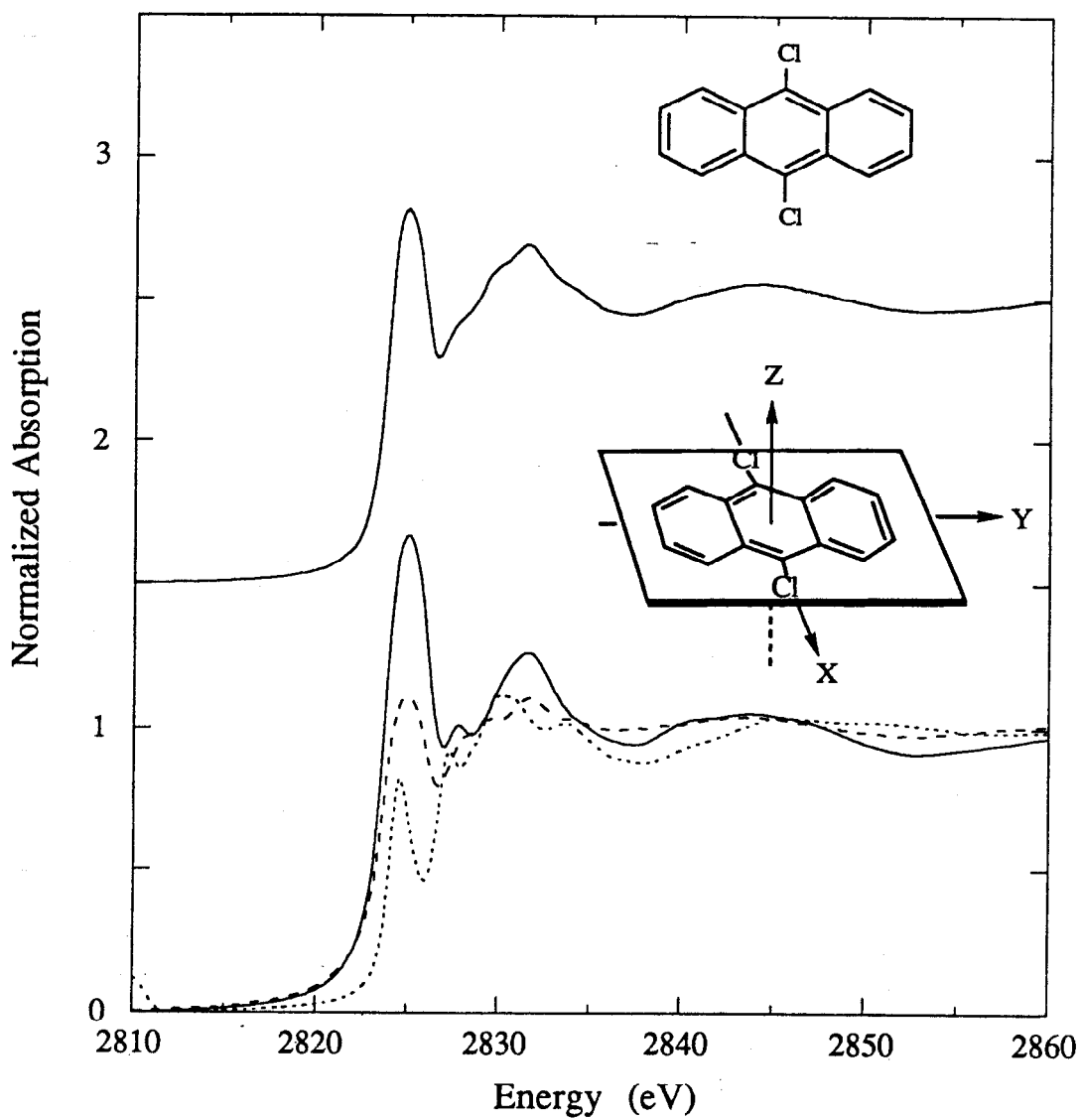


Figure 6.10. The Cl K-edge powder spectrum (top) of DCA, compared with the single-crystal spectra (bottom) corresponding to polarization along the average X (solid), Y (dash), and Z (dot) molecular axes.

due to a transition to a final state orbital with σ symmetry. The presence of the feature in the out-of-plane polarized spectrum could be due to a transition to a π symmetry orbital due to the aromatic nature of 9,10-dichloroanthracene, similar to the case of thiophene.^{6a}

There have been no other studies of Cl present as it is in the dye systems studied here, however Cl K-edge spectra have been reported for SCl_2 , S_2Cl_2 , SOCl_2 , and SO_2Cl_2 .^{6d-e} For these compounds, the Cl K-edge spectra is similar to the Cl K-edge spectra of the dye molecules studied here, with the most intense feature occurring between 2821.4 and 2822.5 eV. This feature has been assigned as a transition to a final state with S-Cl σ^* symmetry, supporting the qualitative conclusion that the white line feature in the Cl K-edge of the dye molecules can be attributed to a transition to a final state with σ symmetry.

6.3.3. Au and Ag Complexes with Sulfur-Containing Ligands

S K-edge XAS measurements were done on a wide variety of complexes formed between Ag or Au and S present as a thione group (3-carboxymethyl-4-methyl-4-thiazoline-2-thione, thiourea, ethylenethiourea and trimethylthiourea), a thiol group (phenylmercaptotetrazole, trimethyl-1,2,4-triazolium thiolate) or S present in a ring (benzthiazole), as well as on a variety of metal sulfides (Table 6.4). These compounds were chosen to investigate the effect that Ag or Au metal complexation would have on the electronic structure of photographic dyes, and to investigate the nature of the chemical sensitization centers. A comparison of representative ligand and metal-ligand complexes is presented in Figure 6.11. In all of the metal-sulfur compounds, the 2473 - 2474 eV white-line feature changes as a result of metal complexation and a shoulder to the high-energy side of the white-line feature appears at ~ 2475 eV. For the complex between Ag and a benzthiazole group (AGBENZ), the white-line feature broadens and decreases in intensity (Figure 6.11a). In complexes between Ag and terminal sulfur-containing ligands, such as AGCMMT (Figure 6.11b), AGPMT (Figure 6.11c), AGTRZ (Figure 6.11d), AGTRZ2 and AGTRZ4 (Figure 6.11e), the white-line feature increases in intensity and the pre-edge feature between 2470.5 and 2472.0 eV is absent. The pre-edge feature has been attributed to a transition to a $p\pi^*$ orbital by our single-crystal polarized studies; its absence in the metal complexes suggests that the $p\pi^*$ orbital of S is directly involved in the covalent metal-sulfur interaction.

The presence of gold has a much stronger effect on the S K-edge spectra than silver (Figure 6.12). In general, the intensity of the white-line feature of the Au complexes studied here (AUTMTU, AUETU2, AUTHIO, AUTRZ2, Figure 6.12a-d, respectively) is

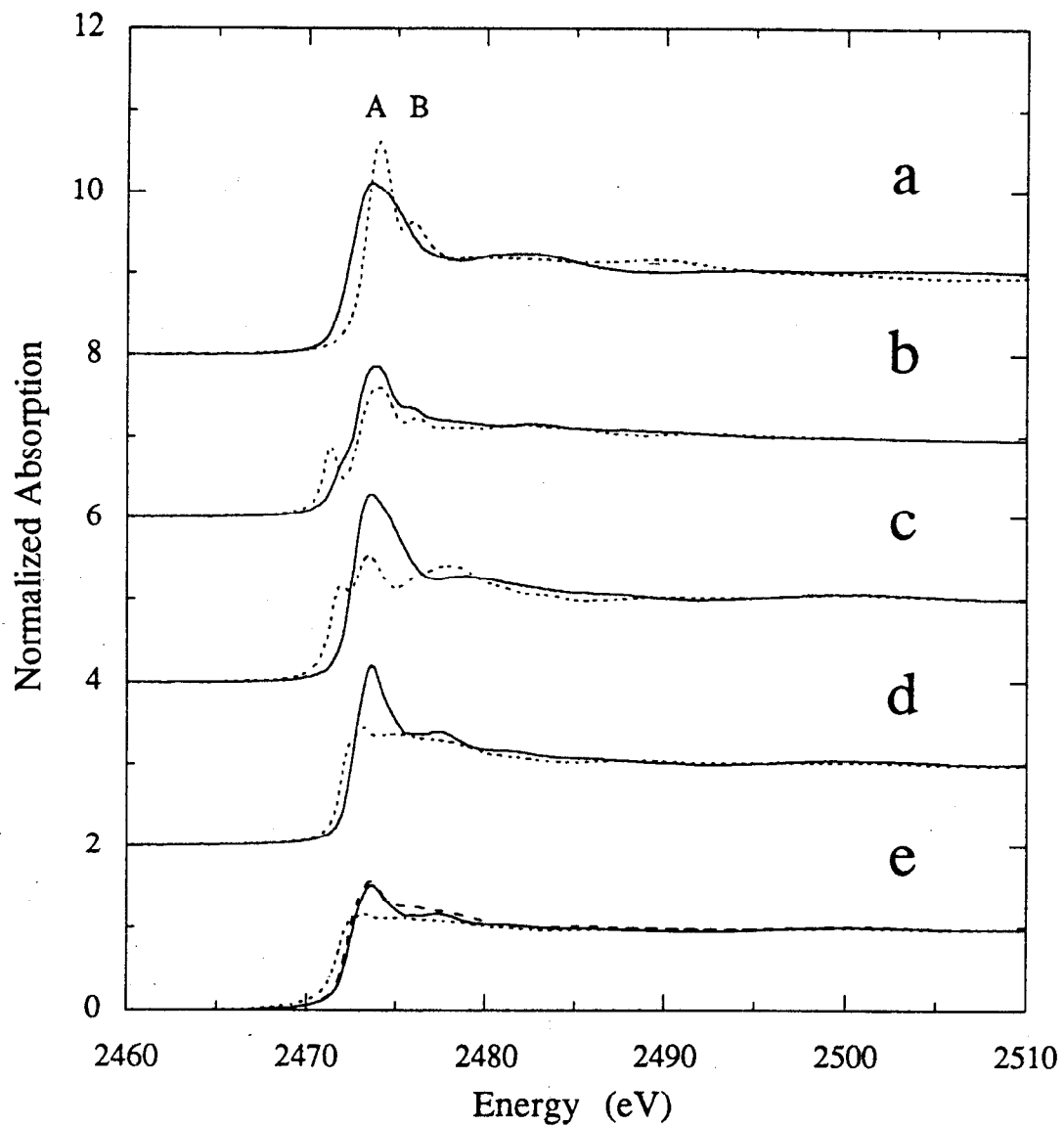


Figure 6.11. The spectra of Ag-S complexes. The solid lines are the spectra of the metal complexes and the dotted lines are the spectra of the ligands. (a) AGBENZ and BENZ, (b) AGCMMT and CMMT, (c) AGPMT and PMT, (D) AGTRZ and TRZ, (e) AGTRZ2, AGTRZ4 (dash) and TRZ.

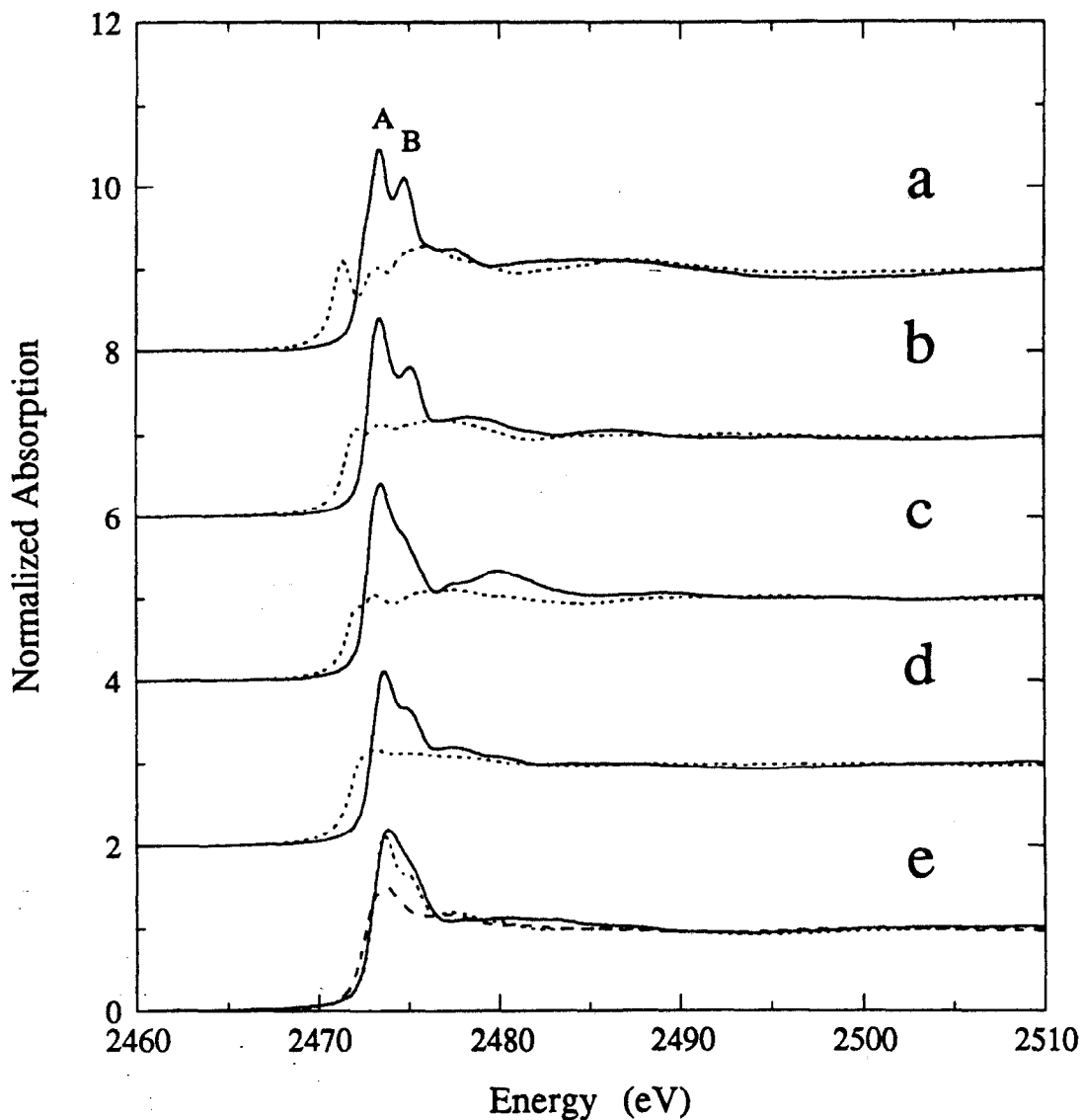


Figure 6.12. The spectra of Au-S complexes. The solid lines are the spectra of the metal complexes and the dotted lines are the spectra of the ligands. (a) AUTMTU and TMTU, (b) AUETU2 and ETU, (c) AUTHIO and THIOUR, (d) AURZ2 and TRZ. In (e), the spectra of a mixed metal complex (AUAGTRZ, solid) is compared to the spectra of a Au (AURZ2, dot) and Ag (AGTRZ2, dash) complex with the same ligand.

greater than that of the Ag complexes. The white-line transition in the Au complexes is also more narrow than in the Ag complexes and a shoulder can be seen on the high energy side of the main transition which is sometimes well-resolved. In the Ag complexes, the main transition is broadened to the high energy side, however no shoulder is resolved from this feature. In a comparison of Ag vs. Au complexation with the same ligand (AUTRZ2 and AGTRZ2, Figure 6.12e), the Au-containing complex has a much more intense white-line feature than the analogous Ag complex, and in the mixed metal AGAUTRZ compound, the spectrum is more similar to that of AUTRZ2 than AGTRZ2 (Figure 6.12e).

Data were collected on a series on Ag, Au and mixed metal sulfides (AG2S, AU12S8, AU2S, AU2S3) as models of the chemical sensitization centers. AU2S and AU2S3 are indistinguishable from each other, but the larger cluster, AU12S8, has a narrower white-line with a second transition to higher energy (Figure 6.13). The position of the white-line occurs at a higher energy than the white-line position of the smaller clusters as well. Silver sulfide is different from all of the gold sulfides (Figure 6.13), with a split, less intense and broader white-line. Although the S K-edge spectra do not provide enough information to determine the size of the metal sulfide clusters formed on the photographic substrate, it may be possible to decipher between Au and Ag sulfide clusters based on the shape and intensity of the white-line feature.

Single-crystal polarized S K-edge measurements were done on bis(ethylenethiourea) Au(I) hydrate hydrochloride (AUETU2), in which the Au metal forms a complex with the thione S. The powder spectra of AUETU2 and ethylenethiourea are compared in Figure 6.12b. For the powder spectrum of AUETU2, the low energy feature attributable to the thione S seen in the ligand spectrum is absent, and the spectrum contains an intense feature at 2473.3 eV and a lower-intensity feature at 2475.3 eV. For the polarized measurements, X was defined to be in the plane of the ligand rings along the average C-S_{thione} bond, Z was defined to be the average of the ligand plane normals, and Y, defined to be the cross-product of X and Z, is directed roughly along the S-Au-S bond. As a result of this definition, the Y orientation will contain some X character.

The polarized spectra reveal that the features in the powder spectra of AUETU2 are polarized primarily in the plane of the ligand rings (Figure 6.14). In the Y-oriented spectrum, the sharp white-line feature occurs at the same energy as in the powder spectrum, but in the X-oriented spectrum, the feature is broad and occurs at 2473.9 eV. This suggests that the white-line feature of the powder spectra of AUETU2 can be attributed to transitions to two final states, one with Au-S σ^* character (2473.3 eV), and one with C-S σ^* character (2473.9 eV). The shoulder at 2475.3 eV is the dominant feature in the X-polarized spectrum and it can therefore be concluded that this feature is due to a

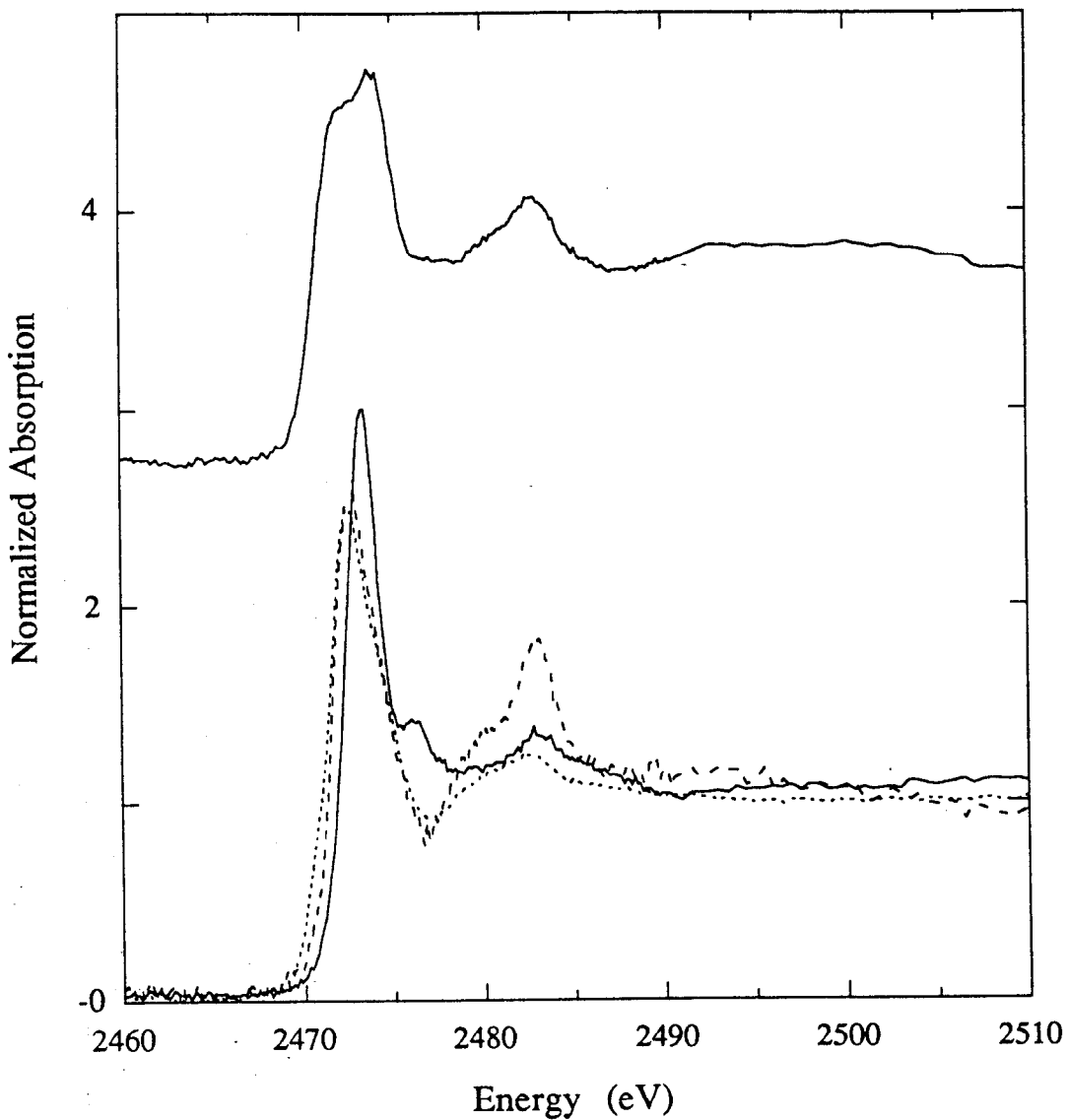


Figure 6.13. The S K-edge spectra for Ag and Au sulfides. (a) the powder spectrum of Ag_2S , (b) the powder spectra of Au_{12}S_8 (solid), Au_2S (dash) and Au_2S_3 (dot).

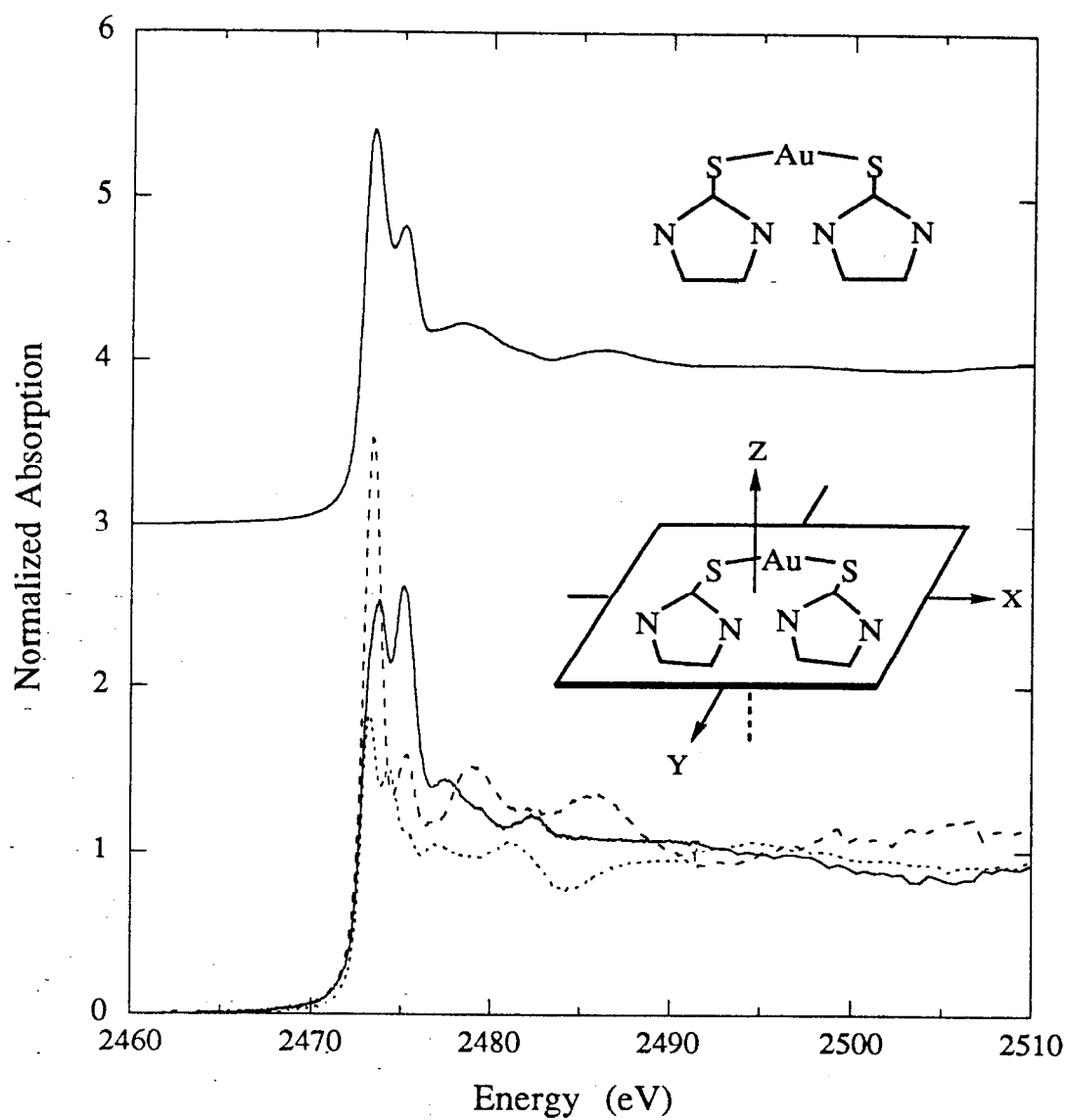


Figure 6.14. The powder spectrum (top) of AUETU2 compared with the single-crystal spectra (bottom) corresponding to polarization along the average X (solid), Y (dash), and Z (dot) molecular axes.

transition to a C-S σ -type orbital. In the Z-polarized (out-of-plane) spectrum, there is a feature at 2473.2 eV, whereas in the out-of-plane orientation of 2-thiohydantoin, no transition occurs at this energy (see Figure 6.5). The presence of the 2473.2 eV feature in the out-of-plane spectrum of bis(ethylenethiourea) Au(I) must therefore be due to the metal-sulfur interaction, and either reflects a transition to a final Au-S state with $p\pi^*$ symmetry which occurs at energies similar to those of the metal- and C-S σ -type final states, or represents a shift in the energy of the C-S $p\pi^*$ final state as a result of the interaction of the metal and sulfur atoms.

Extending these results to the other metal-sulfur complexes, it can be concluded that the intense feature at 2473 eV is due to transitions to two final states of σ symmetry, one with metal-S σ character, and the other with C-S σ character, while the shoulder at 2475 eV is due to a transition to a C-S σ -type orbital. A comparison of the spectra of a thiol-ligand (APMT), a Ag-thiol complex (AGPMT), and the sodium salt of a thiol group (APMTNA) is shown in Figure 6.15. In contrast to the dramatic change seen in the S K-edge spectra as a result of a covalent interaction between Ag or Au and S, an ionic interaction between S and a metal results in the loss of the pre-edge peak, but no change in the shape or intensity of the white-line feature. This suggests that the ionic interaction between Na and S has little or no effect on the σ -symmetry final state orbitals, whereas the covalent interaction between Ag and S has a significant effect. As noted before, the loss in the pre-edge feature from thione to thiol to thiolate seems to be correlated to the accumulation of negative charge on the S atom, perhaps as a result of destabilization of the $p\pi^*$ orbitals.

6.3.4. Surface Measurements

Data were collected on two dyed and three chemically sensitized AgBr sheet crystal samples at glancing angle incidence. The dyed samples were treated with a cyanine dye (DC6) or a merocyanine dye (DM4), both of which contain Cl, thereby allowing Cl K-edge polarized measurements to be undertaken as well. Polarized measurements were collected on the merocyanine-dyed sample, corresponding to in-plane ($\chi = 0^\circ$) and out-of-plane ($\chi = 90^\circ$) orientations. For the cyanine-dyed sample, the signal-to-noise level was very poor in the out-of-plane orientation, so only in-plane measurements were made. The chemically sensitized samples consisted of a thiosulfate-treated AgBr sheet crystal, and two Au/S treated sheet crystal samples with differing Au:S ratios (Au:S 1:2 and 1:4). Data for these samples were collected in the in-plane orientation.

The in-plane polarized DC6 sample is compared to its powder spectrum in Figure 6.16. Although the noise level of the surface sample is very high, the intensity of the main

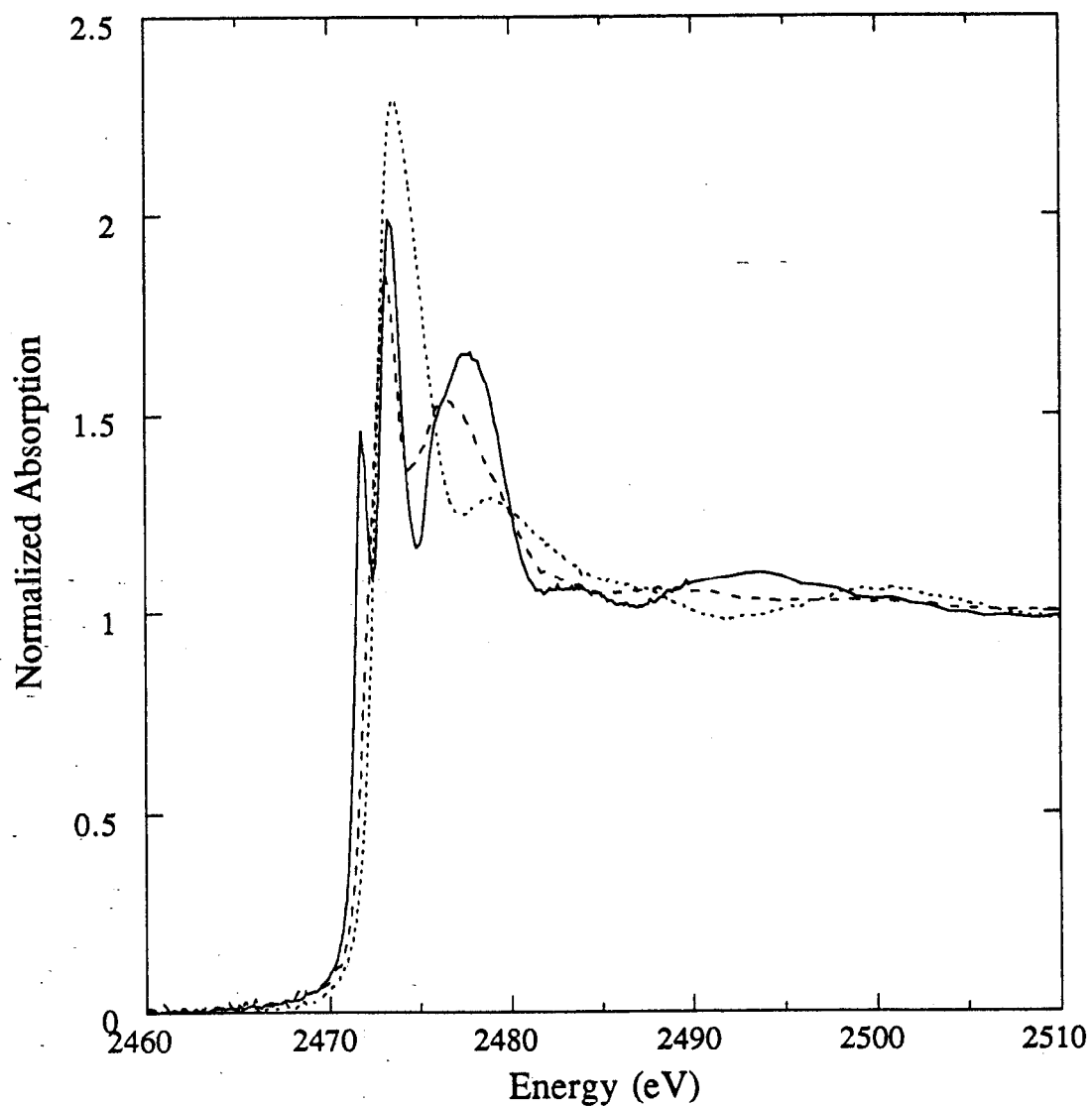


Figure 6.15. The S K-edge spectra of an exocyclic S-containing molecule (APMT, solid) compared with the spectra of an ionic (APMTNA, dash) and covalent complex (AGPMT, dot) with a similar molecule.

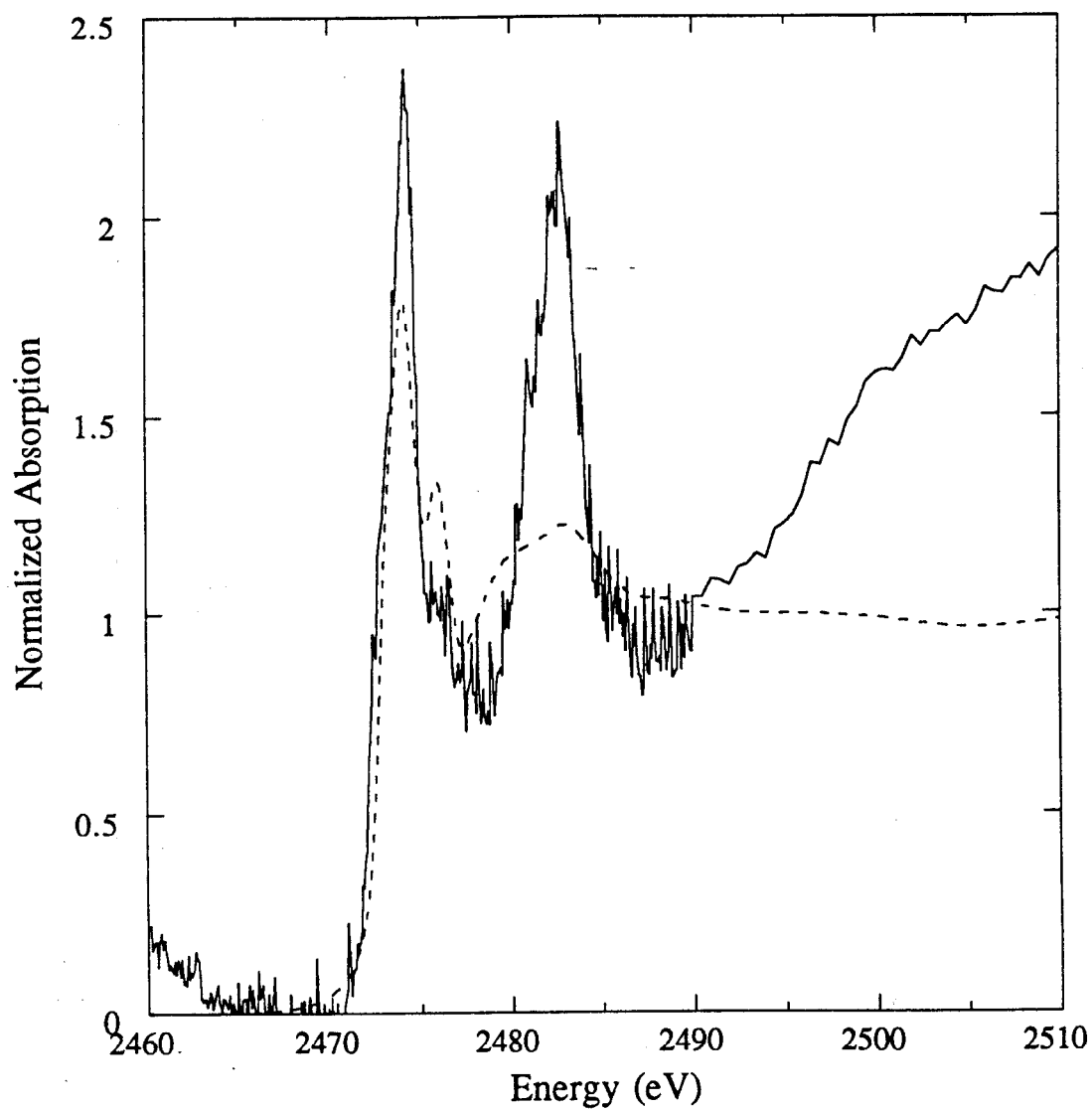


Figure 6.16. S K-edge surface spectrum of a AgBr sheet crystal treated with cyanine dye DC6 measured at $\chi = 0^\circ$ (solid), compared to the powder spectrum of DC6 (dash).

transition increases relative to the intensity of the same transition in the powder spectrum. The change in the surface DC6 spectrum is different from the change seen due to the interaction between Ag and benzthiazole sulfur (see Figure 6.12a), in which the intensity of the ligand feature decreases and the feature broadens. This suggests that the interaction between the cyanine dye S and the AgBr sheet crystal does not involve the same kind of interaction which occurs in silver benzthiazole. The same is observed for the merocyanine dyed surface sample. In both the in- and out-of-plane orientations (Figure 6.17), the thione pre-edge feature is present, and the white-line feature does not increase in intensity, therefore no bond between the thione S and the Ag in the AgBr sheet crystal is formed (see AGCMMT, Figure 6.13b; AUTMTU, AUETU2, and AUTHIOUR, Figure 6.13a-c). The features in the DM4 sample show an orientational dependence. The thione feature is more pronounced in the in-plane polarization than in the out-of-plane orientation. For polarization studies, intensity enhancement occurs when the polarization vector of the incident radiation is codirectional with the orbital of interest. The pre-edge feature is due to a transition to a S $p\pi^*$ orbital oriented out of the plane of the molecule. For the intensity of this feature to increase, the molecule is oriented on the surface so that this orbital is perpendicular to the direction of the beam and parallel to the polarization vector (Figure 6.1). This can only happen if the dye molecules are oriented edge-on, with the plane of the ring perpendicular to the surface and in the plane defined by the direction of the beam. If the orbital of interest is 100% parallel to the polarization vector in the in-plane orientation, one would expect the intensity of this feature to vanish in the out-of-plane orientation. The pre-edge feature does not vanish in the out-of-plane orientation, but it is about half as intense as in the in-plane spectrum. This suggests that the dye molecules may be tilted with respect to the plane of the surface with the result that the overlap of the $p\pi^*$ orbital with the polarization vector is not 0° in the out-of-plane configuration, resulting in some amount of excitation into this orbital.

The Cl K-edge data for the DC6 dyed sample is presented in Figure 6.18. For this sample, the white-line is very intense in the in-plane orientation and much less intense in the out-of-plane configuration. This suggests that the dye molecules are oriented so as to maximize the overlap of the C-Cl bond with the polarization vector for the in-plane orientation suggesting that the molecule is oriented with a ring axis perpendicular to the direction of the beam and parallel to the sheet crystal surface. It cannot be determined from these data if the dye molecules are oriented edge-on (with the plane of the ring perpendicular to the surface) or flat-on (with the plane of the ring parallel to the surface) as these orientations are identical with respect to the C-Cl bond. The polarized Cl K-edge spectra of the DM4 samples do not exhibit much polarization dependence (Figure 6.19),

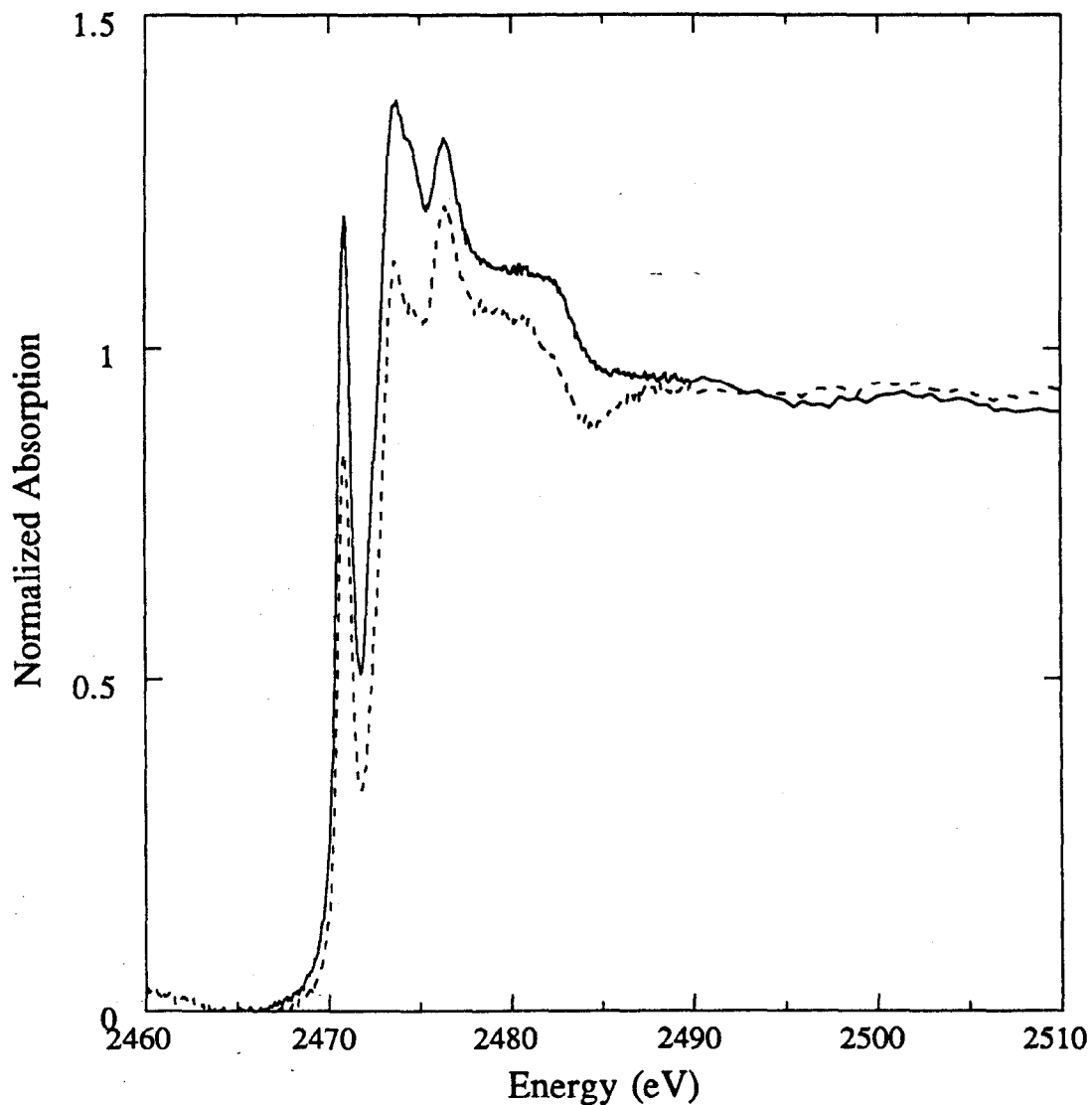


Figure 6.17. S K-edge surface spectra of a AgBr sheet crystal treated with merocyanine dye DM4, measured at $\chi = 0^\circ$ (solid) and $\chi = 90^\circ$ (dash).

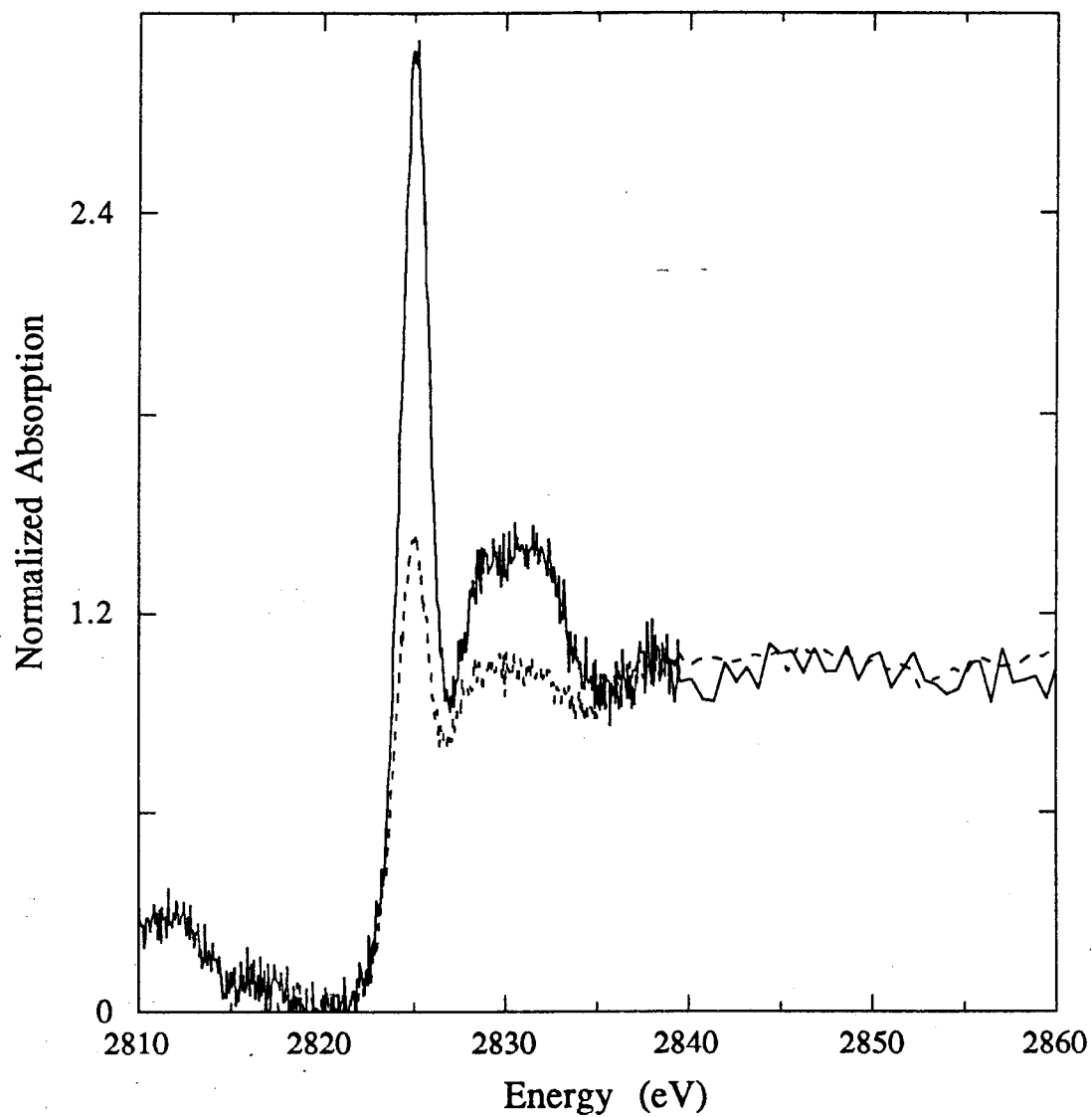


Figure 6.18. Cl K-edge surface spectra of a AgBr sheet crystal treated with cyanine dye DC6, measured at $\chi = 0^\circ$ (solid) and $\chi = 90^\circ$ (dash).

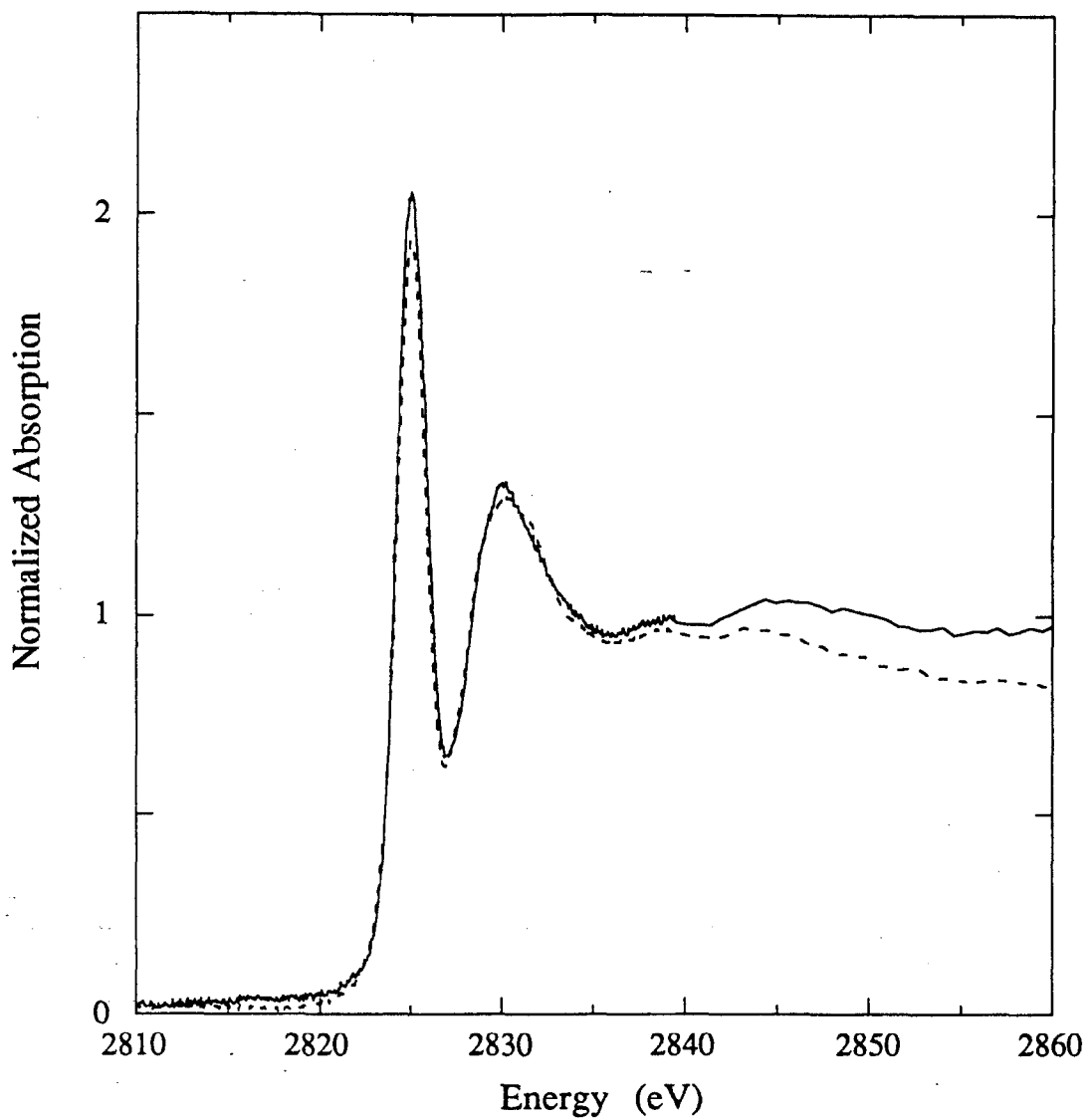


Figure 6.19. Cl K-edge surface spectra of a AgBr sheet crystal treated with merocyanine dye DM4, measured at $\chi = 0^\circ$ (solid) and $\chi = 90^\circ$ (dash).

suggesting that there may be some disorder in the alignment of the dye molecules on the AgBr substrate.

The thiosulfate-treated AgBr sheet crystal sample has an edge very similar to that of Ag₂S powder, and also similar to H₂S-treated Ag on quartz, suggesting that silver sulfide is the species formed during the sensitization process (Figure 6.20a, see Figure 6.13). The presence of Au in the 4:1 (Figure 20b) and 2:1 (Figure 20c) S: Au samples modifies the appearance of the edge features, with an increase in the intensity of the lower energy feature of the split main transition as the amount of gold increases. The edge spectra of the Au-treated samples are also different in appearance from the edge spectra of pure Au₂S₃ or Au₂S (Figure 6.13b), suggesting that the species formed during the sensitization treatment of the AgBr sheet crystals is distinct from Ag₂S and Au₂S₃ or Au₂S.

6.4. Discussion

These studies have shown that S and Cl K-edge X-ray absorption spectroscopy can be used to characterize the electronic and geometric structure of these low-Z atoms in components of the photographic system. The Cl K-edge spectra are essentially identical and do not depend on the type of molecule or on the position of Cl on the molecule. There are, however, striking differences in the spectra of molecules containing sulfur in an exocyclic (thione(ol)) position compared to a cyclic sulfur (thiazole). The white-line feature occurs at about the same position for all of the compounds studied, but is more intense for the thiazole compounds than for those containing thione(ol). This feature is polarized along the C-S bond and corresponds primarily to a transition to C-S $p\sigma^*$ orbital. X α calculations on thiophene, however, suggest that a transition to a $p\pi^*$ also contributes.^{6a} This was also seen from our single-crystal polarized studies in which a transition in the region of the white-line feature was seen in the out-of-plane orientation. For the exocyclic S compounds, only a transition to the C-S $p\sigma^*$ orbital contributes to the white-line feature. This difference could account for the increase of the white-line feature intensity of the thiazoles relative to the thione(ol)s.

A pre-edge feature below the position of the white-line is seen for compounds in which S is present as a thione or a thiol; this feature is absent in the cyclic sulfur compounds. The presence of this feature is due to a transition to a final state p orbital arising from the involvement of the exocyclic sulfur in a $p\pi$ system. This has been confirmed by our single-crystal polarized measurements, in which this feature was shown to be polarized perpendicular to the C=S bond and the plane of the ring, and by X α calculations by others.^{6b-c,7} For molecules containing exocyclic sulfur, the position of the

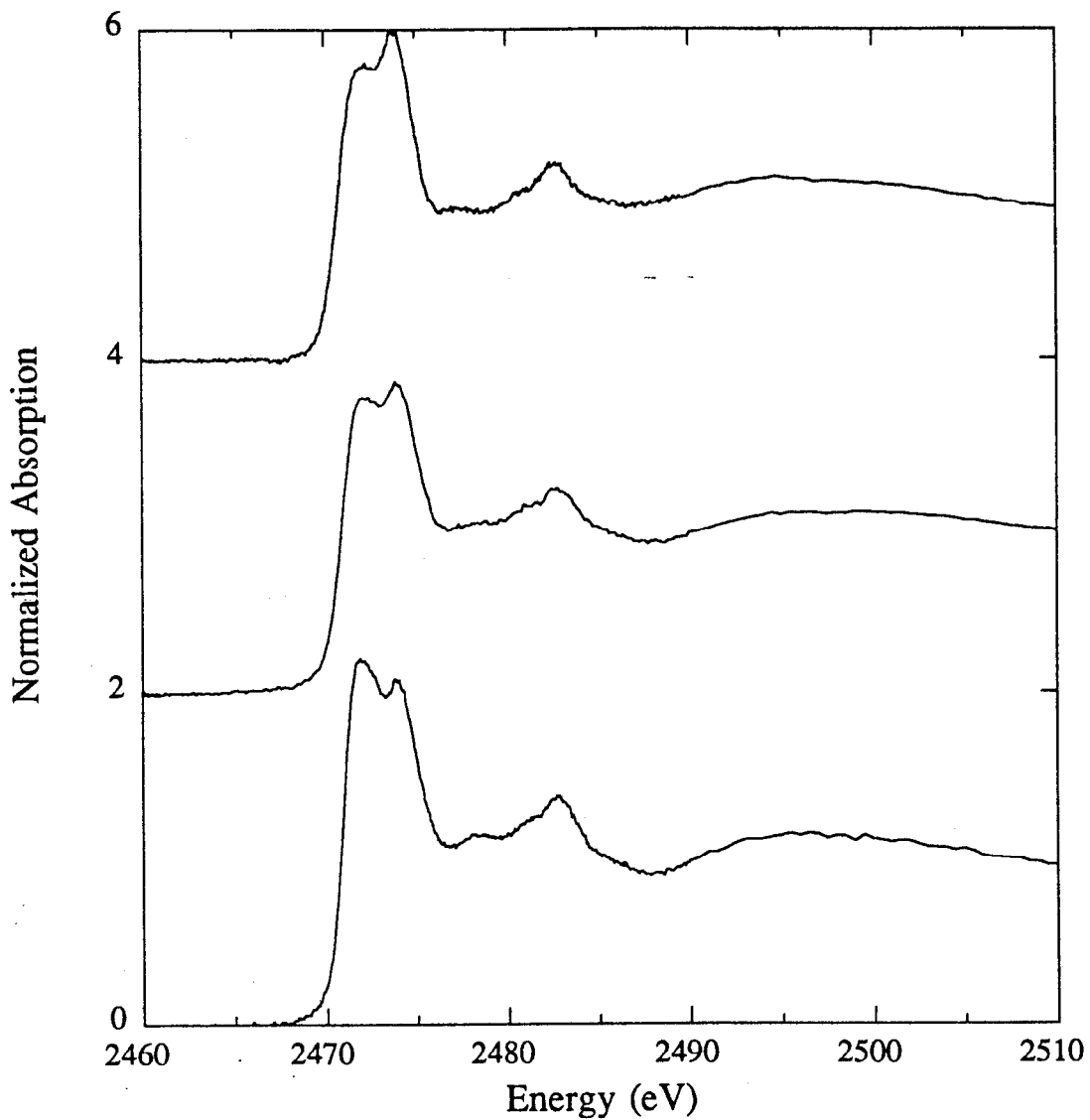


Figure 6.20. Surface spectra of (a) thiosulfate treated AgBr sheet crystal measured at $\chi = 0^\circ$, and gold dithiosulfate treated AgBr sheet crystals in a S: Au ratio of (b) 4:1 and (c) 2:1, measured at $\chi = 0^\circ$.

pre-edge feature moves to higher energy from thione to thiol to thiolate (Figure 6.8) and the position of the white-line feature moves to lower energy in accordance with the accumulation of negative charge on the sulfur atom. The movement of the thione feature to higher energy suggests that the change in the S environment from thione to thiol to thiolate must effect the final state C-S $p\pi^*$ orbital as well. The involvement of this orbital either in a covalent bond with H (thiol) or an ionic bond with Na^+ (thiolate) results in the partial or total filling of the otherwise empty $p\pi^*$ orbital, resulting in a destabilization of this orbital relative to the core level, hence the transition to this orbital appears at a higher energy.

There is also some variation seen in the intensity and position of the pre-edge feature within the thiourea molecules, in which the sulfur is present only as a thione, and within the tetrazoles, in which the S is present as a thiol. The differences in the intensity of the pre-edge feature from sample to sample probably reflect the amount of S $p\pi_z$ mixing in the final state orbital, whereas the differences in the position of the feature might reflect the accumulation of electron density on the S atom as a result of structural differences within the two classes of compounds. For example, EMT has an ethyl group in the 2 position, PMT has a phenyl group at the same location, and APMT has an acetamido-substituted phenyl group in the same position. In Figure 6.21, the S K-edge spectra of these compounds is compared. EMT has almost no pre-edge feature, whereas APMT has a well-resolved pre-edge feature, and PMT lies somewhere in between these two. It has previously been demonstrated that in going from a thione to a thiol to a thiolate (Figure 6.8) the pre-edge peak moves to higher energy and the white-line transition moves to lower energy as the electron density on the S atom increases. One possible explanation is that destabilization of the $p\pi^*$ orbital relative to the core level occurs due to the partial filling of that orbital by the interaction with H or Na, with the result that the transition occurs at higher energy. If the accumulation of electron density results in a shift to higher energy of the thione(ol) pre-edge feature, one would expect that EMT, which has an electron-donating group in the 2 position, would have the least resolved pre-edge feature, whereas APMT, which has a better electron-withdrawing group than PMT, would have the best resolved pre-edge feature. At the same time, the white-line transition of EMT should occur at a lower energy than that of APMT. These trends are seen in the data (Table 6.2).

The nature and extent of the interaction between S in photographic materials and Ag and Au metals, in conjunction with single-crystal polarized measurements, have been characterized. Covalent or ionic interactions with a metal (Ag, Au or Na^+) results in a dramatic change in the S K-edge (Figures 6.12, 6.13 and 6.15). The white-line feature for all exocyclic S-containing ligands increases in intensity due to a C-S $p\sigma^*$ interaction between S and the metal, and the pre-edge feature vanishes due to an interaction between

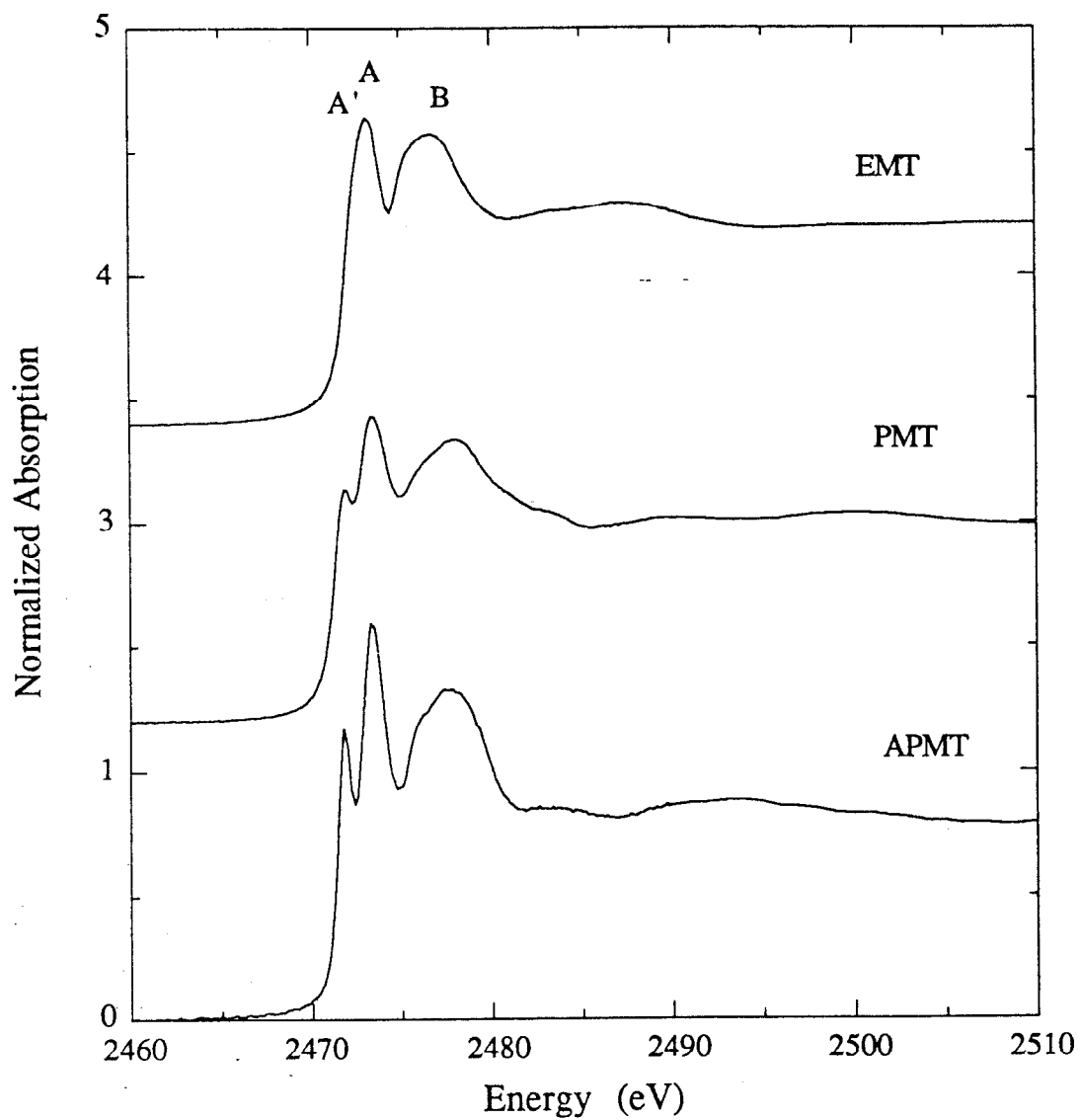


Figure 6.21. The powder spectra of EMT (top), PMT (middle) and APMT (bottom).

the S $\pi\pi^*$ orbital and the metal. The white-line feature has been shown by single-crystal polarized studies to have contribution from transitions to two σ orbitals, one with metal-sulfur character and one with carbon-sulfur character. This could explain the increase in the intensity of this feature upon complexation with a metal. There is also a feature in this same energy region for the out-of-plane oriented spectrum (Figure 6.14), which could be due to a transition to a Au-S $\pi\pi$ -type orbital occurring at the same energy as the σ transitions, or it could be that the involvement of the S $\pi\pi^*$ orbital with the metal results in a shift of the C-S $\pi\pi^*$ orbital of the non-complexed thione(ol) group (Figure 6.5) to this energy. Both of these possibilities would also contribute to the intensity of the white-line feature. For the silver benzthiazole compound, in which the silver metal interacts with a cyclic S compound, the white-line feature broadens and decreases in intensity. It is clear from these studies that the covalent interaction between Ag and Au with S in photographic materials results in a significant degree of change in the electronic structure of the S atoms and that studies of this type can be used to characterize the extent of the interaction between these metals and sulfur-containing components of the photographic system.

The dyed AgBr sheet crystal samples did not show the dramatic change in the S K-edge features associated with a bonding interaction between the metal and the sulfur (Figure 6.16 and Figure 6.17). This suggests either that the nature of the interaction in the systems studied is of a physical, rather than a chemical nature, or that any direct bonding interaction which does occur between the dye molecules and the AgBr substrate does not involve the S atoms. Although we believe that there was only a monolayer of dye on the surface, we cannot eliminate the possibility that we were sampling a multilayer region of the substrate and not the substrate/adsorbate interface. Unlike the study done by Stöhr et. al,²² we found that at angles greater than the glancing angle, there was a tremendous increase in the background which swamped the signal of interest. For these types of systems, a glancing angle configuration is required.

In the in-plane polarized spectrum of the merocyanine-dyed AgBr sheet crystal (thione S), the pre-edge feature is enhanced relative to the powder and the out-of-plane spectra. The enhancement of this feature in the in-plane polarized spectrum means that the dye molecules are oriented such that this orbital is parallel to the polarization vector; this in turn means that the plane of the ring of the molecule is in the plane defined by the direction of the beam and that the molecules stack together with the rings parallel. The presence of this feature in the out-of-plane polarized spectrum suggests that the alignment of the $\pi\pi^*$ orbital is not perfectly parallel to the surface; if the molecule were tilted with respect to the surface, there would be some amount of overlap with the polarization vector in the out-of-plane orientation resulting in some possibility of a transition occurring. The best insight

into the orientation of the DC6 molecules (thiazole S) is obtained from the polarization properties of the Cl K-edge, as we were unable to obtain a scan of the S K-edge in the $\chi = 90^\circ$ orientation. The white-line feature for the Cl edge of DC6 was most intense in the in-plane spectrum, and decreased in the out-of-plane spectrum (Figure 6.18), suggesting that the C-Cl bond is parallel to the polarization vector in the in-plane orientation. However, we cannot determine if the molecule is oriented edge-on or flat-on based on the results of the Cl K-edge studies. The treatment of the AgBr sheet crystals with gold dithiosulfate results in a sulfide species distinct from pure Ag_2S , Au_2S or Au_3S_2 , although the exact nature of the metal sulfide cluster formed cannot be determined from the data available.

6.5. Conclusions

X-ray absorption spectroscopy is particularly sensitive to the different environment of S in the merocyanine and cyanine dyes and dye intermediates, and single-crystal polarized studies have allowed determination of the origin of the transitions seen in the spectra to be made. XAS can distinguish between covalent and ionic interactions between a metal and exocyclic sulfur. A distinctive change occurs in the S K-edge spectra of Ag and Au metal complexes, allowing predictions of the nature of the dye adsorbate/AgBr substrate interaction to be made, and clearly showing that there is no covalent interaction between the Ag in the AgBr sheet crystals and the S in the cyanine and merocyanine dye molecules. In addition, the sensitivity of XAS to the polarization properties of the S K-edge features provides insight into the orientation of the dye molecules on the AgBr substrate. X-ray absorption spectroscopy has proven to be a valuable technique for characterizing and understanding the nature of S and Cl present in elements of the photographic system, as well as the nature of the interaction between S and Ag and Au metals.

6.6. Acknowledgements

This work was supported by research funds from Eastman Kodak Company. These data were collected at the Stanford Synchrotron Radiation Laboratory (SSRL) and at the National Synchrotron Light Source (NSLS), Brookhaven National Laboratory, which are supported by the Department of Energy, Division of Materials Sciences and Division of Chemical Sciences. SSRL is also supported by the National Institutes of Health, Biomedical Resource Technology Program, Division of Research Resources and by the Department of Energy, Office of Health and Environmental Research.

6.7. References and Notes

1. Hedman, B.; Frank, P.; Penner-Hahn, J. E.; Roe, A. L.; Hodgson, K. O.; Carlson, R. M. K.; Brown, G.; Cerino, J.; Hettel, R.; Troxel, T.; Winick, H.; Yang, J. *Nucl. Instr. and Meth.* **1986**, *A246*, 797.
2. Lytle, F. W.; Greigor, R. B.; Sandstrom, D. R.; Marques, E. C.; Wong, J.; Spiro, C. L.; Huffman, G. P.; Huggins, F. E. *Nucl. Instr. and Meth.* **1984**, *226*, 542.
3. Sugiura, C. *J. Chem. Phys.* **1983**, *79*, 4811.
4. (a) Huffman, G. P.; Huggins, F. E.; Mitra, S.; Shah, N.; Pugmire, R. J.; Davis, B.; Lytle, F. W.; Greigor, R. B. *Energy & Fuels* **3**, 1989, 200-205. (b) Spiro, C. L.; Wong, J.; Lytle, F. W.; Greigor, R. B.; Maylotte, D. H.; Lamson, S. H. *Science* **226**, 1984, 48-50. (c) George, G. N.; Gorbaty, M. L. *J. Am. Chem. Soc.* **111**, 1989, 3182-3186.
5. Tyson, T. A.; Roe, A. L.; Hodgson, K. O.; Hedman, B. *Phys. Rev. B* **1989**, *39*, 6305.
6. (a) Hitchcock, A. P.; Horsley, J. A.; Stöhr, J. *J. Chem. Phys.* **85**, 1986, 4835-4848. (b) Dezarnaud, C.; Tronc, M.; Hitchcock, A. P. *Chem. Phys.* **142**, 1990, 455-462. (c) Perera, R. C. C.; LaVilla, R. E. *J. Chem. Phys.* **81**, 1984, 3375-3382. (d) Hitchcock, A. P.; Bodeur, S.; Tronc, M. *Chem. Phys.* **115**, 1987, 93-101. (e) Hitchcock, A. P.; Tronc, M. *Chem. Phys.* **121**, 1988, 265-277. (f) Sze, K. H.; Brion, C. E.; Tronc, M.; Bodeur, S.; Hitchcock, A. P. *Chem. Phys.* **121**, 1988, 279-297.
7. (a) Yakata, Y.; Yoloyama, T.; Yagi, S.; Happo, N.; Sato, H.; Seki, K.; Ohta, T.; Kitajima, Y.; Kuroda, H. *Surf. Sci.* **259**, 1991, 266-274. (b) Seymour, D. L.; Bao, S.; McConville, C. F.; Crapper, M. D.; Woodruff, D. P.; Jones, R. G. *Surf. Sci.* **189/190**, 1987, 529-534. (c) Stöhr, J.; Kollin, E. B.; Fischer, D. A.; Hastings, J. B.; Zaera, F.; Sette, F. *Phys. Rev. Lett.* **1985**, *55*, 1468-1471.
8. Stöhr, J.; Outka, D. A. *Phys. Rev. B* **1987**, *36*, 7891-7905.
9. Herz, A. H. *Adv. Coll. Inter. Sci.* **1977**, *8*, 237.
10. Bird, G. R.; Norland, K. S.; Rosenoff, A. E.; Michaud, H. B. *Phot. Sci. Engr.* **1968**, *12*, 196.
11. Ficken, G. E. *J. Phot. Sci.* **1973**, *21*, 11.
12. Saijo, H.; Kitamura, T.; Ohtani, H. *Surf. Sci.* **1986**, *177*, 431-443.
13. Weiss, G.; Ericson, R.; Herz, A. *J. Coll. Inter. Sci.* **1967**, *23*, 277.
14. Spencer, H. E.; Atwell, R. E.; Levy, M. *J. Phot. Sci.* **1983**, *31*, 158.

15. Walker, L. A.; Folting, K.; Merritt, L. L. Jr. *Acta Cryst.* **1969**, *B25*, 88-93.
16. Nakatsu, K.; Yoshioka, H.; Aoki, T. *Chem. Lett.* **1972**, 339-340.
17. Trotter, J. *Acta Cryst.* **1986**, *C42*, 862-864.
18. Jones, P. G.; Guy, J. J.; Sheldrick, G. M. *Acta Cryst.* **1976**, *B32*, 3321-3322.
19. Stern, E. A.; Heald, S. M. *Rev. Sci. Instr.* **1979**, *50*, 1579.
20. Heald, S. M.; Keller, E.; Stern, E. A. *Phys. Lett.* **1984**, *103a*, 155-158.
21. Agarwal, B. K. in *X-ray Spectroscopy*, Springer Series in Optical Sciences vol. 15; D. L. MacAdam, Ed.; Springer-Verlag, Berlin, Heidelberg; 1979; pp 130 - 137
22. Stöhr, J.; Kollin, E. B.; Fischer, D. A.; Hastings, J. B.; Zaera, F.; Sette, F. *Phys. Rev. Lett.* **1985**, *55*, 1468-1471.